Investigation of turbulent shear flows with high resolution PIV methods

Sven Scharnowski

Vollständiger Abdruck der von der Fakultät für Luft- und Raumfahrttechnik der Universität der Bundeswehr München zur Erlangung des akademischen Grades eines

Doktors der Naturwissenschaften
(Dr. rer. nat.)

genehmigte Dissertation.

Gutachter:

1. Universitätsprofessor Dr. rer. nat. habil. Christian J. Kähler
2. Professor Dr. Fulvio Scarano
3. Dr. rer. nat. habil. Christoph Garbe

Die Dissertation wurde am 14.02.2013 bei der Universität der Bundeswehr München eingereicht und durch die Fakultät für Luft-und Raumfahrttechnik am 13.03.2013 angenommen. Die mündliche Prüfung fand am 08.10.2013 statt.

Danksagung

Die vorliegende Arbeit wurde am Institut für Strömungsmechanik und Aerodynamik der Fakultät für Luft- und Raumfahrttechnik an der Universität der Bundeswehr München angefertigt. Ich möchte mich hiermit bei allen bedanken, die zum Gelingen dieser Arbeit beigetragen haben. Ganz besonders danke ich Christian Kähler für die Möglichkeit, vielfältige und spannende Forschungsthemen in einer inspirierenden Atmosphäre bearbeiten zu dürfen. Sein Interesse an meiner Arbeit, seine Erfahrung, seine ständige Bereitschaft zu wissenschaftlichen Diskussionen und ganz besonders seine kritischen Anmerkungen haben wesentlich zum Gelingen dieser Arbeit beigetragen.

Fulvio Scarano und Christoph Garbe erklärten sich bereit, die Rolle der weiteren Gutachter zu übernehmen. Ich danke ihnen dafür, dass sie sich die Zeit genommen haben, die Dissertation durchzuarbeiten und zu bewerten, sowie für den Vortrag und die Prüfung nach Neubiberg zu reisen.

Unter meinen Kollegen möchte ich Rainer Hain und Christian Cierpka hervorheben. Sie haben mir den Einstieg in die Strömungsmechanik und die Strömungsmesstechnik erleichtert, indem sie ihr Wissen gerne an mich weitergaben. Darüber hinaus waren sie stets bereit, neue Ideen mit mir zu diskutieren und kritisch zu hinterfragen.

Meiner Frau Anja und meinen Kindern Fabian und Louisa danke ich von ganzem Herzen für ihr Verständnis, ihre Unterstützung, aber ganz besonders dafür, dass sie mir täglich zeigen, dass es noch mehr als nur Physik gibt.

Neubiberg, den 25.03.2014

Sven Scharnowski

Kurzfassung

Die abgelöste Strömung im Nachlauf eines generischen Trägerraketenmodells wurde experimentell bei einer sehr hohen Reynolds-Zahl und einer transsonischen Machzahl untersucht, um die physikalischen Phänomene, die zum Buffeting führen, aufzuklären und verlässliche Validierungsdaten für numerische Strömungssimulationen zu generieren. Aufgrund der großen Dynamik der verschiedenen Skalen und der Geschwindigkeit in turbulenten Scherschichtströmungen war im Rahmen der Arbeit eine Weiterentwicklung der etablierten PIV-Messtechnik erforderlich. Eine grundlegende Untersuchung der räumlichen Auflösungsgrenze identifizierte eine ideale Messanordnung und die beste Auswertetechnik, um die gewünschten Ergebnisse über die Nachlaufströmung des untersuchten Trägerraketenmodells zu erhalten. Außerdem wurde ein neues Verfahren entwickelt, um die Wahrscheinlichkeitsdichtefunktion der Geschwindigkeit direkt aus der PIV-Korrelationsfunktion abzuschätzen. Dieser Ansatz ermöglicht die direkte Bestimmung der Reynolds- Normal- und Schubspannung ohne nennenswerte räumliche Tiefpassfilterung gegenüber etablierten Auswertemethoden und führt zu einer wesentlich verbesserten Auflösung und Genauigkeit. Weiterhin wurden einzelne Wirbel in der abgelösten Scherschicht in momentanen Geschwindigkeitsfeldern detektiert, um die Entstehung und Bewegung turbulenter Strukturen zu analysieren. Eine statistische Analyse der detektierten Wirbel zeigt deren räumliche Verteilung in Abhängigkeit von der Wirbelgröße und -stärke. Die kombinierte Anwendung der entwickelten Auswerteverfahren liefert einen breiten Überblick über die Strömungsvorgänge im Nachlauf des Trägerraketenmodells und liefert eine Datenbasis, die für die Validierung neuer numerischer Werkzeuge eingesetzt werden kann. Darüber hinaus sind die verbesserte Abschätzung der Reynoldsspannungen und die theoretischen Überlegungen zur räumliche Auflösung von grundlegender Bedeutung für viele andere Experimente.

Abstract

The separated wake flow of a generic space launcher model was investigated experimentally at a very high Reynolds number and a transonic Mach number in order to analyze the physical phenomena that lead to buffeting and to generate reliable validation data for computational fluid dynamics. Due to the large dynamic range of scales and velocities in turbulent shear flows, it was necessary to improve the state-of-the-art PIV techniques. A fundamental investigation of the spatial resolution limit identified the ideal measurement setup and the best evaluation approach to obtain the desired results of the wake flow for the investigated space launcher model. Additionally, a new method was developed to estimate the velocities' probability density function directly from the PIV correlation function. This approach allows for the direct determination of the Reynolds normal and shear stress without significant spatial low-pass filtering, compared to established methods, and results in significantly improved resolution and accuracy. Furthermore, individual vortices in the separated shear layer were detected in instantaneous velocity fields to

investigate the formation and motion of turbulent structures. A statistical analysis of the detected vortices reveals their spatial distribution with respect to their size and swirling strength. The combination of the developed evaluation techniques yields a broad overview of the flow phenomena in the space launcher model's wake and results in a data basis that may serve for the validation of new numerical tools. Beyond that, the improved estimation of Reynolds stresses and the theoretical considerations regarding the spatial resolution are of fundamental importance for many other experiments.

Contents

1 Introduction

1.1 The space launcher's wake

The transportation of satellites and other aero/astro-space technical equipment from earth's surface to a near earth orbit or even to outer space requires efficient delivery systems, that fulfill a number of demands, e.g. a high degree of reliability in extreme conditions, enough power to mobilize massive pieces of hardware and superior cost effectiveness. The European space launcher *ARIANE V* consist of the cryogenic main stage and two solid rocket boosters attached to the side of the main stage, as shown in Fig. 1.1. More than 10 tonnes of payload can be accommodated in the second stage, which is placed in the top part of the main stage and covered by the fairing. In its first 140 seconds, the launcher is accelerated to a velocity of approximately 2,000 m/s by the solid boosters. After separation, the main engine (Vulcan 2) lifts the main stage to an altitude of ca. 150 km, where the fairing splits off and the upper stage is released. In the case of flight VA208 (August 2, 2012), the conditions for geostationary transfer orbit (altitude: 658 km, velocity: 9,352 m/s) had been achieved less than 30 minutes after ignition and the payload (*Intelsat 20* and by *Hylas-2*) was released[1].

The wake flow of a space launcher is characterized by a large separation region during atmospheric ascent. Schrijer et al (2011) recently performed wind tunnel experiments on a 1 : 60 sub-scale model of the *ARIANE V.* They showed that the boundary layer separating at the rear end of the main body reattaches at the main engine's nozzle. This reattachment causes strong wall pressure fluctuations which lead to increased dynamic loads for the nozzle structure. The loads are strongest in the transonic regime and the characteristic frequencies of the pressure fluctuations may interfere with the structural modes of the nozzle leading to so called buffeting. A sketch of the wake flow is illustrated in Fig. 1.2.

In order to develop design rules for the geometry of a space launcher's rear end, it is necessary to investigate the effect of all relevant parameters on the wake flow. It is essential to understand the relation between flow parameters (boundary layer state, flow velocity, pressure, temperature) and geometry parameters (main stage diameter, nozzle location and size), on the one hand, and flight performance and mechanical loads, on the other hand. To achieve the required overview it is necessary to vary the parameters of question

[1] http://www.esa.int

(a)

(b)

(c)

Figure 1.1: (a) ARIANE V cryogenic main stage with the Vulcain 2 engine, (b) compleated launcher on its mobile launch table and (c) liftoff of the 57th ARIANE V (VA201) from Europe's Spaceport in French Guiana (images provided by ESA).

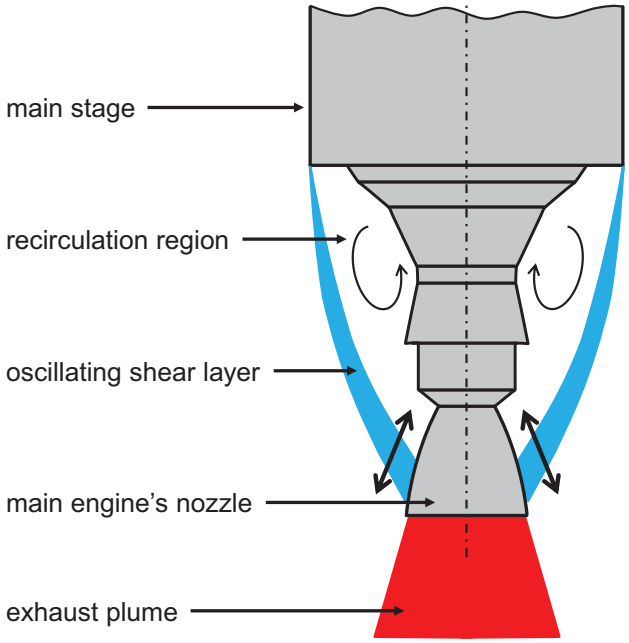

Figure 1.2: Sketch of the space launcher wake: The main body boundary layer separates and reattaches on the main engine's nozzle.

and analyze their effect with adequate tools. These tools can be computational fluid dynamics (CFD) and/or experimental flow investigations.

1.2 Previous investigations of backward-facing step flows

The flow over a backward-facing step, like at the rear end of a space launcher, is very important from a technological point of view as well as for fundamental fluid mechanic research. It was extensively studied both experimentally and numerically in the past. Although the geometry is rather simple, the flow field is relatively complex, as illustrated in Fig. 1.3. The incoming boundary layer separates at a sharp edge. A Kelvin-Helmholtz instability develops in the first part of the thin shear layer and generates coherent vortices. The vortices grow in size and strength while traveling downstream. This causes, on average, a broadening of the shear layer with increasing distance from the point of separation and an amplification of the turbulent fluctuations. The mean flow field is characterized by a large recirculation region, which is separated from the outer region by the dividing streamline. Some of the shear layer vortices are pulled into the recirculation region by an adverse pressure gradient and they interact with the next generation of shear layer vortices. Due to this feedback, the shear layer of a backward-facing step differs significantly from a free shear layer. Furthermore, the vortices traveling backwards within the primary recirculation region generate secondary ones. As a result, a secondary recirculation region

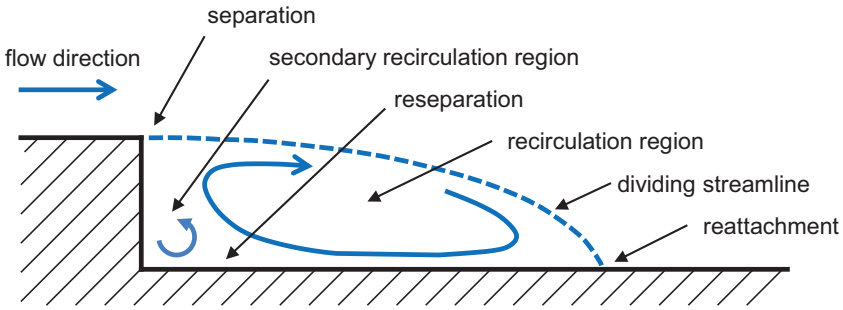

Figure 1.3: Backward-facing step flow field.

is formed in the corner of the primary recirculation region, which appears in the averaged flow field.

Bradshaw and Wong (1972) as well as Eaton and Johnston (1981) showed in their review papers, that for $2D$ backward-facing steps the stream-wise extension of the primary recirculation region mainly depends on the step height and on the incoming boundary layer state. The reattachment length is between 5 and 7 times the step height for fully turbulent incoming flow over a Reynolds number range of $\mathrm{Re_h} = 3 \times 10^3 \ldots 3 \times 10^5$ (based on the step height).

Eaton and Johnston (1981) found that the first part of the separated shear layer is similar to a plane-mixing layer, since the dividing streamline is only slightly curved and the shear layer is thin enough to be unaffected by the wall. The second half of the separated flow region is characterized by a strongly curved shear layer, indicated by the dividing streamline in Fig. 1.3. In this region the shear layer broadens and the Reynolds stresses increase. Eaton and Johnston (1981) compared several $2D$ experiments and concluded that the stream-wise location with maximum stream-wise Reynolds stress and Reynolds shear stress is close to the reattachment location or slightly upstream. Whether or not the stresses in the shear layer are even higher could not be answered so far due to the limited spatial resolution of the measurement techniques applicable to these kind of flows.

A characteristic feature of the backward-facing step flow is the splitting of the reattaching shear layer. Bradshaw and Wong (1972) predicted that at reattachment large eddies are torn in two and, as a result, the eddies are decreased in size further downstream, which could not be verified experimentally at that time. On the other hand, Chandrasuda (1975) and McGuinness (1978) concluded that some of the large eddies follow the upstream moving fluid, while the others are traveling further downstream. The early measurements presented in Bradshaw and Wong (1972) and in Eaton and Johnston (1981) were performed by point-like probes (LDA and hot-wire). Thus, they reveal only temporal profiles rather than spatial distributions and are not able to detect instantaneous flow structures. More recently, Huang and Fiedler (1997) used PIV to study the temporal development of the starting flow of a backward-facing step in a water tunnel at $\mathrm{Re_h} = 4300$. They showed

that an initially formed regular vorticity street collapses after a short time due to vorticity interaction.

Later on, Scarano et al (1999) and Schram et al (2004) used PIV to investigate turbulent structures within instantaneous velocity fields and demonstrated the suitability of PIV for the detection of vortices and the measurement of their size and swirling strength at relatively low Reynolds numbers ($\mathrm{Re_h} \approx 5000$). It was shown that the size of span-wise aligned rollers grows nearly linearly in the first part of the shear layer. Furthermore, a significant fraction of counter rotating vortices indicated an early three dimensional breakdown resulting in a varying reattachment location. Le et al (1997) also observed this phenomena in direct numerical simulations (DNS) for a similar test case.

Roshko and Thomke (1966) observed the turbulent reattachment downstream of an axisymmetric step in supersonic flow by means of pitot probe measurements and schlieren images. They found that the reattachment length is only 2.8 to 3.7 times the step height for Mach numbers between 2 and 4.5. Experiments in the subsonic regime also showed a decreased length of the reattachment region (Hudy et al, 2003, 2005) indicating that the round shape of the model reduces this quantity.

In the last years, the wake of space transportation systems was in the focus of several close collaborations to perform numerical investigations and experiments. The FESTIP (Future European Space Transportation Investigations Program) and the RE–SPACE project (Key Technologies for Reusable Space Systems), for example, developed new technologies and new simulation methods for reusable launchers (Pfeffer, 1996; Gülhan, 2008). The ESA TRP –Unsteady Subscale Force Measurements within a Launch Vehicle Base Buffeting Environment– concentrated on the *ARIANE V* base flow and investigated the wake of a space launcher model by means of PIV and tested potential buffeting reduction devices (Hannemann et al, 2011; Schrijer et al, 2011). Furthermore, several numerical (Lüdeke et al, 2006; Deck et al, 2007) and experimental (David and Radulovic, 2005; Deprés et al, 2005) works have analyzed the flow around a 1/60 model of the *ARIANE V* space launcher including solid state boosters and other smaller components. David and Radulovic (2005) and Deprés et al (2005) performed unsteady wall pressure measurements on the after-body of the space launcher model at the DNW High Speed Wind Tunnel. Both reported wall pressure fluctuations corresponding to a Strouhal number of $St_\mathrm{d} = f \cdot d/u_\infty \approx 0.2$, which occur only for azimuthal angles between the solid state boosters. David and Radulovic (2005) also presented unsteady wall-pressure measurements during atmospheric flight of the real *ARIANE V* launcher during flight 521, which confirm the wind tunnel observations.

The flow over a cylindrical forebody elongated by a second cylinder of smaller diameter and finite length is a generic version of a space launcher's rear end. It was in the focus of several numerical investigations (Deck et al, 2007; Weiss et al, 2009; Meiss and Schröder, 2008; Statnikov et al, 2012) and of experiments presented in Deprés et al (2004). The smaller cylinder, which has a length of 1.2 times the diameter of the forebody, represents the main engine's nozzle. Deprés et al (2004) performed unsteady wall pressure measurements on the elongated cylinder at Mach numbers between 0.6 and 0.85. They found that for long

enough rear bodies the separated flow reattaches at the end of the nozzle dummy. Two characteristic frequencies were found in the pressure spectra. The corresponding Strouhal numbers are $St_d = 0.2$ and $St_d = 0.6$, which are related to formation of large scale vortices and convection of turbulent eddies in the separated shear layer, respectively. Recently, Bitter et al (2012) analyzed the pressure dynamics for a similar model, with a very long base cylinder, using fast-responding pressure-sensitive paint. They showed the spatial distribution of the surface pressure: The maximum spectral amplitude corresponds to a Strouhal number of $St_d = 0.21$ and was detected at a location shortly after reattachment.

1.3 Computational and experimental approaches

The motion of a fluid in space and time $\vec{u}(\vec{x},t)$ is characterized by the conservation of mass, energy and momentum. The main equations are summarized here by following the work of Kundu and Cohen (2008) as well as the online documentation at http://www.cfd-online.com. The conservation of mass $\mathrm{d}m/\mathrm{d}t = 0$ leads to the continuity equation, which has the following form in the case of compressible fluids:

$$\frac{\partial \rho}{\partial t} + \frac{\partial}{\partial x_i}(\rho u_i) = 0 \tag{1.1}$$

Where ρ is the fluid density and u_i are the velocity components. The conservation of momentum is derived from Newtons second law:

$$\frac{\partial}{\partial t}(\rho u_i) + \frac{\partial}{\partial x_j}(\rho u_i u_j + p\delta_{ij} - \tau_{ij}) = 0 \tag{1.2}$$

Where p is the pressure and τ_{ij} is the viscous stress tensor (for Newtonian fluids):

$$\tau_{ij} = 2\mu e_{ij} \tag{1.3}$$

with the viscosity μ and the strain rate tensor e_{ij} defined as:

$$e_{ij} = \frac{1}{2}\left(\frac{\partial u_i}{\partial x_j} + \frac{\partial u_j}{\partial x_i}\right) - \frac{1}{3}\frac{\partial u_k}{\partial x_k}\delta_{ij} \tag{1.4}$$

From the fist law of thermodynamics the equation for the conservation of energy is derived:

$$\frac{\partial}{\partial t}(\rho e) + \frac{\partial}{\partial x_j}(\rho u_j e + u_j p + q_j - u_i \tau_{ij}) = 0 \tag{1.5}$$

Where e is the internal energy per unit mass and the heat flux is given by

$$\vec{q} = -k\nabla T. \tag{1.6}$$

With the conductivity k and the temperature gradient ∇T.

Equations (1.1), (1.2), and (1.5) are referred to as the Navier-Stokes equations. To close the equations it is necessary to specify an equation of state, like $p = \rho RT$ for a perfect gas. The Navier-Stokes equations are a system of nonlinear partial differential equations, in general.

Although, it is not yet proved that solutions always exist (nor that they are smooth and have bounded kinetic energy), the Navier-Stokes equations are widely used in computational fluid mechanics (CFD) to predict the motion of non-relativistic fluids, which can be treated as continuum. However, direct numerical simulation (DNS) of a turbulent shear flow requires an enormous amount of computational power. The computational mesh must be fine enough to resolve all spatial scales ranging from the smallest dissipative one, the Kolmogorov scale η, up to the integral length scale L, associated with the largest turbulent structure. The Kolmogorov scale η is given by:

$$\eta = \left(\frac{\nu^3}{\varepsilon}\right)^{1/4} \tag{1.7}$$

Where ν is the kinematic viscosity and ε is the rate of kinetic energy dissipation (Kolmogorov, 1962). Typically, η is in the range of millimeters for oceans and the atmosphere and reaches the micrometer scale for laboratory experiments (Kundu and Cohen, 2008). Thus, several orders of magnitude must be covered by the computational mesh. Due to this, DNS is mainly used for fundamental research at relatively low Reynolds numbers, where it still requires the use of supercomputers (Moin and Mahesh, 1998; Ishihara et al, 2009; Wu and Moin, 2009).

If the computational mesh is not fine enough to resolve the Kolmogorov length scale, large eddy simulations (LES) are applied to solve the Navier-Stokes equations. LES was proposed by Smagorinsky (1963), it explicitly resolves the large turbulent structures, the large eddies, and implicitly resolves the small eddies by using a sub-grid model. This leads to spatially low-pass filtered velocity fields. Although the resolution is decreased, compared to DNS, LES has become a powerful tool for the simulation of turbulent flows in industrial environment or for fundamental research (Mason, 2006; Pitsch, 2006; Sagaut, 2005). Due to the reduced computational time it became possible to simulate flows around objects with complex geometries.

When the computational costs must be reduced even further, it is possible to compute only the mean velocity field from the Navier-Stokes equations. Here, the instantaneous quantities are substituted by time-averaged and fluctuating ones (Reynolds decomposition). The velocity for example is rewritten as follows:

$$u_\mathrm{i} = \langle u_\mathrm{i} \rangle + u_\mathrm{i}' \tag{1.8}$$

Where $\langle u_\mathrm{i} \rangle$ is the mean velocity and u_i' its corresponding fluctuation. The Reynolds decomposition of $\vec{u}$ and p allows for reducing Eqs. (1.1), (1.2), and (1.5) to the Reynolds-averaged

Navier-Stokes equations (RANS) for incompressible flow. In the case of compressible flow, also density and viscosity must be decomposed leading to the Favre-averaged Navier-Stokes equations (Favre, 1965; Canuto, 2009). A remaining issue of this procedure is that the Reynolds decomposition introduces additional terms to the system of equations. The so called Reynolds stress tensor $-\rho \left\langle u_i' u_j' \right\rangle$ represents the apparent stress of the fluctuating velocity field and was not part of the Navier-Stokes equations. To account for the additional unknowns, the RANS (or Favre-averaged Navier-Stokes) equations must be supplemented with turbulence models. A variety of different turbulence models was developed to close the equations (see for instance Spalart and Allmaras (1992); Menter et al (2003); Kalitzin et al (2005))

To analyze the wake of a space launcher during atmospheric ascent with CFD tools, direct numerical simulation of the Navier-Stokes equations is far to slow, even for today available supercomputers. Also LES requires very much computational effort. To achieve results after reasonable computational time, RANS and LES methods must be combined for the simulation of the transonic wake flow: The forebody (Statnikov et al, 2012; Roidl, 2012) or the outer region (Deck et al, 2007) is simulated with RANS at fairly low cost and only the wake is analyzed by means of LES. Such novel approaches need to be validated using experimental data.

To achieve experimental data of the flow velocity, different measurement techniques were developed in the past: The first quantitative measurements were done by probes that need to be placed within the flow. The pitot pressure probe measures the dynamic pressure in the flow from which the local velocity can be estimated (Pitot, 1732; Darcy, 1858). Hot-wire anemometers measure the velocity electrically: A thin metal wire is heated electrically and cooled by the flow. The temperature of the wire yields information about the (absolute value of the) flow velocity. The temperature, on the other hand, influences the resistance of the wire, which is measured electrically (King, 1914; Wattendorf and Kuethe, 1934; Corrsin, 1947; Wyngaard, 1968). The main drawbacks of these probes are (1) that they measure only point-wise data and (2) that they need to be placed within the flow, right at the position of interest.

More recently, optical sensors were used to determine the flow velocity. Laser-Doppler anemometers (LDA), also known as Laser Doppler Velocimeters (LDV), measure the velocity of small tracer particles seeded into the flow (Foreman et al, 1965). Two coherent laser beams (generated by slitting one beam) are crossed and form interference fringes. Particles that cross the fringe pattern scatter light that is collected by a photo-detector. The frequency of the scattered light intensity is directly proportional to the velocity component perpendicular to the fringe orientation. The big advantage over probes is that the fluid is undisturbed, apart from tracer particles. A remaining issue is that only one velocity component is measured for one point (average over a small volume) in space. Only complex setups, using a combination of three LDVs with different laser wavelengths, allow for the estimation of all three velocity components (Tian et al, 2007; Chesnakas and Dancey, 1990). In order to measure the spatial distribution of velocity fields with the

point-wise techniques discussed above, one would have to either traverse the sensor or to use several sensors at the same time. However, traversing the sensor would not allow for measuring instantaneous vector fields and using several sensors results in a rather complex setup.

To overcome this fundamental problem, Particle Image Velocimetry (PIV) was invented more than two decades ago. PIV estimates, analog to LDV, the flow velocity from the motion of tracer particles. The differences to the LDV technique are that (1) a much larger volume is illuminated and (2) the scattered light of thousands of tracer particles is captured at the same time. Using one double-shutter camera and a double-cavity laser allows for measuring two velocity components an a plane. Two cameras in a stereoscopic setup yield all three velocity components and three or more cameras enable to measure the velocity field in a volume rather than in a plane. Among all this measurement techniques, PIV is the only one that is capable to measure gradient based quantities, such as vorticity or dissipation rate from instantaneous vector fields. Furthermore, with the development of digital Particle Image Velocimetry in the last years it became possible to acquire and process huge amounts of data, which allows for estimating flow statistics or for investigating the temporal development of flow phenomena.

PIV seems to be the best available experimental method for the investigation of turbulent shear layers. However, the experimental investigation also has some limitations: One is that the measurements are usually done on a sub-scale model in wind tunnels, where the model must be mounted. This model mounting, as well as the wind tunnel walls, are a deviation from the geometry of interest. Another drawback of PIV experiments, compared to CFD, is that the information is collected on a regular grid, which cannot be refined in regions with strong gradients. Thus, an enormous dynamic spatial range is required to resolve the different scales of turbulent shear flows.

It can be concluded that a combination of PIV and CFD methods should be used to achieve the knowledge required for the design of future space launchers. Combined RANS-LES methods, on the one hand, are in principle capable to simulate a full-scale launcher at transonic Mach numbers during atmospheric ascent. On the other hand, experimental data must be used to validate the numerical methods in order to verify whether the simulated turbulence spectrum is sufficient or not (in the case of LES) and whether the turbulence modeling is realistic or not (in the case of RANS).

1.4 Structure of the thesis

This thesis was performed within a sub-project of the SFB-TRR 40 program “Technological foundations for the design of thermally and mechanically highly loaded components of future space transportation systems”, founded by the German research foundation (DFG). The scientific focus within the SFB-TRR 40 is the analysis and modeling of coupled liquid

rocket propulsion systems and their integration into the space transportation system[2]. Based on reference experiments, numerical models are developed, which serve as a basis for efficient and reliable predictive simulation design tools. A combined optimization of the major components under high thermal and mechanical loads, e.g. combustion chamber, nozzle, structure cooling, and after body, is undertaken within the SFB-TRR 40 program to achieve an enduring increase in the efficiency of the entire system. For the validation of the wake flow simulation with new numerical tools, a generic model was designed, which is investigated numerically and experimentally. Only a generic model with simple geometry is suited for such a combined investigation. It allows for the analysis of the basic physical phenomena without the effects of complex geometries. Nevertheless, once the numerical tools are validated, the geometry can be altered to design future space launchers.

The here considered sub-project concentrates on the experimental investigation of the turbulent wake flow of a generic space launcher model in a transonic regime. The overall objective is to achieve a deep understanding of the flow physics of the space launcher model's wake for two reasons: (1) to create a data basis that can serve as reference for the validation of new numerical methods and (2) to identify the sources of the characteristic pressure fluctuations in order to be able to reduce the buffeting to an acceptable level in future works. To fulfill the objective it was necessary to improve the existing measurement techniques as well as the evaluation methods.

The thesis consists of 5 chapters. This introduction is followed by a chapter discussing the basics of digital Particle Image Velocimetry. The equipment necessary for PIV is briefly introduced and an overview of the different evaluation techniques is shown. With the intention to validate numerical flow simulations, a detailed analysis of the theoretical limits of PIV is very important. Therefore, the resolution limit of PIV and the uncertainty for the estimation of near-wall velocity profiles is also discussed in Chapter 2.

In Chapter 3 the spatial resolution for flow statistics – such as the Reynolds stresses – is improved. The combination of the mean velocity field and the Reynolds stress distribution is well suited for a comprehensive characterization of a flow phenomena such as a space launcher's wake. In contrast to instantaneous velocity fields, it allows for a comparison of different experiments among themselves as well as of experiments with flow simulations. Furthermore, in CFD the Reynolds stress tensor is required for closing the RANS equations. Chapter 3, shows for the first time, how Reynolds normal and shear stresses, in a $2D$ regime, can be estimated from the velocity's probability density function, which is estimated from PIV correlation functions. This approach results in significantly improved spatial resolution and does not suffer from spatially low-pass filtering, as previous methods do.

Chapter 4 discusses the possibility to detect vortices from PIV velocity fields. Vortices are the source of dynamic loads, their location, size, swirling strength, and orientation is very important for the characterization of turbulent shear flows. Chapter 4 shows that the detectability of vortices depends on the resolution of the vector field. The large scale vortices, which contain most of the energy can be identified.

[2] http://www.sfbtr40.de

Finally, the wake of a generic space launcher model is analyzed at a Mach number of 0.7 in Chapter 5. This chapter contains the evaluation of state-of-the-art experiments analyzed with sophisticated PIV evaluation methods. The analyzed data set was acquired at relatively low optical magnification resulting in a large field of view, which yields the required overview. On the other hand, the mean velocity distribution as well as the Reynolds stress distribution are reliably estimated with very high resolution. Thus, it is possible to cover a large dynamic spatial range, which allows for the investigation of small (thin shear layer, corner vortex) and large scales (recirculation region) at the same time. Furthermore, the appearance of shear layer vortices in the wake of the space launcher model is analyzed. The spatial distribution of the vortices with respect to their size and swirling strength as well as the spatial distribution of the mean velocity field and the Reynolds normal and shear stresses yield fundamental information about the connection of these quantities.

2 Particle Image Velocimetry

Particle image velocimetry (PIV) is a non intrusive measurement technique that estimates the velocity field of a flow in a plane, or even in a volume, by measuring the displacement of appropriate particles in a certain time interval Δt. Therefore, tracer particles which follow the fluid motion faithfully are illuminated twice by a laser and the light scattered from the particles at the time t and $t + \Delta t$ is recorded on successive frames of a digital camera, as illustrated in Fig. 2.1. In a second step the recorded image pair is subdivided into several thousand interrogation windows and the average particle image displacement is estimated by spatial cross-correlation methods for each interrogation window. Finally, the local flow velocity for each interrogation window is estimated from the location of the signal peak in the correlation plane by taking into account the optical magnification of the imaging system and the time interval between the two illuminations (Adrian and Westerweel, 2010; Raffel et al, 2007).

This chapter describes the key elements of PIV measurements: Section 2.1 discusses the required components and their interaction. Imaging system, light source and tracer particles must match certain requirements, which are defined by the experiment. Section 2.2 explains the evaluation principle of PIV. Two well developed methods, window-correlation and single-pixel ensemble-correlation, are discussed in detail. The resolution limit of PIV is in the focus of Sec. 2.3 and Sec. 2.4 deals with the uncertainty of near-wall velocity profiles.

2.1 Data acquisition

The key elements for PIV measurements are:

- tracer particles, whose motion represents the motion of the fluid of interest,
- a light source that illuminates the particles in the measurement volume, and
- an imaging system that collects the scattered light from the particles and image it onto a camera sensor so that the PIV images can be read out and processed

The working principle of a PIV system is sketched in Fig. 2.1 for the simplest case: Two velocity components are measured in a plane, which is illuminated by a laser light sheet. In order to measure all three velocity components, a stereoscopic system with two PIV cameras is generally used (Westerweel and Nieuwstadt, 1991; Willert, 1997; Prasad and

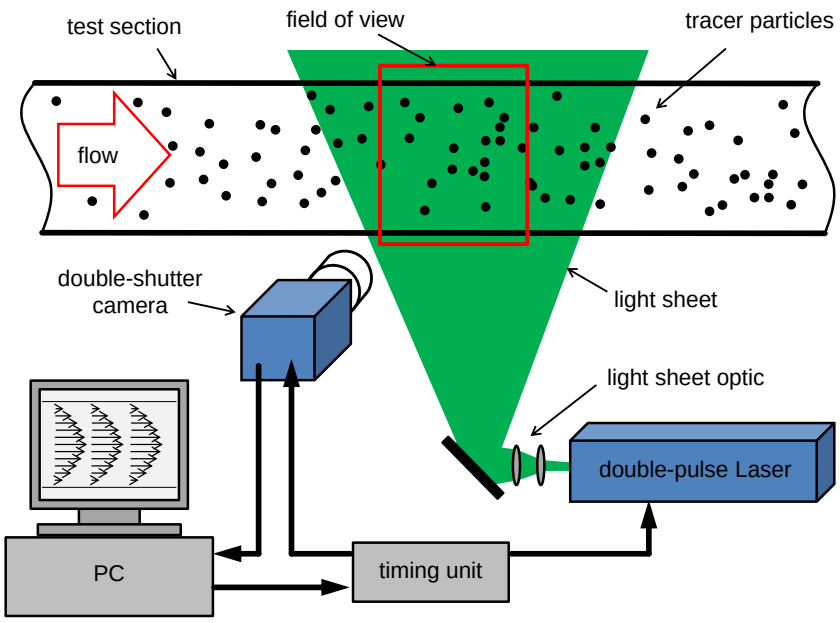

Figure 2.1: Estimation of a velocity field using digital Particle Image Velocimetry.

Adrian, 1993). Furthermore, a tomographic system, consisting of three or more cameras and a volume illumination, reveals all three velocity components in a three dimensional volume (Elsinga et al, 2006).

To measure a velocity field of a certain flow, the three key elements must be adapted to the experimental conditions. The right choice of the key components is a necessary step towards reliable and accurate vector fields. In the following the most important properties of the tracer particles, the light source, and the imaging system are briefly discussed.

2.1.1 Tracer particles

The objective of PIV measurements is to determine the velocity of a transparent fluid in a desired plane or volume. However, not the fluid motion itself is observed but the motion of tracer particles that are seeded into the fluid. Thus, the tracer particles need to follow the fluid motion faithfully in order to estimate the fluid velocity. Therefor, the size of the tracer particles must be small and the mass density ideally matches the fluid's density.

On the other hand, the particle size strongly affects the intensity of the scattered light: For a particle size significantly larger than the wave length of the illuminating light the intensity of the scattered light is proportional to the square of the particle diameter (Mie, 1908). In order to achieve particle images with sufficiently high signal-to-noise ratio (SNR), the particle size should be large, in contradiction to the previous requirement. Additionally,

Table 2.1: Examples of racer particle (Melling, 1997; Raffel et al, 2007)

Material	Mean diameter d_p in µm	Mass density ρ in kg/m^3	Particle shape
Polyamide	$0.5 - 100$	$1.03 \cdot 10^3$	non-spherical
Hollow glass spheres	$10 - 100$	$1.1 \cdot 10^3$	spherical
TiO_2 nano-particles	$0.1 - 5$	$3.5 \cdot 10^3$	non-spherical
DEHS droplets	$0.5 - 1.5$	$0.912 \cdot 10^3$	spherical

the refractive index of the particles must differ from that of the fluid in order to be able to visualize the particles by scattering light, whereas the scatter intensity increases with the ratio of the refractive indexes. Tracer particles with the same refractive index as the fluid are not visible and can therefor not be used for PIV. Due to the fact that the refractive index is dependent on the mass density, it is difficult to achieve matching density and high scatter intensity at the same time (Liu and Daum, 2008).

Due to the relatively large refractive index of water ($n_\mathrm{water} \approx 1.33$ at $\lambda = 532$ nm), the scatter intensity is reduced compared to air flow ($n_\mathrm{air} \approx 1.0$ at $\lambda = 532$ nm) for the same particle size. To achieve reasonably large SNR values for the particle images, the particle size or the laser pulse intensity must be increased. For water flow, particles made of polyamide can be used, their density is close to that of water. Another possible choice are hollow glass spheres, which can be coated with a highly reflective layer.

For air flow, the density can usually not be matched very well (Kähler et al, 2002; Melling, 1997; Meyers, 1991). Liquids and solids, such as DEHS droplets or TiO_2 nano-particles, are used as seeding materials. Due to the large difference in density, the tracers need to be very small in size in order to reduce the velocity lag to an acceptable level (Raffel et al, 2007).

Another important property of tracer particles is their shape. Ideally, the tracers are perfectly spherical to ensure that the particle images look the same for two different laser pulses, even in the case of rotating particles. Among the examples given above hollow glass spheres and DEHS droplets are fairly spherical, whereas polyamide particles are non-spherical but mainly round and TiO_2 nano-particles can have a complex shape. The main properties of the example seeding materials are summarized in Tab. 2.1.

2.1.2 Light source

The light source of a PIV system must provide illumination of the measurement volume with an intensity and wave length that is sufficient to visualize the scattered light of the

Table 2.2: Examples of PIV laser

Laser	Wave length	Repetition rate	Pulse energy	Pulse duration
SpitLight Compact PIV 400 (Innolas GmbH)	532 nm	10 Hz	> 180 mJ	$5 - 7$ ns
EverGreen 200 (Evergreen laser Corporation)	532 nm	$0 - 15$ Hz	200 mJ	< 10 ns
Darwin-Duo-40-M (Quantronix)	527 nm	$0.1 - 10$ kHz	20 mJ (at1 kHz)	120 ns

particles with the imaging system. A pulsed laser with a wave length in the range of green light is often used for PIV measurements for the following reasons:

- pulsed lasers provide a large amount of energy per pulse which is required to visualize the tiny tracer particles with high SNR
- laser light is characterized by small divergence and can therefore be well focused to form a thin light sheet at a defined position
- camera sensors are often most sensitive to green light
- the short pulse duration (in the range of nanoseconds) is used to limit the camera's exposure time, which would be hard to achieve with a electrical or mechanical shutter

Nowadays, flash lamp pumped lasers with a pulse energy of some hundred millijoules can operate at a frequency of ≈ 10 Hz. This is not sufficiently fast for most applications to record a PIV double image, from which the motion of the particle images can be captured. To overcome this problem, PIV lasers are usually equipped with two cavities, which can fire at any time difference. The light beams of the two cavities (both emitting linear polarized light) are overlapped using Brewster windows. The main properties of common PIV lasers are given in Tab. 2.2.

The pulse duration of PIV lasers is typically some nanoseconds for flash lamp pumped ones, or around 100 ns for diode pumped lasers. This is sufficiently short for most applications to ensure nearly round particle images. For the investigation of very fast flow velocities however, this illumination can already be very long and might result in stretched particle images. Since this effect reduces the accuracy, according to Ganapathisubramani and Clemens (2006), special care must be taken in the case of long pulse duration in combination with hypersonic Mach numbers.

An alternative illumination source for PIV measurements is a high-power LED. Willert et al (2010) reported recently LED based PIV measurements with a pulse energy of 400 µJ at a frequency of 2 kHz. For measurements in water, where large tracer particles can be

used, this pulse energy is sufficient. The pulse duration of such high-power LEDs is in the microsecond range, which is only sufficient for fairly small flow velocities.

2.1.3 Imaging system

The PIV imaging system captures the scattered light of the tracer particles and image the measurement plane onto the sensor of the digital camera. It generally consists of a PIV camera, which is capable to acquire two frames in a short time interval, and an objective lens. The most relevant parameters of a PIV camera are:

- inter-framing time, which is the minimum time between two frames
- number of pixels, which limits the dynamic spatial range
- pixel grid spacing, which determines the digital particle image diameter and limits the spatial resolution (see Sec. 2.3)
- recording rate, which limits the temporal resolution
- spectral sensitivity, which must match the laser wave length and determines the SNR together with the
- dynamic range and the
- readout noise

PIV cameras based on CCD technology typically have an inter-framing time in the sub-microsecond range and a sensor with $2 - 11$ million pixel, whereas the pixel grid spacing is below 10 µm (Hain et al, 2007). CMOS cameras are used to capture large ensembles of images in short time. They can acquire double-frame images with a repetition rate in the kilohertz range and typically have a sensor size of $0.5 - 4$ million pixel with a pixel grid spacing around 20 µm. Recently, sCMOS cameras were developed to combine the advantages of CCD and CMOS sensors: They are characterized by sensors with a large number of pixels, which can be readout at higher rates (compared to CCD) with lower noise. Furthermore, the pixel grid spacing is in the same range as that for CCD sensors, leading to reduced peak locking and improved resolution, compared to the large spacing of CMOS cameras. Three example PIV cameras and their main properties are listed in Tab. 2.3.

In front of the PIV camera an objective lens is mounted. The focal length of the lens and the working distance determine the optical magnification. In order to achieve the required size of the field of view, focal length and working distance must be selected taking into account the camera sensor size. To avoid perspective errors, it is important to ensure that the working distance is much larger than the light sheet thickness, according to Raffel et al (2007).

The quality of an objective lens is indicated by the modular transfer function. It determines how much high spatial frequencies (caused by small features) are damped in a optical

Table 2.3: Examples of PIV cameras

Camera	Recording rate	Pixel grid spacing	Number of pixels	Dynamic range
pco.4000 (PCO AG)	5 frames/s	9.0 µm	4008×2672	14 bit
Imager sCMOS (LaVision GmbH)	50 frames/s	6.5 µm	2560×2160	16 bit
Phantom v12.1 (Vision Research)	6242 frames/s	20.0 µm	1280×800	12 bit

system. For reliable PIV measurements with high spatial resolution and a large dynamic spatial range the particle images must be small and the particle image density should be high. Thus, damping of large spatial frequencies must be minimized. Perfect imaging, on the other hand, would result in very small particle images. For low magnifications their size can even be smaller than the sensor pixel spacing, which causes bias errors for the estimation of the particle image displacement. Ideally, the modular transfer function of the lens produces particle images with a diameter in the range of $2 - 3$ px (Adrian and Westerweel, 2010; Raffel et al, 2007).

The aperture of the objective lens strongly affects the transfer function. For most lenses it is adjustable over a wide range and can be used to optimize the particle image size. Whereas, the smallest particle image size is usually achieved for slightly closed aperture (Overmars et al, 2010).

2.2 Data evaluation

Once the tracer particles in the measurement volume are illuminated by the laser pulses and the scattered light is imaged on the sensor of a digital camera, the shift of the particle images between two frames must be linked to the flow velocity using the optical magnification and the time separation between the laser pulses. In order to compute a field of velocity vectors the spatial distribution of the particle image's shift must be determined.

Particle Tracking Velocimetry (PTV) directly estimates the displacement vectors from the location of the particle images (Adrian, 1991; Maas et al, 1993; Ohmi and Li, 2000). If the particle image and its corresponding partner in the second frame can be paired, the shift vector is determined from the difference of the two locations. PTV is well suited for the case of good image quality (high SNR) and low seeding density. The pairing of particle images is complicated by a large shift vector length (required for high accuracy),

by overlapping particle images (likely in the case of high particle image density), and by a large amount of loss of pairs between the two frames (due to out-of-plain motion for instance).

To overcome the limitations of PTV discussed above, correlation based methods were invented. Spatial cross correlation of small sub-figures, hereinafter referred to as window-correlation, and single-pixel ensemble-correlation are two well developed correlation based methods that can deal with overlapping particles, higher seeding densities, lower SNR, and larger amount of loss of pairs, compared to PTV. Window-correlation and single-pixel ensemble-correlation are discussed in detail in the following for the case of planar measurements.

2.2.1 Window-correlation

Figure 2.2 illustrates the working principle of window-correlation based PIV evaluation. The double frame images are divided into small sections, called interrogation windows. Spatial cross-correlation of two corresponding interrogation windows is used to determine the mean motion of the particle images within the window. The correlation function's maximum yields the most common shift between the two interrogation windows. It is estimated with sub-pixel accuracy using a Gaussian fit (Willert and Gharib, 1991). In order to have a high probability to achieve a clear maximum in the correlation function, the window size must be large enough to contain at least $6 - 8$ particle images, whose motion is captured in both frames (Adrian and Westerweel, 2010).

Furthermore, the interrogation window size should be significantly larger than the particle image displacement for the fist pass. It is recommended to choose a window size that is four times larger than the displacement for the fist pass (*one-quarter rule*; Keane and Adrian (1990)).

After the first pass both PIV images are deformed with respect to each other using the shift vector distribution, such that the particle images in both frames are (nearly) overlapping (Scarano, 2001). This procedure compensates for in-plane loss-of-pairs and thus, strongly enhances the SNR of the cross-correlation function for the second pass (and following once). Additionally, image deformation often allows for reducing the interrogation window size, since the *one-quarter rule* is always fulfilled. This increases the spatial resolution and the dynamic spatial range of the estimated shift vector fields. Furthermore, Wereley and Meinhart (2001) showed that image deformation leads to second order accuracy. As a result of this, the computed vectors are aligned tangential to the actual streamline, which is generally not the case without image deformation.

Due to seeding inhomogeneities, out-of-plain motion, imperfect light sheet overlapping, low SNR in the PIV images, and other issues, erroneous shift vectors appear, which must be removed. Westerweel and Scarano (2005) presented a method to identify such outliers, based on the difference of a shift vector and the median of the neighboring vectors for

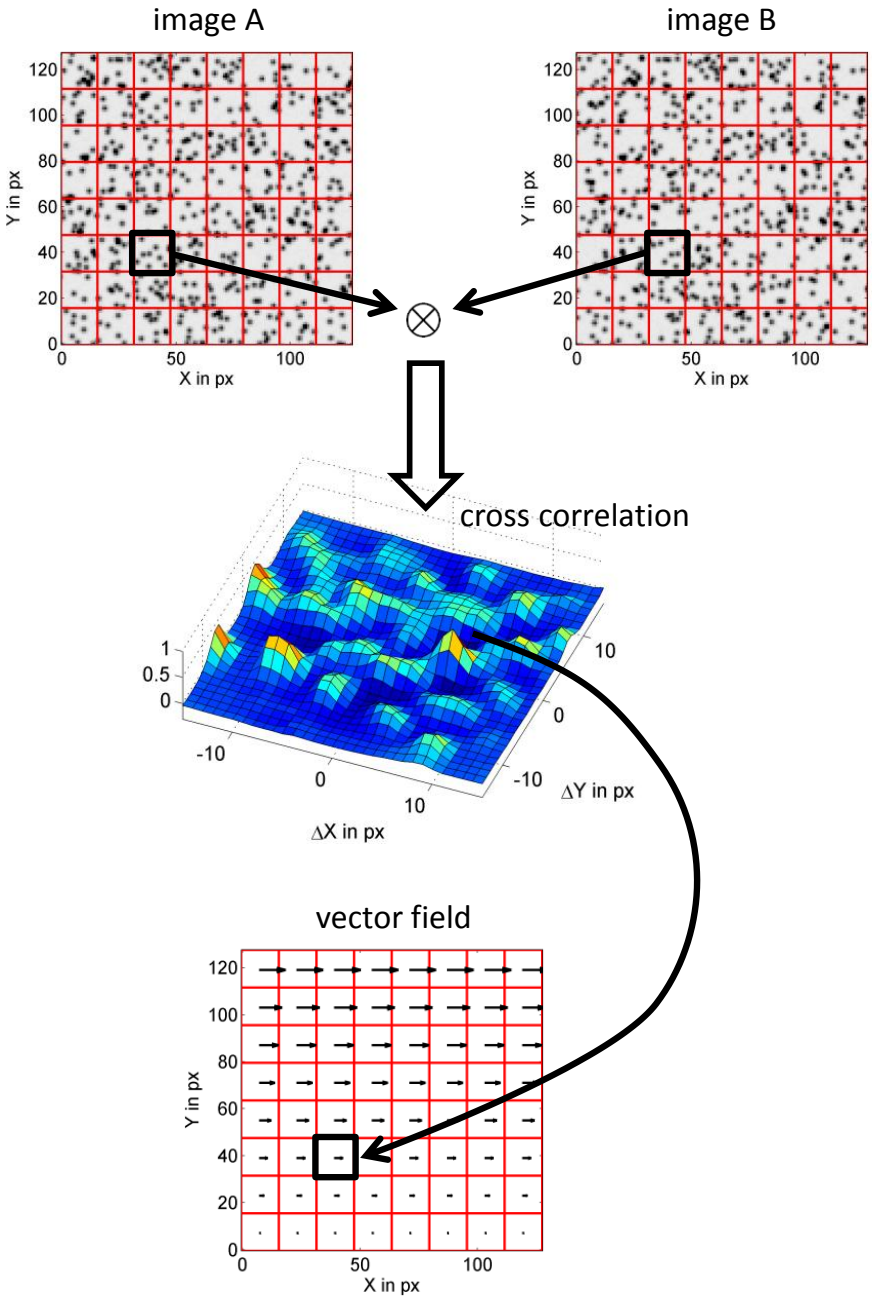

Figure 2.2: Principle of window-correlation PIV evaluation. A double-frame image pair is divided into interrogation windows which are cross-correlated in order to determine the local shift vector.

both components. To further enhance the accuracy of window-correlation and to decrease the number of spurious vectors the correlation function can be weighted with a Gaussian, for instance (Astarita, 2007; Nogueira et al, 2005).

The biggest advantage of window-correlation, compared to single-pixel ensemble-correlation, is that it computes instantaneous shift vector fields, from which individual turbulent structures can be detected. Nevertheless, the method is also used to estimate mean velocity fields as discussed in Meinhart et al (2000). In this case the correlation functions of several image pairs (ensemble) are averaged and the resulting peak position represents the ensemble averaged mean motion. This procedure is commonly called sum-off-correlation evaluation. To compensate for seeding inhomogeneities through the ensemble the correlation functions should be normalized by their standard deviation before added together.

One drawback associated with window-correlation is the relatively low dynamic spatial range, which is usually in the range between 20 and 250. Thus, the range of spatial scales which can be resolved with this technique is rather small. Other drawbacks result from the spatial low-pass filtering that bias the estimation of Reynolds stresses (see Chapter 3).

2.2.2 Single-Pixel ensemble-correlation

Single-pixel ensemble-correlation evaluates a large number of PIV image pairs and estimates the ensemble-averaged mean velocity with enhanced spatial resolution. An ensemble of double frame PIV images is divided into two sets: The first set contains all the first frames $A_\mathrm{n}(X,Y)$ of each image pair and the second set contains the corresponding second frames $B_\mathrm{n}(X,Y)$ that were acquired at Δt after the first one. The double-frame images do not need to be captured at equidistant time steps, but the interval between all image pairs Δt does need to remain constant. The time plot for the image intensity at a certain pixel from the first image set is correlated with the time plot of neighboring pixels in the second set and a correlation function C is generated:

$$C(\xi,\psi,X,Y) = \frac{\sum_\mathrm{n}\left[A_\mathrm{n}(X,Y)-\bar{A}(X,Y)\right]\cdot\left[B_\mathrm{n}(X+\xi,Y+\psi)-\bar{B}(X+\xi,Y+\psi)\right]}{\sigma A(X,Y)\cdot\sigma B(X+\xi,Y+\psi)} \tag{2.1}$$

where the standard deviation is given by:

$$\sigma A\,(X,Y) = \sqrt{\frac{1}{N-1}\sum_\mathrm{n}\left[A_\mathrm{n}(X,Y)-\bar{A}(X,Y)\right]^2} \tag{2.1a}$$

N and n are the total number of PIV image pairs and the corresponding control variable, respectively. (X,Y) are discrete coordinates of the pixel in question in both images and (ξ,ψ) are the coordinates on the correlation plane. The maximum position of the correlation function C represents the mean shift vector with first-order accuracy. The working principle of single-pixel ensemble-correlation is sketched in Fig. 2.3.

Single-pixel ensemble-correlation was first applied by Westerweel et al (2004) for stationary laminar flows in micro-fluidics. In the last years, the approach was extended for the

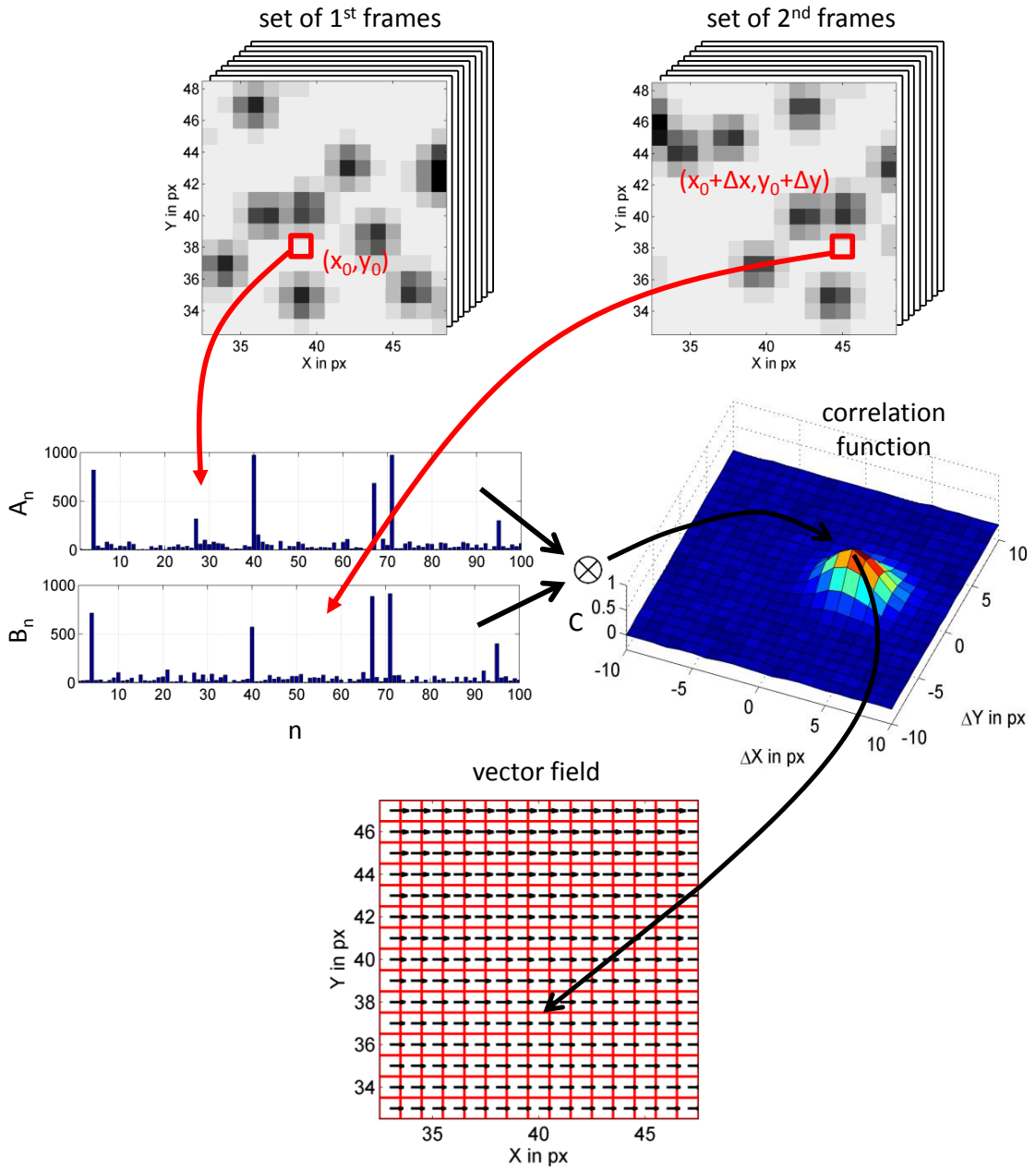

Figure 2.3: Principle of single-pixel ensemble-correlation. A set of double-frame images is used to compute a correlation function for each pixel, whereas the intensity distribution (along the ensemble) of each pixel in the first frame is compared to the distribution of surrounding pixel of the second frame.

analysis of periodic laminar flows (Billy et al, 2004), of macroscopic laminar, transitional, and turbulent flows (Kähler et al, 2006), and for the analysis of compressible flows at large Mach numbers (Bitter et al, 2011; Kähler and Scholz, 2006). Scholz and Kähler (2006) have extended the high-resolution evaluation concept also for stereoscopic PIV recording configurations. Based on the work of (Kähler et al, 2006), the single-pixel evaluation was further expanded to estimate Reynolds stresses in turbulent flows with very high resolution (Scharnowski et al, 2012), which will be in the focus of Chapter 3. Recently, Scharnowski and Kähler (2013) presented a method to compute mean velocity fields with second order accuracy, from which the bias error due to curved stream lines was corrected.

Single-pixel ensemble-correlation evaluates the correlation function for each single pixel of the camera sensor. Thus, this method allows for the estimation of the mean velocity for each single pixel. This results in significantly increased spatial resolution as well as in larger dynamic spatial range, compared to standard-window correlation. However, due to the finite size of the particle images the resolution is always larger than one pixel, as discussed in the following section.

2.3 On the resolution limit of PIV

Due to the recording principle of digital particle image velocimetry, each measured velocity vector represents a volume-averaged mean motion of the discretized and quantized tracer particle's diffraction images, rather than the actual velocity of the flow at $\vec{r}$. This can be expressed by the following equation (Kähler et al, 2012a):

$$\langle u\,(\vec{r},t)\rangle = \int_{\Delta V} G\,(\vec{r},\vec{r}',S)\cdot u\,(\vec{r}',t)\,dV' \tag{2.2}$$

The weighting function $G\,(\vec{r},\vec{r}',S)$ accounts for the intensity and location $\vec{r}'$ of the particle images as well as the discrete sampling due to the digital recording. This weighting function strongly depends on the illumination and imaging system, including the laser beam profile, the camera pixel-grid spacing S, the fill-factor of the camera sensor, the modular transfer function of the objective lens, and the micro-lens array above the CCD/CMOS sensor. The measurement volume ΔV is mainly determined by the interrogation-window size projected in physical space and the light sheet thickness.

Generally, double pulse PIV is not capable of detecting the path and acceleration of the tracer particles, as illustrated in Fig. 2.4. This would require multi-pulse PIV systems as outlined by Kähler and Kompenhans (2000) in combination with multi-frame evaluation techniques as discussed in detail by Hain and Kähler (2007). Therefore, the higher order effects caused by acceleration and curvature must be avoided in double pulse PIV by selecting a sufficiently short time separation Δt between the laser pulses and a sufficiently large magnification M of the imaging system such that the displacement can be resolved

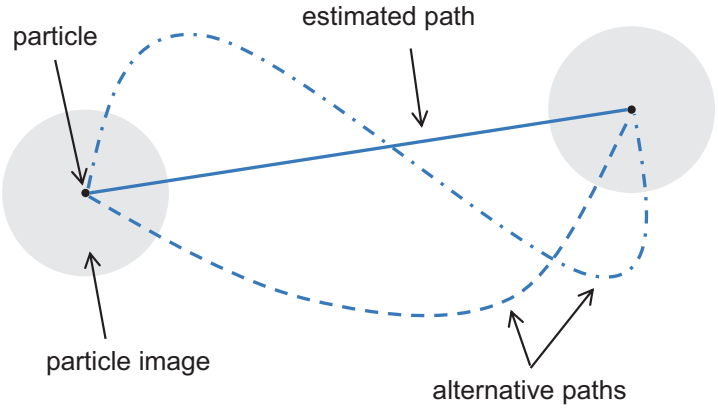

Figure 2.4: Three hypothetical trajectories of a particle (black dot) and its images (gray circles) at the beginning and the end of the motion.

properly. In this case, the first-order approximation of the particle motion, indicated by the straight line in Fig. 2.4 matches well with the true particle motion.

Besides local effects related to individual particles, which are also relevant for particle tracking and molecular tagging techniques, PIV suffers from averaging the motion of several particle images within the interrogation windows. This causes, significant bias errors in the case of varying flow gradients as illustrated in Fig. 2.5 (Keane and Adrian, 1990; Westerweel, 2008).

In order to minimize the errors associated with spatial averaging it is essential, first of all, to acquire proper data with a well aligned system. Secondly, the time interval between the illuminations must be sufficiently short to overcome the problem discussed above. Finally, since this reduces the relative measurement uncertainty (as the particle image displacement becomes smaller, while the precision in estimating the signal peak in the correlation plane is constant), the spatial resolution must be increased to maintain precision for the velocity estimation.

To increase the spatial resolution of PIV systems, as well as its measurement precision, long-range micro-PIV presents a well established method when the observation distance cannot be further reduced or when perspective errors are essential and must be avoided, as outlined in Kähler et al (2006). This technique, used in combination with single-pixel evaluation (see Sec. 2.2.2), seems to increase the resolution beyond the optical limit.

However, although it is possible to compute velocity vectors even in smaller scales than a micrometer grid, these vectors are not independent and bias errors occur in particular situations. Even though many different approaches to increase the accuracy and resolution of PIV were presented (Stanislas et al, 2003, 2005, 2008; Adrian and Westerweel, 2010; Raffel et al, 2007; Stitou and Riethmuller, 2001; Scarano, 2001; Willert, 1997), a detailed

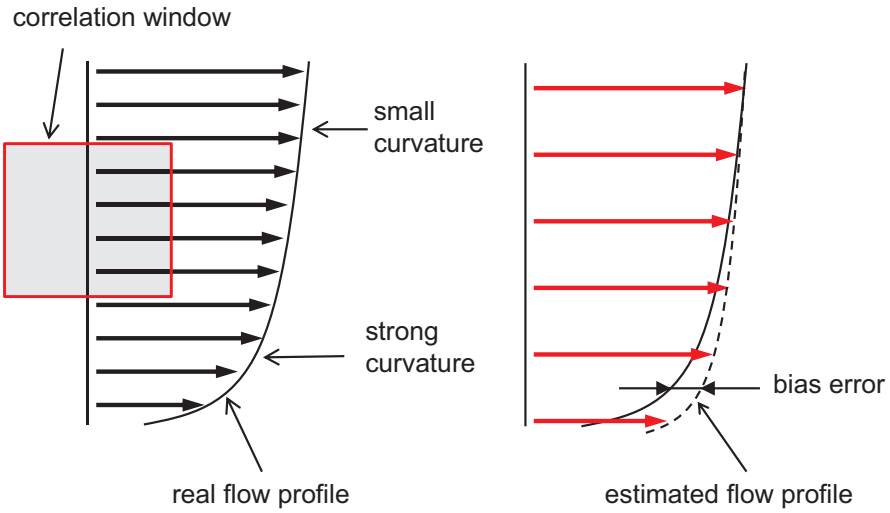

Figure 2.5: Spatial filtering of velocity profiles caused by window-correlation.

analysis of the resolution limit is still lacking and will be the focus of this Section. Section 2.3.1 discusses how a step function is used to determine the spatial resolution of PIV evaluation methods. In Sec. 2.3.2 the particle image size as a function of the optical magnification is analyzed in detail. Synthetic PIV images (Sec. 2.3.3) are used to determine the response to a step-like velocity profile for window-correlation and single-pixel ensemble-correlation (Sec. 2.3.4), in order to identify the dependence of the resolution on the particle image size. Finally, the spatial resolution and the optical magnification are linked together in Sec. 2.3.5.

2.3.1 Step function response

To determine the effective resolution for various interrogation approaches systematically, the resolution limit can be analyzed with a step-like velocity profile:

$$\Delta X^* \left(Y^* \right) = \begin{cases} 1\,\mathrm{px} & Y^* \geq 0 \\ 0\,\mathrm{px} & Y^* < 0 \end{cases} \tag{2.3}$$

Where ΔX^* is the displacement parallel to the intersection line and $Y^*$is the distance from this line. The step response is also frequently used in electrical engineering and control theory to analyze an output's behavior when the input signal changes in a very short time. In order to analyze the PIV resolution, the signal (particle image displacement) is changed in space over a very short distance. The response to a step profile is shown in Fig. 2.6a for window-correlation using four different interrogation-window sizes and for single-pixel ensemble-correlation.

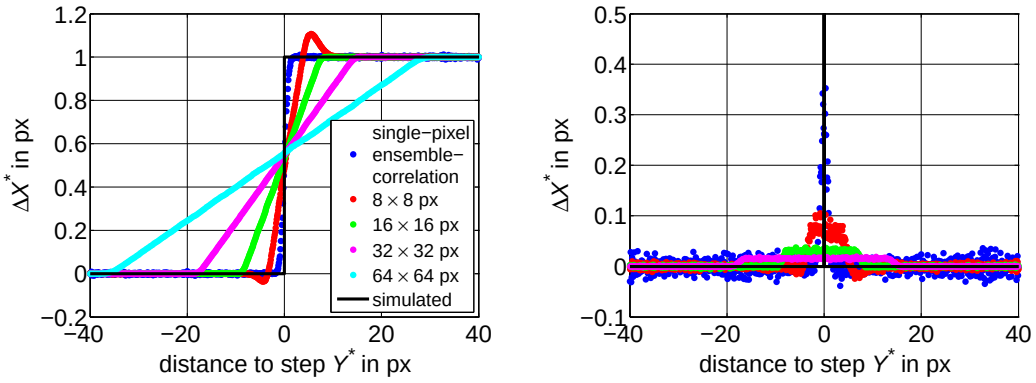

(a) (b)

Figure 2.6: Response to a step-like velocity profile (a) and their corresponding velocity gradients (b) computed with different interrogation-window sizes and with single-pixel ensemble-correlation. A digital particle image diameter of $D = 3\,\text{px}$ was used for the synthetic images.

The width of the response function (Step Response Width or SRW) can be regarded as the resolution, and describes the minimum distance between independent vectors. Only for distances larger than SRW is the vector not biased by the aforementioned flow variations.

Window-correlation leads to a broad response that is dependent on the interrogation-window size. This becomes even more evident when gradient based quantities are considered, as shown in Fig. 2.6b. The gradients are underestimated and their spatial extension is enlarged. It is obvious that this effect leads to systematic errors in estimating the vorticity and other gradient based quantities. The use of weighting functions for the strongly overlapping interrogations windows can improve the spatial resolution to a certain extend. However, independent vectors can be determined with a resolution of about $4 \ldots 5$ pixels only under ideal conditions as shown by Nogueira et al (2005).

Single-pixel ensemble-correlation can drastically reduce the spatial low-pass filtering for the mean shift vector field and is therefore well suited to increase the spatial resolution as demonstrated by Westerweel et al (2004) for laminar flows in micro-fluidics, by Kähler et al (2006) for macroscopic laminar, transient and turbulent flows and Bitter et al (2011) for compressible flows at large Mach numbers. However, it should be noted that it does still not represent the exact solution. The deviation is due to the fact that the measured mean velocity represents the convolution of the particle image (or more precisely, of the particle images' auto-correlation function) and the actual velocity distribution as outlined in Scharnowski et al (2012) (see Chapter 3). Therefore, the question arises: How can the resolution be increased or what is the best spatial resolution that can be achieved by using PIV?

2.3.2 Digital particle image size

By increasing the magnification the resolution of the PIV measurements can be enhanced. However, the imaging of the particles is strongly affected by the optical magnification. The particle image diameter on the image plane is directly related to the particle size itself via the optical magnification. However, it appears enlarged in the PIV images mainly due to four effects:

1. diffraction at the limited aperture of the objective lens
2. defocussing
3. lens aberrations
4. discretization and quantization of the continuous image signal into a discrete signal with pixel-grid spacing S

The enlargement of the particle image due to diffraction and defocussing can be described by the second and third term under the square root of the following equation determined by Olsen (2010):

$$d_\tau = \sqrt{M^2 \cdot d_\mathrm{p}^2 + \left(2.44 \cdot f_\# \cdot \lambda \cdot (M+1)\right)^2 + \left(\frac{M \cdot z \cdot D_\mathrm{a}}{s_0 + z}\right)^2} \tag{2.4}$$

where M is the magnification of the imaging system, d_p the particle diameter, $f_\#$ the ratio between objective lens diameter and the aperture's diameter, λ the wave length of the scattered light (or the fluorescent light in micro-fluidics), z the object's distance from the focal plane, D_a the lens aperture diameter, and s_0 the object distance.

The three terms in the square root of Eq. (2.4) correspond to the geometric, diffraction and defocussing components. The latter shows only significant influence for volume illumination, typically used in micro-PIV (Rossi et al, 2010). In macroscopic PIV z is usually 1 to 3 orders of magnitude smaller than s_0 for well aligned optical systems. In the case of low magnification, the diffraction limited particle image (on the image plane) is smallest and has the lower limit of $2.44 \cdot f_\# \cdot \lambda$ for $M \to 0$. Thus, for a large numerical aperture (small $f_\#$) and a wave length in the range of visible light, the particle images are smaller than the pixel-grid spacing S of the camera sensor, which is typically in the range of $5 - 20\,\mu\mathrm{m}$ for typical CCD or CMOS cameras used for PIV (Hain et al, 2007).

However, after the discretization and quantization of the image by means of the discrete pixels of the digital camera sensor, all particle images will have a size of at least the pixel-grid spacing S. Thus, smaller particle images are artificially enlarged in the case of low magnification. The digital particle image diameter D on the measurement plane is dependent on the pixel-grid spacing S and the particle image diameter d_τ. For particle images with $d_\tau < S$ the digital particle image diameter D is equal to one pixel or slightly larger. Even a very small particle image can illuminate up to four pixel if it is located close to the pixel's corner. However, the probability that a small particle image illuminates only

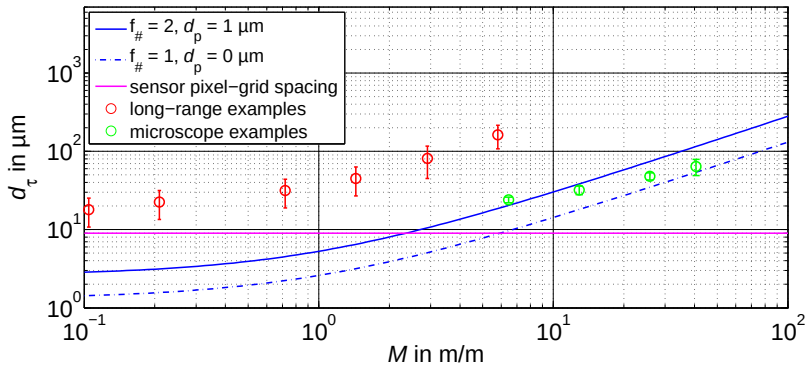

Figure 2.7: Limitation of the particle image size due to diffraction, aberration and discretization.

one single pixel on the sensor is $(S - d_\tau)^2 / S^2$. For particle images larger than one pixel ($d_\tau > S$) the following expression holds:

$$D \approx d_\tau / S \tag{2.5}$$

Figure 2.7 illustrates the effective particle image diameter as a function of the optical magnification for $f_\# = 2$ and $d_\mathrm{p} = 1\,\mu\mathrm{m}$, which is a typical particle diameter for air flow, according to Wernet and Wernet (1994), Melling (1997) and Kähler et al (2002). Additionally, a horizontal line representing the pixel-grid spacing is drawn at $S = 9\,\mu\mathrm{m}$, which corresponds to the $PCO.4000$ camera (by PCO AG), for reference purposes. Only particle image diameters above both curves can possibly exist in reality for this setup. Besides, the theoretical functions are plotted along with experimental results. Where the particle image diameter was measured at $1/\mathrm{e}^2$ of the peak intensity. The experimental results were acquired by using a $Makro - PlanarT * f2/100$ objective lens (by Carl Zeiss AG) combined with up to six tele-converters ($2 \times Pro\,300$ by Kenko Tokina Co., Ltd.) connected to a $PCO.4000$ camera (by PCO AG). The working distance was set to approximately 1 m.

Additionally, the particle image diameters of polystyrene latex particles ($d_\mathrm{p} = 1\,\mu\mathrm{m}$), fabricated by Microparticles GmbH and coated with a red fluorescent dye were analyzed. The particles were observed using a Zeiss Axio Observer.Z1 inverted microscope coupled with a double cavity frequency doubled Litron Nano S Nd:YAG laser (532 nm) for the illumination of the particles. The particle images were recorded with a PCO Sensicam QE camera (by PCO AG). The results are shown for different magnifications in Fig. 2.7. Some example images are illustrated in Fig. 2.8.

The difference between the experimental long-range results and the theory is mainly due to lens aberrations, since the modular transfer function (MTF) is fairly low for the high spatial frequencies caused by the small tracer particles and the large distance. Additionally, according to Eq. (2.4), slightly imperfect focusing leads to further broadening of the

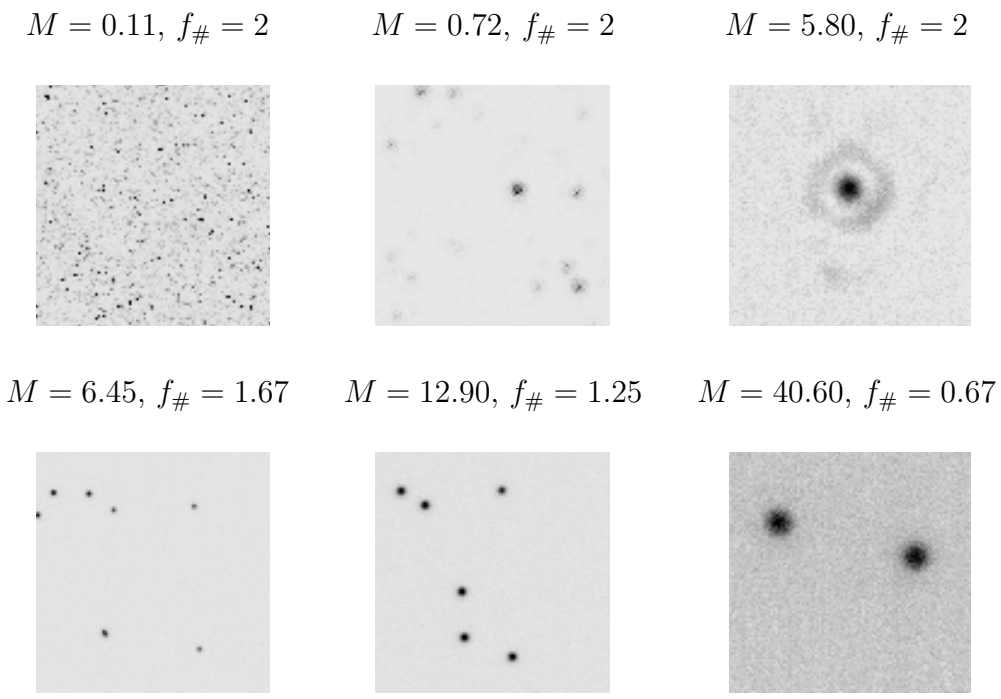

Figure 2.8: Experimental digital particle images captured with different magnifications at a working distance of 1 m (top) and for the microscopic example (bottom) from Fig. 2.7. All images show a sample of 100×100 px.

particle images. However, it is clearly visible in Fig. 2.7 that all the recorded particle images are larger than what the theoretical functions predict. These functions represent the theoretical lower limit for perfect (aberration free) imaging. For the particle imaging with the inverted microscope, for each magnification: $M = [6.45; 12.9; 25.5; 40.6]$ the f-number changes to $f_{\#} = [1.67; 1.25; 0.83; 0.67]$. The working distance is in the millimeter range, thus the modular transfer function is quiet large. Consequently, the particle image diameter is close to the theoretical limit, but still biased by optical aberrations.

2.3.3 Generation of synthetic PIV images

The analysis based on synthetic images gives full control of all simulation parameters and is thus perfectly suited to detect sensitivities and to deduce what is relevant and what is not. All synthetic images were generated using MATLAB® controlling the following parameters: The image size was selected such that the region of interest was surrounded by a several pixel wide margin. The image margins depend on the particle image diameter, the velocity gradient, and the turbulence level. The particle image positions were randomly chosen. A Gaussian particle image shape with the digital particle image diameter D and the maximum intensity I_0 was assumed:

$$I\left(X,Y\right) = I_0 \cdot \exp\left[-8 \cdot \left[\left(\frac{X - X_0}{D}\right)^2 + \left(\frac{Y - Y_0}{D}\right)^2\right]\right] \tag{2.6}$$

Where (X_0,Y_0) is the randomly chosen center position and D is the diameter at $1/\mathrm{e}^2$ of the maximum intensity (4 times the standard deviation).

To reproduce the effect due to the finite pixel-grid spacing of the camera sensor, each pixel's gray value is computed from the integral of the intensity over the corresponding area, instead of simply transferring the analytical point-wise values to the pixel. This integral represents an idealized camera sensor with a fill factor of one, and a constant transfer function. In reality, the transfer function may not be constant due to micro lenses and the design of the sensor, as discussed in Kähler (2004). The intensity distribution of a synthetic PIV image is given by following equation:

$$A\left(X,Y\right) = \sum_{\mathrm{p}=1}^{\mathrm{P}} \left[\int_{X-0.5}^{X+0.5}\int_{Y-0.5}^{Y+0.5} I_{\mathrm{p}}\left(X,Y\right) dxdy\right] \tag{2.7}$$

where P and p are the number of particle images and the corresponding control variable, respectively. The number of the generated particle images depends on the image size and on the particle image density *dens*, which is defined as the fraction of illuminated area by an intensity of $I > I_0/\mathrm{e}^2$. Thus, the particle image density is a function of the digital particle image diameter D. Each particle image occupies an area of $D^2 \cdot \pi/4$, thus, the

number of particle images per pixel N_{ppp} can be computed by:

$$N_{\mathrm{ppp}} = \frac{4 \cdot dens}{D^2 \cdot \pi} \tag{2.8}$$

The particle image positions in the second images were shifted with respect to the position in the first images and the pixels gray values were again computed from the integral of the Gaussian by using Eq. (2.7). On top of the particle image intensities, a Gaussian noise with zero mean and the standard deviation of σ_{n} was added. Thus, the signal to noise ratio is given by:

$$\mathrm{SNR} = \frac{I_0}{\sigma_{\mathrm{n}}} \tag{2.9}$$

Finally, the intensity distribution was converted into a 16 bit unsigned integer matrix to account for the discrete nature of PIV images.

2.3.4 Resolution limit

The response to a step-like velocity profile (as shown in Fig. 2.6a) is well suited to determine the spatial resolution of the estimated velocity field. Such a strong local change does exist in reality in the form of contact layers in supersonic flows or shear layers in micro-fluidic mixers. Velocity distributions in high speed shear layers and phase boundaries of two-phase flows, for instance, also represent a step-function as particles are statistically not present directly at the interface (Kähler et al, 2012a).

Window-correlation - resolution limit

In the case of window-correlation, 1,000 synthetic image pairs, 256×256 px in size, were generated for each particle image diameter considered in this analysis. The images were divided in two parts: one with zero velocity and one with a particle image motion of one pixel. The intersection line was slightly tilted ($1:20$) with respect to the image grid and the shift was applied parallel to this line to produce results for random sub-pixel locations. The particle image density was 25% in each case, meaning that 25% of the image area was illuminated by particle images. Consequently, the number of particles changes with the particle image diameter (according to Eq. (2.8)), as it does in real PIV recordings for magnified images and constant seeding concentration. The maximum intensity of the particle images was set to 1,000 counts and a signal-to-noise ratio of $\mathrm{SNR} = 100:1$ was simulated by means of a background noise with Gaussian distribution. Some example images are shown in Fig. 2.9.

The evaluation of the data was performed using a sum-of-correlation approach proposed by Meinhart et al (2000) without window weighting using 16×16 px interrogation windows with 87% overlap. Fig. 2.10a shows the estimated displacement ΔX^* parallel to the

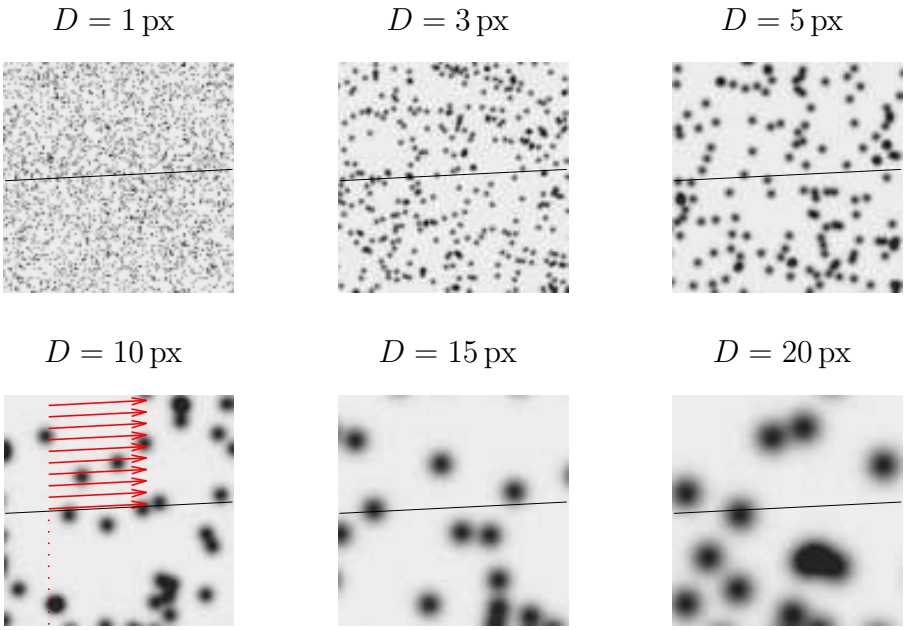

Figure 2.9: Synthetic images for the step-response test with different digital particle image diameters D. The intersection between the two velocity regions is indicated by the black solid line. All images show a sample of $100 \times 100\,\mathrm{px}$.

intersection line with respect to the distance Y^* from this line. It is clearly visible that the step response width SRW strongly depends on the interrogation-window size, as already illustrated in Fig. 2.6a, but interestingly also on the size of the particle images as can be seen in Fig. 2.10a. The response function becomes broadened (and also more noisy) for larger particle images. Hence, sum-of-correlation evaluation allows for reducing the interrogation-window size down to approximately four times the particle image diameter. For further reduction, SRW increases with D. It is important to note that the use of smaller interrogation windows does not gain any additional spatial resolution.

Single-pixel ensemble-correlation - resolution limit

In the case of single-pixel evaluation, more images are required (Westerweel et al, 2004; Scharnowski et al, 2012), and thus 10,000 image pairs were generated for each particle image diameter considered in this analysis. For each pixel the correlation-function was computed using Eq. (2.1) on page 21. The mean shift vector was estimated with a 3-point Gauss-fit. Figure 2.10b shows the resulting displacement ΔX^* parallel to the intersection line with respect to the distance Y^* from this line. The estimated displacement profiles

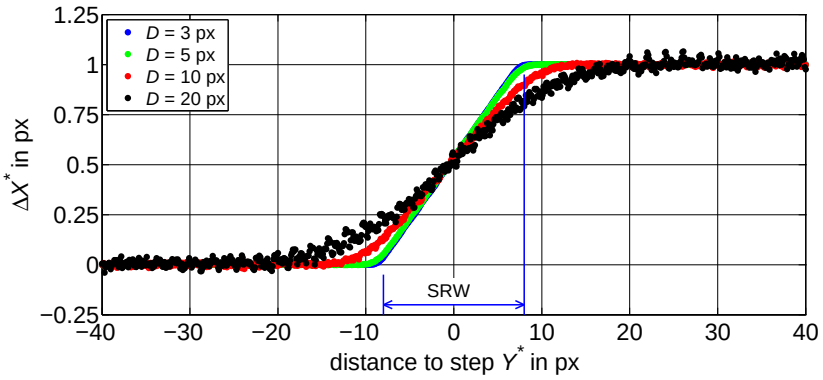

(a)

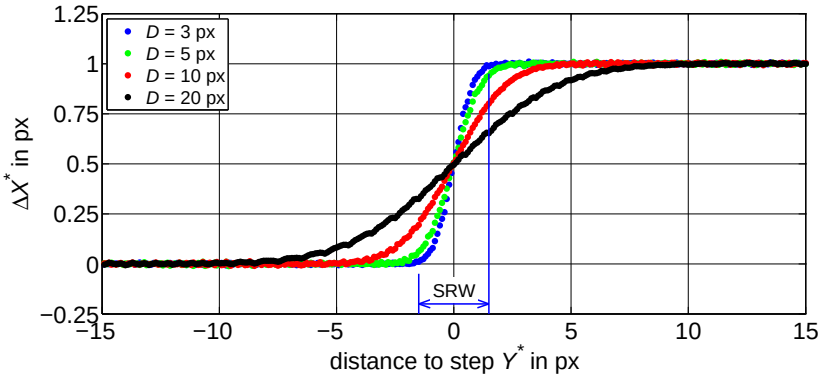

(b)

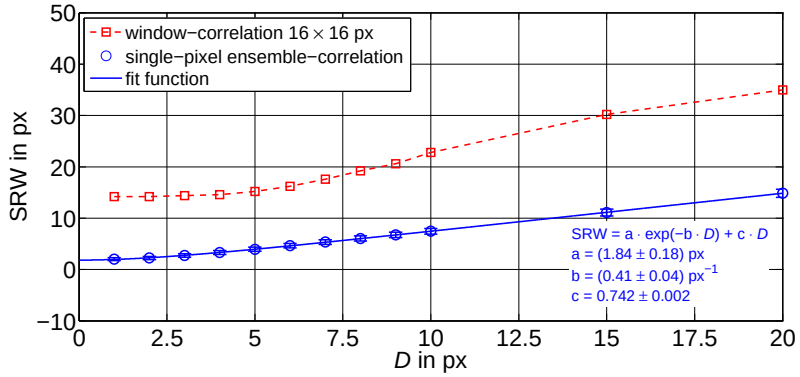

(c)

Figure 2.10: Response to a step-like velocity profile for different digital particle image diameters computed with averaged window-correlation using 16×16 px interrogation windows with 87% overlap (a) and single-pixel ensemble-correlation (b) as well as the step response width of the estimated displacement with respect to the digital particle image diameter (c).

are compared to an error function in order to estimate the width of the response functions:

$$\Delta X^*\left(Y^*\right) = \frac{\Delta X_0}{2} \cdot \left(\operatorname{erf}\left[\frac{8 \cdot Y^*}{SRW}\right] + 1\right) \tag{2.10}$$

where SRW is the width that covers $\operatorname{erf}\left(\sqrt{2}\right) \approx 95\%$ of the total step height and ΔX_0 is the step height. Figure 2.10c shows the fitted width as a function of the simulated digital particle image diameter. The lower limit of the fit function shown in Fig. 2.10c is at 1.84 px. This means that even the smallest particle images (one pixel for PIV) result in a step response width of 1.84 px. Consequently, it can be concluded from the present analysis that the best possible resolution that can be achieved in PIV is around 1.84 px instead of a single-pixel. Furthermore it is interesting to note that for large particle images, the resolution (defined by the step response width) is proportional to the particle image diameter. This result is consistent with the assumptions of Adrian (1997).

2.3.5 Guidelines and recommendations

Figure 2.10c summarizes the results of the response to the simulated step-like displacement profile. Using window-correlation the step response shows the known dependence on the window size, but also on the digital particle image diameter as can be seen on the red curve in Fig. 2.10c exemplary for a 16×16 px interrogation window. It is well known, that an additional error in the velocity estimation is present due to truncated particle images. The use of weighting functions and the removal of these truncated particle images can decrease this error significantly as shown by Nogueira et al (2001) and Liao and Cowen (2005). However, reducing the interrogation-window size, only few and most likely truncated particle images are present and thus, these techniques do not improve the results any further. If the digital particle image diameter increases to approximately one quarter of the interrogation-window size, a significant influence from particles, which were partly captured in the interrogation window is visible and the SRW increases drastically. For a particle image size of 10 pixel, which can easily happen by increasing the magnification, the SRW increases from approximately 16 pixel to almost 23 pixel, for instance.

Also in the case of single-pixel ensemble-correlation, the step response indicates a dependence on the digital particle image diameter D. By using a curve fitting, the following relationship:

$$SRW\left(D\right) > 1.84\,\text{px} \cdot \exp\left(-0.41 \cdot D\right) + 0.742 \cdot D \tag{2.11}$$

limits the resolution to about 1.84 px.

Resolution

Combining the relationship between step response width SRW, digital particle image diameter D, and optical magnification M allows for the determination of the resolution

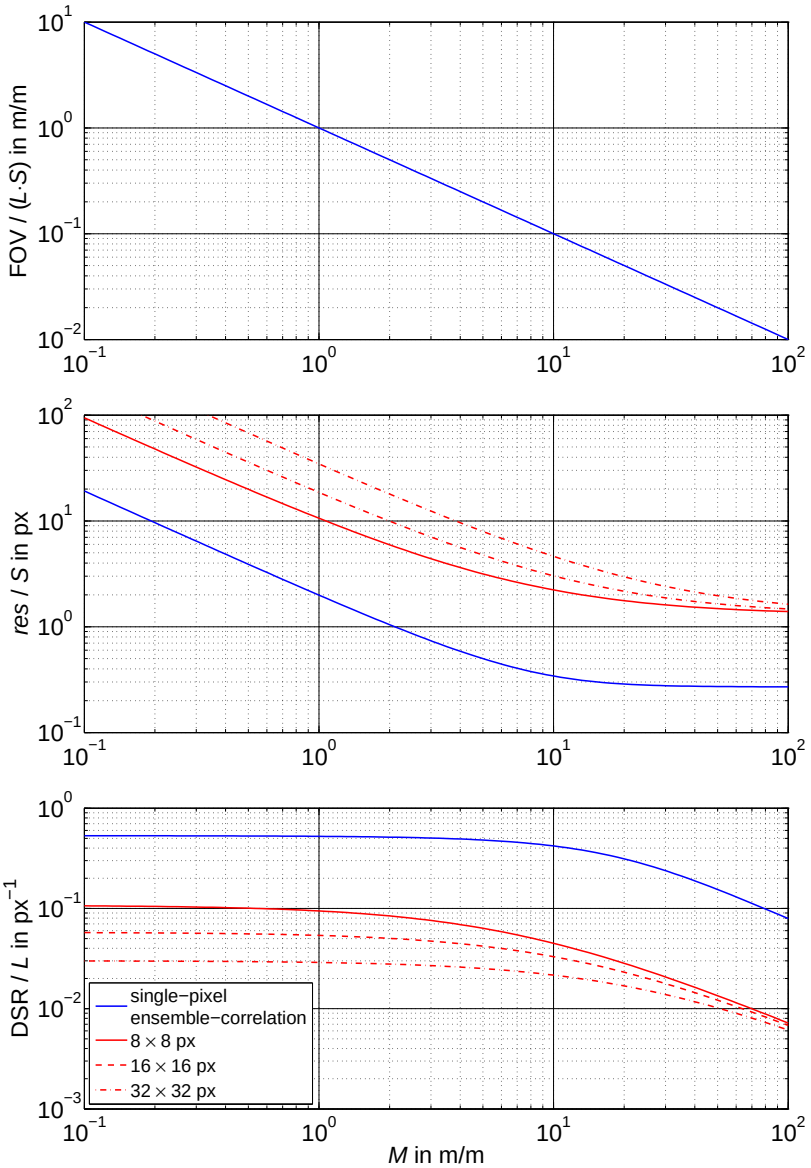

Figure 2.11: Field of view (top), limits of spatial resolution (middle) and dynamic spatial range (bottom) as functions of optical magnification for $d_\mathrm{p} = 1\,\mu\mathrm{m}$ and $f_\# = 2$.

res on the measurement plane in physical space:

$$res\,(M) = SRW\,(D\,(M)) \cdot \frac{S}{M}. \tag{2.12}$$

The normalized resolution is shown in the middle plot of Fig. 2.11 for window-correlation and single-pixel ensemble-correlation. The graph shows the lower limit of the resolution (minimum distance of independent vectors) determined by the step response width from Fig. 2.10c and the digital particle image size defined in Eq. (2.4). The resolution limit in the case of window-correlation is shown for three different interrogation-window sizes (red lines) and is approximately one order of magnitude above the single-pixel ensemble-correlation. For low magnifications and sufficient particle image density ($5 - 10$ particle images per interrogation window) the red lines are also valid for instantaneous shift vector estimation. The distance between independent vectors becomes larger in case of lower particle image density or of strong lens aberrations, as they occur for large working distances, as well as in the case of out-of-focus particles or larger f-numbers.

In order to estimate the resolution limit, res, from Fig. 2.11 the pixel-grid spacing of the camera sensor must be taken into account. For a pixel-grid spacing of $S = 9\,\mu m$, for example, the resolution is limited to $res > 0.3 \cdot 9\,\mu m = 2.7\,\mu m$ in the case of single-pixel ensemble-correlation (solid blue line), which is reached with a magnification of 10 or higher. For low magnifications like $M = 0.1$, for instance, the resolution limit lies at around $200\,\mu m$ (for single-pixel ensemble-correlation).

For particle tracking velocimetry the distance of independent mean vectors is theoretically not limited. Since the resolution is independent on the particle image diameter, using higher magnification would increase the resolution of the measurement even when particle images are very large. Especially for microscopic applications of large magnification, PTV is the only well suited approach (Kähler et al, 2012a).

Dynamic spatial range

Combining the field of view (upper plot in Fig. 2.11) and the resolution (middle plot of Fig. 2.11) allows for the estimation of the dynamic spatial range (DSR) by following the work of Adrian (1997):

$$DSR = FOV/res. \tag{2.13}$$

This relation is plotted in the lower chart of Fig. 2.11, normalized by the sensor size (number of pixel L). In the case of single-pixel ensemble-correlation (blue line) a $PCO.4000$ camera with $L = 4{,}008$ would lead to a maximum dynamic spatial range of $DSR = 0.5 \cdot 4{,}008 \approx 2{,}000$ for a magnification lower than $M = 2$, for example. Since in the case of window-correlation the distance of independent vectors is larger than for single-pixel ensemble-correlation, the dynamic spatial range is smaller for this evaluation method. For very low magnifications ($M \ll 1$), both correlation based methods show a constant DSR value. This is due to the fact that the particle images reaches their minimum size of

slightly more than one pixel. Working in this region of very small magnification might also cause peak locking.

The dynamic spatial range of particle tracking velocimetry is in principle independent on the optical magnification. However, optimal conditions for PTV are a low seeding density and fairly large particle images, as discussed in Kähler et al (2012a).

2.4 On the uncertainty of PIV near walls

The determination of the velocity profiles near walls is a very important task and a challenging problem in many fields of science and technology. In the case of a backward-facing step flow, for instance, the incoming boundary layer strongly affects the Reynolds stresses in the separated region (Eaton and Johnston, 1981). For a turbulent boundary layer flow the velocity profiles are typically normalized with the friction velocity u_τ defined as:

$$u_\tau = \sqrt{\frac{\tau_w}{\rho}} \tag{2.14}$$

where ρ is the fluid density. Since the wall-shear stress τ_w is given by:

$$\tau_w = \lim_{y \to 0} \mu \frac{\partial \bar{u}}{\partial y} \tag{2.15}$$

where μ is the viscosity of the fluid, the precise determination of the mean flow gradient $\partial\bar{u}/\partial y$ down to the wall is very important for the comparison of experimental, theoretical, and numerical results (Alfredsson et al, 2011; Bitter et al, 2011; Fernholz and Finley, 1996; Marusic et al, 2010; Nagib et al, 2007; Nickels, 2004).

In order to resolve the flow field near walls and interfaces it is important:

1. to sample the flow motion down to the wall with appropriate tracer particles which follow the fluid motion faithfully, as discussed by Kähler et al (2002), Melling (1997), Wernet and Wernet (1994),
2. to use fluorescent particles as typically done in micro fluids (Santiago et al, 1998) or a tangential illumination along a properly polished wall (Kähler et al, 2006), such that the wall reflection is not superimposed to the particle image signal,
3. to image the particles properly with a lens or a microscope objective such that the particle signal can be well sampled on a digital camera (Adrian, 1997; Hain et al, 2007),
4. to estimate the particle image displacement with digital particle imaging methods.

The mean velocity profile can be estimated with averaged window correlation (sum-of-correlation), single-pixel ensemble-correlation, or particle tracking velocimetry. The first two methods will be in the focus of this section. Synthetic PIV images are used to

demonstrate the capability of the different evaluation methods. Section 2.4.1 describes the synthetic images and in Sec. 2.4.2 and 2.4.3 the images are evaluated using window-correlation and single-pixel ensemble-correlation to assess systematic errors in the vicinity of the wall. Section 2.4.4 shows the impact of the resolution limit on the estimation of the near-wall velocity for a turbulent boundary layer flow experiment.

2.4.1 Synthetic boundary layer

A fundamental analysis of a synthetic image set is performed for three reasons: First, it gives full control of all parameters considered for the simulation (as opposed to experiments where many uncertainties exist such as local density, temperature, viscosity, flow velocity, particle properties, illumination power and pulse to pulse stability, local energy density in the light sheet, imaging optics, recording medium, and bias effects due to data transfer which are unknown or cannot be precisely controlled as can be done with simulations). Second, the variation of single parameters is possible (which is often difficult to do in experiments because of the mutual dependence of the parameters like light intensity and signal-to-noise ratio, optical magnification and lens aberrations, ...). Third, the range of the parameters can be increased beyond the range accessible experimentally (higher shear rates and turbulence levels, higher particle concentrations, ...).

The major drawback of the synthetic image approach is that not all physical effects can be simulated properly because of a lack of physical knowledge and the fact that each experimental setup is unique. Thus, experiments are always necessary to prove the main predictions and sensitivities of the simulations and to estimate the uncertainty of the simulation relative to the experiment (Kähler et al, 2012b). This will be done in Sec. 2.4.4.

In order to determine the main sensitivities and the measurement uncertainty for velocity vectors close to the surface, synthetic PIV images with different digital particle image diameters were generated and analyzed. The digital particle image diameter varied from $D = 1\,\mathrm{px}$ (which is typical for experiments in air with large observation distances) up to $D = 20\,\mathrm{px}$ (which is common in experiments with large magnification), as illustrated in Fig. 2.12. 10,000 image pairs were generated for each digital particle image diameter. The seeding concentration was about 25%, meaning that 25% of the image was composed by particle images. Consequently, the number of particle images changes with the digital particle image diameter according to Eq. (2.8). The maximum intensity of the particle images was set to 1,000 counts and a signal-to-noise ratio of 100 : 1 was applied.

A displacement profile with a constant gradient of $\partial\Delta X/\partial Y = 0.1\,\mathrm{px/px}$ was simulated to illustrate the effects and main sensitivities. The surface was located several pixels away from the border of the PIV images and was slightly tilted (1 : 20) with respect to the image boarder to simulate the wall location at sub-pixel positions. Only particle images with a random center position above the simulated surface were generated. Even though all particle centers are located above the wall, their images can extend into the region below the wall. This effect is illustrated in Fig. 2.12, where the synthetic images in the near-wall

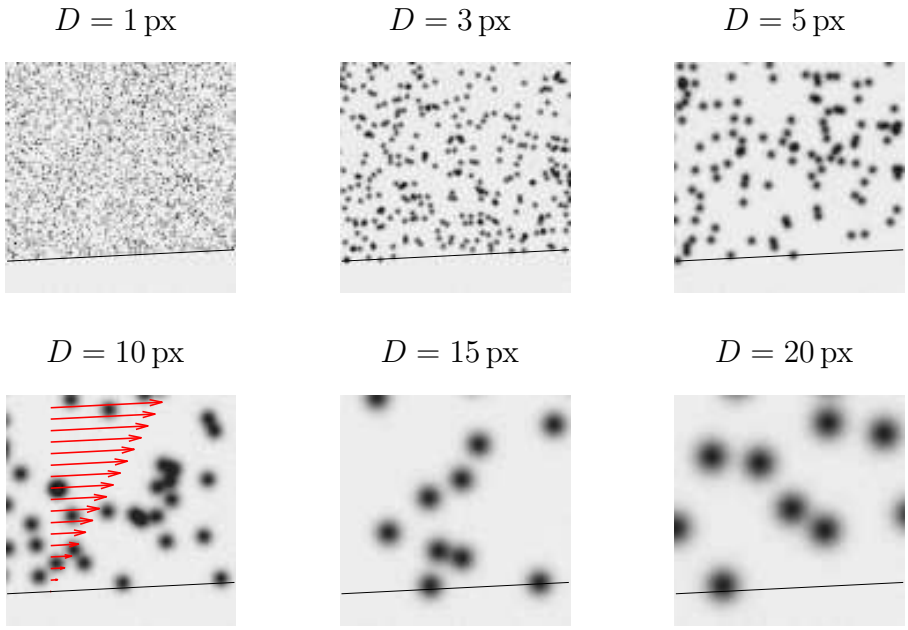

Figure 2.12: Synthetic images of a near-wall boundary layer for different digital particle image diameters D. The surface position is indicated by the black line. $100 \times 100\,\mathrm{px}$ are shown in each case.

region of the boundary layer are shown for different digital particle image diameters D. In the following discussion these images are analyzed by using averaged window-correlation and single-pixel ensemble-correlation.

2.4.2 Window-correlation

The window-correlation based evaluation was performed for a digital particle image diameter of $D = 3\,\mathrm{px}$, which is close to the optimal value to achieve low uncertainties (Raffel et al, 2007). Four different interrogation-window sizes ranging from $8 \times 8\,\mathrm{px}$ to $64 \times 64\,\mathrm{px}$ were applied. The evaluation was performed by using a commercial software ($DaVis$ by LaVision GmbH) with a sum-of-correlation approach (Meinhart et al, 2000). For each interrogation-window size, 100 image pairs were analyzed.

The resulting wall-parallel and wall-normal shift vector components ($\triangle X^*$, $\triangle Y^*$) are shown in Fig. 2.13 as a function of the wall-normal image coordinate Y^*.

Since the simulated surface was slightly tilted, the investigation covers also sub-pixel distances. For larger window sizes, the typical systematic bias error becomes prominent for the estimated wall-parallel shift vector component $\triangle X^*$. Its magnitude is a function of the correlation window dimension in the wall-normal direction.

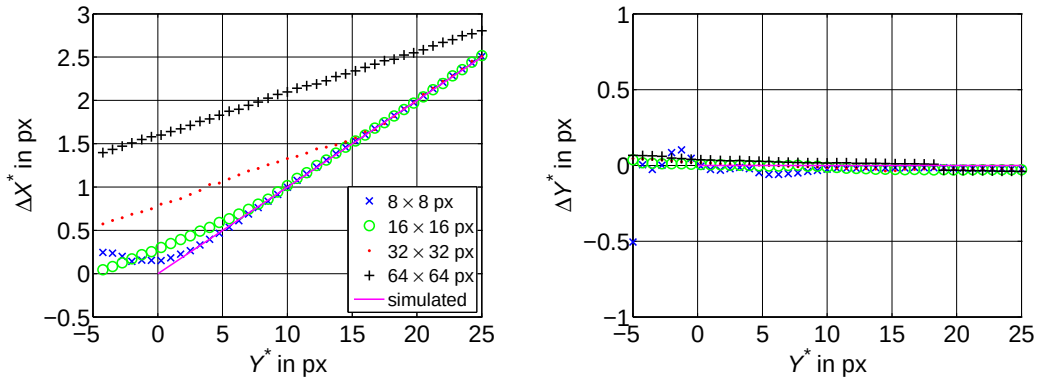

(a) (b)

Figure 2.13: Estimated displacement profile of the wall-normal (a) and wall-parallel (b) shift-vector component for a simulated constant gradient in the near-wall region of a boundary layer using window-correlation for different digital particle image diameters.

The wall-parallel shift vector component is overestimated for locations that are closer to the wall than half the height of the interrogation window. The strong bias error is due to the fact that the mean particle image displacement, averaged over the interrogation window area, is associated with the center position of the window if no vector reallocation is performed. Therefore, even under ideal conditions (constant flow gradient, homogeneous particle image distribution, identical particle image intensity and size), no reliable near-wall displacement can be expected for distances smaller than half the interrogation window dimension in the wall-normal direction. For the 16×16 px interrogation window, for example, vectors located below $Y^* = 8$ px are biased.

The magnitude of the systematic error of the wall parallel shift vector component $\delta\overline{\triangle X}_{\mathrm{wall}}$ at the wall position $Y^* = 0$ px is dependent on the interrogation window height W_{Y} and the mean gradient $\partial\overline{\triangle X^*}/\partial Y^*$ in the near-wall region. Without compensating for inhomogeneous particle image distribution the following bias error occurs:

$$\delta\overline{\triangle X}_{\mathrm{wall}} = \frac{W_{\mathrm{Y}}}{4} \cdot \frac{\partial\overline{\triangle X^*}}{\partial Y^*} \tag{2.16}$$

In this simple model, the interrogation window centered at $Y^* = 0$ px is, on average, only half occupied with particle images. Thus, the mean displacement within this window is equal to the wall parallel shift vector component at $Y^* = W_{\mathrm{Y}}/4$ for constant gradients. The vertical displacement component, shown on the right hand side of Fig. 2.13 is not systematically affected since $\partial\overline{\triangle X^*}/\partial Y^*$ is constant. For the case of a non-constant shift vector gradient, an additional bias error on the estimated shift vector is expected, which scales with the profile's curvature and the interrogation-window size. It is important to note that shift vectors below the surface are computed although no particle images were

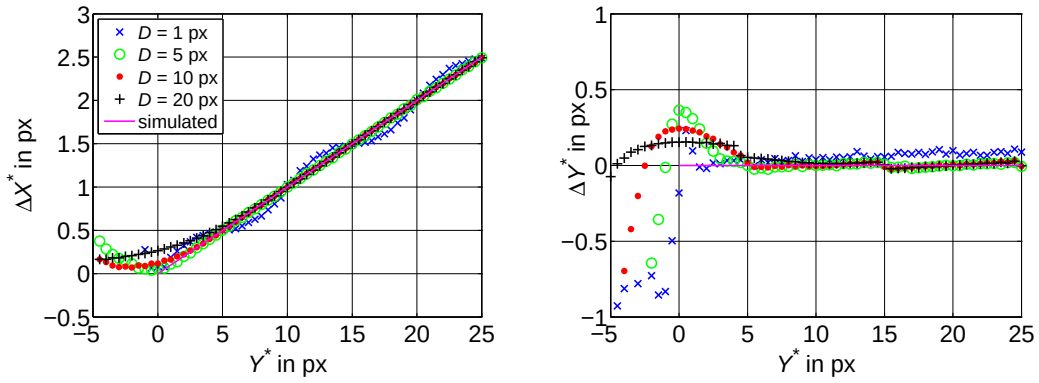

(a) (b)

Figure 2.14: Estimated displacement profile of the wall-normal (a) and wall-parallel (b) shift-vector component for a simulated constant gradient in the near-wall region of a boundary layer using single-pixel ensemble-correlation for different digital particle image diameters.

generated in this region. This is because the interrogation windows centered below the surface are still partly filled with the images of the particles located above the surface. When the wall location is known the vectors can be easily rejected. However, in the case of a tangential illumination or fluorescent particles the wall is not visible at all and the wall detection may become problematic. It is obvious that a proper reallocation of the vectors must be made and a suitable alignment and optimized size of the interrogation windows must be used to minimize these effects. However, this is difficult to achieve close to solid surfaces and interfaces as the ideal conditions (constant flow gradient, homogeneous particle image distribution, straight walls ...) do not generally hold in real experiments.

2.4.3 Single-pixel ensemble-correlation

In the case of single-pixel ensemble-correlation analysis, the limitations associated with the window-correlation evaluation approach do not appear as the interrogation-window size can be reduced to a single pixel. However, although the flow is sampled up to a single pixel the resolution is limited by the digital particle image diameter, as discussed in Sec. 2.3. The single-pixel ensemble-correlation was performed for different digital particle image diameters ranging from $D = 1\,\text{px}$ to $20\,\text{px}$ using 10,000 PIV image pairs. The correlation functions were computed Eq. (2.1) and the maximum of the correlation peak was determined using a three point Gauss estimator for each direction.

Figure 2.14 shows the estimated wall-parallel and wall-normal displacement components with respect to the wall-normal distance Y^* for $D = [1,3,10,20]$ px. The wall-parallel component is strongly biased for the digital particle image diameter of $D = 1\,\text{px}$ due to

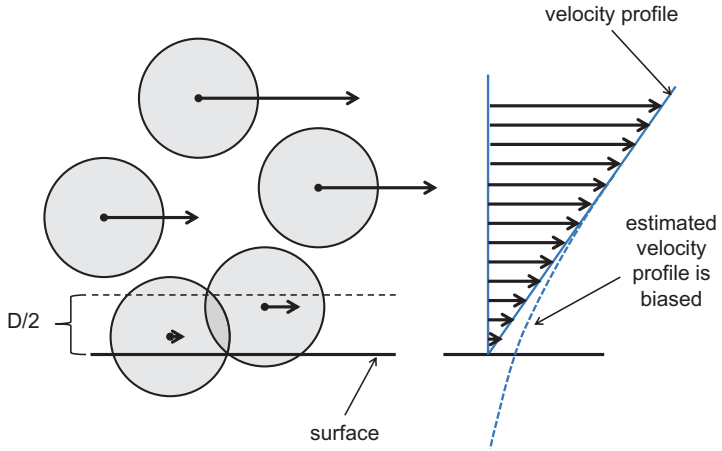

Figure 2.15: Motion of particles (dark dots) and particle images (gray circles) in the near-wall region. The estimated velocity profile is biased within a distance of $D/2$ from the surface.

the peak locking effect, which is a systematic error caused by the discretization of the measured signal (Raffel et al, 2007; Adrian and Westerweel, 2010). As the peak locking has a dramatic effect on the higher order statistics of velocity profiles according to Christensen (2004), measurements with a significant amount of small particles are not suited for high precision flow analysis and should be considered with care. For $D = 3\,\mathrm{px}$, peak locking can also be observed but with a much lower magnitude. Obviously, no peak locking is visible for larger particle images in agreement with Raffel et al (2007).

Figure 2.14(right) illustrates that the wall-normal component of the displacement vectors close to the wall are significantly overestimated. This is due to the fact that the correlation peaks at the wall are influenced by particle images corresponding to particles traveling within a distance of $Y^* \leq D/2$ from the wall with a higher local displacement as discussed above and illustrated in Fig. 2.15. The influence of these particle images results in a bias error towards higher velocities.

The estimated velocity profile $\overline{\Delta X}_{\mathrm{estimated}}(Y)$ is biased due to the evaluation principle of single-pixel ensemble-correlation. To explain this result Eq. (2.1) can be transformed in an analytical expression which shows that $\overline{\Delta X}_{\mathrm{estimated}}(Y)$ is the convolution of the normalized auto-correlation of the particle image $R(D,Y)$ and the actual velocity profile $\overline{\Delta X}_{\mathrm{true}}(Y)$ (Scharnowski et al, 2012). For the wall normal direction this can be described in the following 1-D equation:

$$\overline{\Delta X}_{\mathrm{estimated}}(Y) = \int_{-\infty}^{\infty} R(D,Y-\psi) \cdot \overline{\Delta X}_{\mathrm{true}}(\psi)\,\mathrm{d}\psi \tag{2.17}$$

In order to estimate the difference between the true and the measured shift vector

component the integral in Eq. (2.17) must be solved for a specified auto-correlation and a velocity profile. The diffraction limited image of a tiny particle in Fraunhofer approximation can be described by a Gaussian intensity distribution function and, due to the fact that the auto-correlation function of a Gaussian is a Gaussian, broadened by a factor of $\sqrt{2}$, we can write:

$$R\left(D,Y\right) = \frac{2}{D \cdot \sqrt{\pi}} \cdot e^{-\frac{4Y^2}{D^2}} \tag{2.18}$$

The normalization by the factor before the exponential term in Eq. (2.18) ensures that the integral over Y equals one. The simulated displacement profile with constant gradient used in this analysis can be described as follows:

$$\overline{\triangle X^*}_{\text{true}}\left(Y^*\right) = \Theta\left(Y^*\right) \cdot Y^* \cdot \frac{\partial \overline{\triangle X^*}_{\text{true}}}{\partial Y^*} \tag{2.19}$$

Where $\Theta\left(Y^*\right)$ represents the Heaviside step function. Using Eqs. (2.18) and (2.19) for the normalized auto-correlation and the simulated displacement profile, respectively, results in the following estimated shift vector profile:

$$\overline{\triangle X^*}_{\text{estimated}}\left(Y^*\right) = \frac{\partial \overline{\triangle X^*}_{\text{true}}}{\partial Y^*} \cdot \left[\frac{D}{4\sqrt{\pi}} \cdot e^{-\frac{4Y^2}{D^2}} + \frac{1}{2}\left(1 + erf\left[\frac{2Y^*}{D}\right]\right)\right] \tag{2.20}$$

For large distances from the wall ($Y^* \gg D$) the Gaussian in Eq. (2.20) becomes zero and the error function becomes one. Thus, the estimated shift vector is not biased in the case of homogeneous seeding and constant gradients:

$$\overline{\triangle X^*}_{\text{estimated}}\left(Y^* \gg D\right) = \frac{\partial \overline{\triangle X^*}_{\text{true}}}{\partial Y^*} \cdot Y^* = \overline{\triangle X^*}_{\text{true}}\left(Y^*\right) \tag{2.21}$$

On the other hand, the velocity profile is strongly biased in the vicinity of the wall. The magnitude of the systematic error of the wall-parallel shift vector component $\delta\triangle X^*_{\text{wall}}$ at the position of the wall at $Y^* = 0\,\text{px}$ is proportional to the digital particle image diameter D and the mean gradient $\partial\overline{\triangle X^*}/\partial Y^*$ in the near-wall region:

$$\delta\triangle X^*_{\text{wall}} = \overline{\triangle X^*}_{\text{estimated}}\left(Y^* = 0\right) = \frac{D}{4\sqrt{\pi}} \cdot \frac{\partial \overline{\triangle X^*}_{\text{true}}}{\partial Y^*} \tag{2.22}$$

The analytical bias error is in good agreement with the simulated values within the shift vector profiles in Fig. (2.14). Thus, from the theoretical point of view it seems possible to compensate for the bias error produced by the correlation procedure. However, in the case of real PIV images the inhomogeneous particle image distribution and the real shape of the velocity profile is not generally known. Furthermore, the deconvolution of the discrete values computed from digital images is a mathematically ill-posed problem.

It is interesting to note that the wall-normal component ΔY^* is also biased in the near-wall region because the particle images further away from the wall broaden the correlation peak only on the side facing away from the surface. In the case of flows with constant gradients and ideal conditions (homogeneous particle image distribution, ...) this effect is averaged out as long as the particle is at least $Y^* > D/2$ away from the wall. It should be noted that, this effect reverses for positions below the wall. Some correlation peaks in the vicinity of the wall are shown in Fig. (2.16).

the wall-shear stress τ_w can be estimated directly from the first values above the wall which are not biased according to equation (2.20). Now the experimenter has to determine if the positions of these first reliable vectors are close enough for the estimation of the wall-shear stress, i.e. they belong to the viscous sublayer of a turbulent boundary layer flow, for instance, or not.

The comparison of the two evaluation techniques showed significant differences for the estimated shift vector profiles of the synthetic near-wall flow with constant gradient. Figure 2.17a summarizes the results using a digital particle image diameter of $D = 5$ px for window-correlation and single-pixel ensemble-correlation. In the case of window-correlation, an interrogation window size of 16×16 px was used. It can clearly be seen from Fig. 9 that the biased region extends to $Y^* \approx 8$ px for window-correlation, whereas the biased region and the bias error itself are much smaller in the case of single-pixel ensemble-correlation.

For the estimation of the wall-shear stress, the mean near-wall gradient is determined from the shift vector profiles. Figure 2.17b shows the gradient $\partial\overline{\triangle X^*}/\partial Y^*$ of the profiles from Fig. 2.17a with respect to the wall-normal distance. Each point in Fig. 2.17b represents the slope of a linear fit-function applied to three points of the profile. The error bar corresponds to the 95% confidence interval of the fit parameters. Again, the size of the biased region strongly depends on the applied evaluation technique.

Based on these results, it can be concluded that for the estimation of the near-wall gradient, the only shift vectors that can be used are those that have a distance normal to the surface larger than

- half the interrogation window size in the case of window-correlation (without vector reallocation) and
- half the particle image diameter in the case of single-pixel ensemble-correlation.

Additionally, the selected shift vectors must belong to the viscous sublayer such that the normalized wall distance y^+ is not larger than five and the displacement must be large enough for a reliable estimation as the slope of the gradient depends on both the location and velocity at the same time.

Therefore, it is often more accurate to use particle imaging techniques than LDV or hotwire probes for the analysis of flows with strong velocity gradients. LDV or hotwires are more precise than single-pixel PIV in estimating the velocity; however, the error in estimating the exact location of the measurement volume is much larger. For single-pixel PIV, in contrast, the locations of the particles are precisely known from the image analysis.

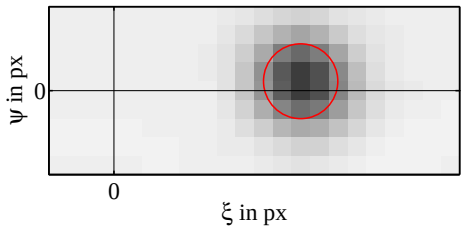

(a) $Y^* = 100\,\mathrm{px}$

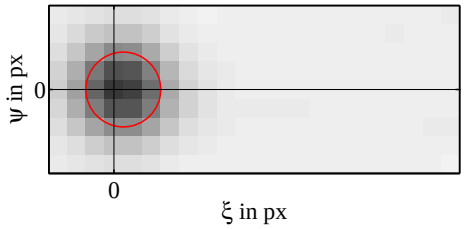

(b) $Y^* = 3\,\mathrm{px}$

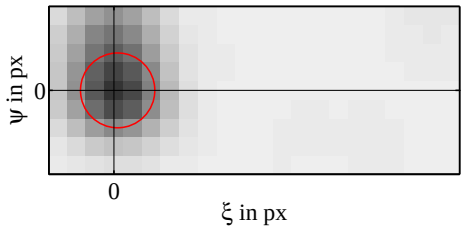

(c) $Y^* = 0\,\mathrm{px}$

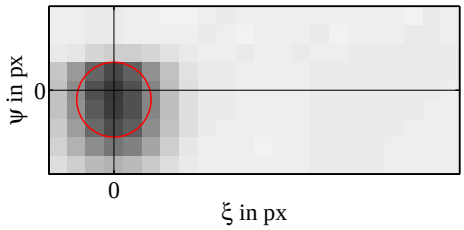

(d) $Y^* = -3\,\mathrm{px}$

Figure 2.16: Correlation functions in the vicinity of the wall for $D = 5\,\mathrm{px}$ and $\partial\overline{\triangle X^*}/\partial Y^* = 0.1\,\mathrm{px/px}$.

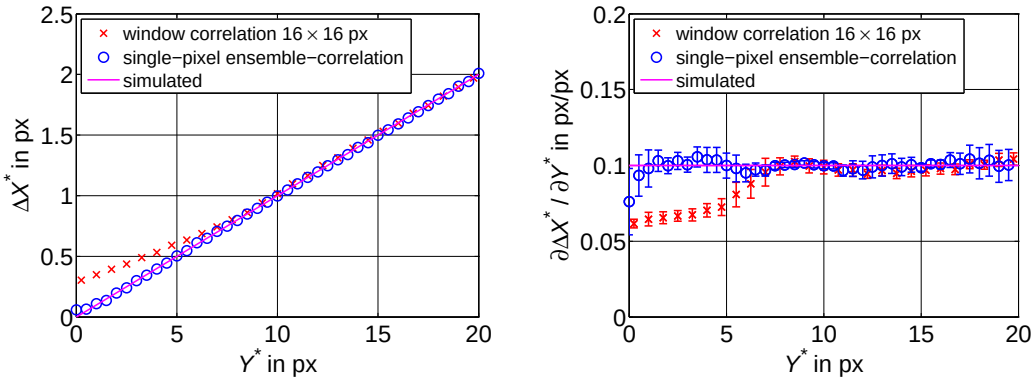

Figure 2.17: Comparison of the different evaluation methods: profile of the estimated horizontal shift vector component (a) and its gradient (b) computed using window-correlation and single-pixel ensemble-correlation. The particle image diameter was $D = 5$ px.

2.4.4 Experimental example

To demonstrate the suitability of single-pixel ensemble-correlation for the investigation of a turbulent boundary layer, an experiment was performed in the large-scaled Eiffel type wind tunnel (AWM) located at the Universität der Bundeswehr in Munich. The facility has a 22 m long test section with a rectangular cross-section of $1.8 \times 1.8\,\mathrm{m}^2$. The model is composed of wooden plates and features a super-elliptical nose with a 0.48 m long semi-axis in the stream-wise direction. The flow was tripped 300 mm behind the leading edge of the plate by a sandpaper strip. The measurements were performed 3 m downstream of the leading edge. Three DEHS particle seeders producing fog with a mean particle diameter of $d_\mathrm{p} = 1\,\mu\mathrm{m}$ (Kähler et al, 2002) were used to sample the flow. The light sheet for illuminating the particles was generated by a Spectra Physics Quanta-Ray PIV 400 Nd:YAG double-pulse laser. For the flow measurements, a *PCO*.4000 camera in combination with a Zeiss makro-planar objective lenses with a focal length of 100 mm was used. The results presented here are taken at 6 m/s free stream velocity, which corresponds to a Reynolds number based on momentum thickness at the measurement location of $Re_{\delta_2} = 4{,}600$. A detailed description of the experimental set-up is outlined by Dumitra et al (2011).

In order to resolve the complete boundary layer velocity profile, a large field of view was selected which extends almost 25 cm in the wall-normal direction. The particle image concentration is relatively high and the digital particle image diameter is in the range of $D = 2 \ldots 3$ px. These conditions are well suited for the single-pixel ensemble-correlation according to Fig. 3.4b on page 62.

In Fig. 2.18a the boundary layer velocity profile evaluated with single-pixel ensemble-

correlation is shown. The profile represents the stream-wise velocity, averaged in stream-wise direction over a length of $x = 7.6\,\mathrm{mm}$. In total 2,300 double frame images were processed. For the current magnification the resolution in the wall-normal direction is 230 µm which gives a spatial dynamic range of 1,000 independent velocity vectors. In normalized wall units the resolution corresponds to $y^+ = y \cdot u_\tau/\nu \approx 4$ and the first data points are already at the limit of the viscous sub-layer ($y^+ \leq 5$). Due to the large field of view and the high dynamic spatial range, which corresponds to the number of independent vectors in each direction, the boundary layer thickness could also be reliable estimated: $\delta_{99} = (130 \pm 4)$ mm. Thus, the relative uncertainty in estimating this quantity is about 3%. However, precisely measuring the mean flow gradient $\partial\bar{u}/\partial y$ down to the wall is not possible as the viscous sublayer ($y^+ < 5$) is not resolved sufficiently, as shown in the normalized semi-logarithmic representation in Fig. 2.18b. By using the method of Clauser (1956), the wall-shear stress can be estimated from the logarithmic region of the boundary layer profile by means of the following equation:

$$\frac{u\,(y)}{u_\tau} = \frac{1}{\kappa} \cdot \ln\left(\frac{y \cdot u_\tau}{\nu}\right) + B \tag{2.23}$$

The uncertainty of this approach is that the value of the constants $\varkappa$ and B are generally unknown. $\varkappa$ and B depend on the Reynolds number, the pressure gradient of the flow and other parameters. For flows along smooth walls and zero pressure gradient, typical values are $\varkappa = 0.41$ and $B = 5.1$. In this case u_τ becomes $0.248\,\mathrm{m/s}$ and the wall-shear stress $0.076\,\mathrm{N/m^2}$. Here, the estimation of $\varkappa$ and B from the logarithmic region of the velocity profile results in different values when using a fit function, see Fig. 2.18b, as $\partial p/\partial x$ is not exactly zero.

To avoid the uncertainty of this Clauser approach in general, a better spatial resolution is necessary to directly resolve the wall-shear stress according to Eqs. (2.14) and (2.15). A better spatial resolution can be achieved by PTV, as demonstrated in Kähler et al (2012b).

Conclusions

The impact of a localized flow gradient (a step function) on the resolution limit of PIV was examined in detail using window-correlation and single-pixel ensemble-correlation evaluation methods. It was shown that in the case of window-correlation the resolution is strongly dependent on the interrogation-window size whereas for single-pixel ensemble-correlation it depends on the particle image diameter instead.

The particle image diameter has a lower limit, which is determined by the particle size, the pixel-grid spacing of the camera sensor, the f-number of the imaging system and optical aberrations. Experimental particle images values for varying magnifications are always larger than the theoretical limits derived. In the case of a large working distance (1 m) the diameter is enlarged by almost one order of magnitude due to lens aberrations. The

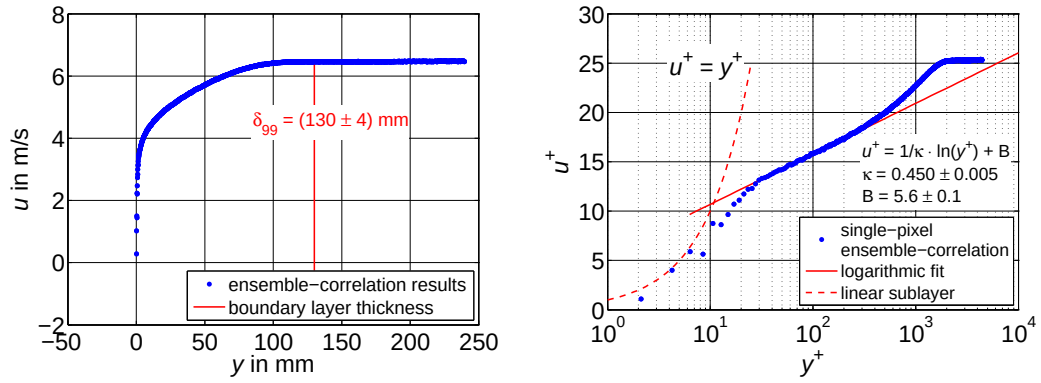

(a) (b)

Figure 2.18: Estimated velocity profile of a turbulent boundary layer using single-pixel ensemble-correlation with a resolution of $res = 230\,\mu m$ and a dynamic spatial range of DSR > 1,000 in the direction normal to the wall.

analysis shows that the resolution cannot be reduced below a certain point which is defined by the particle size, the pixel-grid spacing and the f-number. Magnifications larger than $M = 10$ do not seem to further improve the resolution for typical experimental conditions ($f_\# = 2$ and $d_p = 1\,\mu m$) since the particle images grow linearly with the magnification.

Furthermore, the dynamic spatial range decreases with increasing magnification. In order to achieve results with the best possible spatial resolution and dynamic spatial range by means of correlation based methods, it is recommended to: (1) use the smallest possible working distance (by taking perspective errors into account), (2) select a high quality objective lens with low f-number, (3) use a camera with small pixel-grid spacing and a large sensor, (4) acquire a sufficient amount of PIV recordings for single-pixel or sum-of-correlation evaluation. The best resolution in terms of independent velocity vectors is nevertheless limited for correlation-based methods. For large magnifications, the resolution saturates at a value that depends on the particle size, the pixel-grid spacing of the camera, the f-number of the objective lens, and lens aberrations.

The strong advantage of window-correlation is the possibility to measure instantaneous velocity fields. This allows for the use of gradient based analysis tools as well as correlation and spectral approaches to analyze the instantaneous velocity fields. In this case, however, the resolution is diminished when estimating mean velocities. However, the resolution is limited by the same parameters with the addition of the seeding concentration. In this case, the particle image size and density determine the interrogation-window size that directly influences the resolution. At least $6 - 8$ particle images are required per interrogation window to limit the number of spurious vectors to an acceptable level. For a digital particle image diameter of $D = 3\,px$ and a seeding concentration of 25%, the interrogation-window size should be larger than $14 \times 14\,px$. Since the resolution of correlation-based methods is limited by the particle image diameter, it should be possible, in principle, to increase the

resolution with an appropriate pre-processing method that reduces the particle image size.

The analysis of synthetic PIV images of a near-wall flow with constant gradient shows that the estimation of the wall-parallel velocity component depends strongly on the evaluation technique. Accurate estimations are only possible within the bounds of the resolution limit of each method: The window-correlation evaluation is limited by the interrogation-window size. In the case of the single-pixel evaluation the particle image size is the major limitation for the resolution and bias errors appear only for wall distances smaller than the diameter of the particle image. In order to reduce the uncertainty of the velocity estimation near walls or interfaces beyond the limit of single-pixel ensemble-correlation PTV evaluation is required, as demonstrated in Kähler et al (2012b).

3 Reynolds stress estimation up to single-pixel resolution

This chapter derives a theory for estimating Reynolds normal and shear stresses from PIV images using single-pixel ensemble-correlation. The main idea is the analysis of the correlation function to identify the probability density function from which the Reynolds stresses can be derived in a $2D$ regime.

Standard window-correlation estimates the Reynolds stresses directly from an ensemble of velocity fields after subtracting the mean field from each sample. These vector fields are obtained from the spatial cross correlation of interrogation windows of each PIV image pair (see Sec. 2.2.1). Thus, the resolution of the Reynolds stresses is limited by the size of the interrogation windows used for the cross correlation. This means that the computed values only represent an average over the corresponding interrogation area and that strong spatial changes, as the ones that occur in boundary and shear layers or separated regions, are smeared out. Hence, the finite interrogation-window size acts as a low-pass filter.

Reducing the window size to enhance the spatial resolution leads to higher measurement noise and thus to an artificial amplification of the Reynolds stresses. On top of that, the number of spurious vectors increases (Raffel et al, 2007). A good compromise between accuracy and resolution often is a window size between 16×16 px and 32×32 px, depending on the particle image's size and density.

The single-pixel ensemble-correlation can be used to improve the spatial resolution for mean velocity fields without lowering the measurement precision, but does not allow for computing an ensemble of independent vector fields. Thus, statistical information about the flow cannot be extracted in the same way as for window-correlation.

However, statistical variables can be extracted from the shape of the correlation peak. Kähler and Scholz (2006) suggested a method for estimating (symmetrical) normally distributed turbulence from the size of the correlation peak. A fully optical approach was performed by Arnold et al (1986) by analyzing the visibility in speckle velocimetry. Both examples indicate that the probability density function of the velocity can be used to extract the statistical information about the variance of the flow.

This chapter will show how to quantitatively estimate the Reynolds normal and shear stresses from the shape of the single-pixel ensemble-correlation function. The chapter is divided into three main sections. Section 3.1 discusses the relationship between the probability density function and the correlation function in an analytical way. An analytical

equation for the correlation function is derived in order to determine the influence of velocity gradients, the digital particle image diameter, and the shape of the probability density function on the correlation function. This is followed by a systematic investigation of synthetic PIV recordings in Sec. 3.2, where the accuracy and the applicability of the new method is studied. Finally, the developed approach is applied to an experimental example to show the benefit of the increased spatial resolution.

3.1 Mathematical description

Since the correlation function can be computed for each single-pixel of the PIV images using the single-pixel ensemble-correlation, the suggested method allows for the estimation of the in-plane components of the Reynolds stress tensor for each single pixel. For a sufficiently large ensemble of PIV image pairs, the shape of a correlation peak is similar to the convolution of the particle image's auto-correlation and the probability density function of the velocity. Without stresses, this peak is narrow and has a distinct maximum. In the case of Reynolds normal stresses, the correlation peaks become broader and shear stresses lead to an asymmetrical shape. The connection between the shape of the correlation function and the existing Reynolds stresses is discussed in this section.

The two-dimensional velocity field is described as follows:

$$\vec{v}(x,y,t) = \langle \vec{v}(x,y) \rangle + \vec{v}'(x,y,t) = \begin{pmatrix} \langle u(x,y) \rangle + u'(x,y,t) \\ \langle v(x,y) \rangle + v'(x,y,t) \end{pmatrix} \tag{3.1}$$

Where $\langle \vec{v}(x,y) \rangle$ and $\vec{v}'$ are the mean velocity and the corresponding velocity fluctuation, respectively. The mean velocity can be estimated with single-pixel ensemble-correlation. However, there is no direct access to the temporal development of the velocity fluctuations, but statistical values of the fluctuations can be computed from their probability density function.

The joint probability density function $PDF(u,v,x,y)$ among the two velocity components includes all occurring velocities for a given point (x,y) over a certain time (or for an ensemble of measurements) and allocates the related probability. Hence, it is possible to compute the Reynolds normal and shear stresses using the probability density function of the velocity field given by:

$$\left\langle u'(x,y)^2 \right\rangle = \int PDF(u,v,x,y) \cdot u'^2 \mathrm{d}u\, \mathrm{d}v \tag{3.2a}$$

$$\left\langle v'(x,y)^2 \right\rangle = \int PDF(u,v,x,y) \cdot v'^2 \mathrm{d}u\, \mathrm{d}v \tag{3.2b}$$

$$\langle u(x,y)' \cdot v(x,y)' \rangle = \langle v(x,y)' \cdot u(x,y)' \rangle = \int PDF(u,v,x,y) \cdot u' \cdot v'\, \mathrm{d}u\, \mathrm{d}v \tag{3.2c}$$

The integration limits are $-\infty$ or $+\infty$, respectively. Equations (3.2a), (3.2b), and (3.2c) must now be multiplied by the mass density in order to provide the actual Reynolds stresses. For simplicity, the expected values of the fluctuation products will be identified as Reynolds stresses here. Equations (3.2a), (3.2b), and (3.2c) are valid for any normalized PDF, hence the challenge that remains lies in solving the integrals. Furthermore, the most important task is to identify the probability density function from the correlation peak. Therefore, the shape of the correlation peak, as a function of the PDF, will be analyzed in the next section.

3.1.1 A general analytical expression of the correlation function

In the following analysis the variables for the position vector and other quantities are used on both, the measurement plane in physical space and the image plane (camera sensor). Lower case letters (x,y,...) refer to quantities on the measurement plane and upper case letters (X,Y,...) denote quantities on the image plane. The position vectors on the two planes are directly related via the magnification M of the imaging system and the pixel-grid spacing S of the camera sensor:

$$(X,Y) = (x,y) \cdot M/S \tag{3.3}$$

The velocity on the measurement plane is transferred into the shift vector on the image plane:

$$(\Delta X,\Delta Y) = (u,v) \cdot \Delta t \cdot M/S \tag{3.4}$$

For single-pixel ensemble-correlation, the correlation function $C(\xi,\psi,X,Y)$ can be computed by using Eq. (2.1) on page 21. In order to analyze the shape of the correlation function for a fixed point (X,Y) in the image plane, Eq. (2.1) is converted into an analytical expression: A cross-correlation integral of the two images A and B replaces the sum in Eq. (2.1). The discrete images A_n are replaced by one continuous Gaussian peak representing the particle image intensity distribution:

$$A_\mathrm{n}(X,Y) \rightarrow A(X,Y) = \exp\left(-\frac{X^2+Y^2}{D^2} \cdot 8\right) \tag{3.5}$$

The parameter D in Eq. (3.5) is the digital particle image diameter at $1/e^2$ of the maximum intensity. Although the Gaussian intensity profile is a good approximation (Born and Wolf, 2000), the derivation can also be based on any other shape, if necessary. However, finding an analytical expression for the correlation function might become more difficult.

The images B_n are also replaced by a single Gaussian, but two things are different compared to A_n: first, they are shifted due to the particle mean motion and secondly, they are convolved (denoted by $*$) with the probability density function $PDF(X,Y)$ of the velocity

to include velocity fluctuations:

$$B_{\mathrm{n}}(X,Y) \rightarrow B(X - \Delta X\,(X,Y)\,,Y - \Delta Y\,(X,Y)) * PDF(X,Y) \tag{3.6}$$

with

$$B(X - \Delta X\,(X,Y)\,,Y - \Delta Y\,(X,Y)) = \exp\left(-\frac{(X - \Delta X\,(X,Y))^2 + (Y - \Delta Y\,(X,Y))^2}{D^2} \cdot 8\right) \tag{3.6a}$$

By using Eq. (3.5) and (3.6), the correlation function from Eq. (2.1) can be transformed into an analytical expression:

$$C(\xi,\psi,X,Y) \sim A\,(X,Y) \star [B\,(X,Y) * PDF\,(X,Y)] = \int A\,(X - \xi,Y - \psi) \cdot \left[\int B\,(\mu - \Delta X(\mu,\eta),\eta - \Delta Y(\mu,\eta)) \cdot PDF\,(X - \mu,Y - \eta)\,\mathrm{d}\mu\mathrm{d}\eta\right] \mathrm{d}X\mathrm{d}Y \tag{3.7}$$

Where $\star$ denotes the cross correlation and $*$ the convolution. In Eq. (3.7), the sum of Eq. (2.1) was replaced by an integral. This ensures that all possible locations of the particle image, with respect to the point of interest, were considered and simulates a perfectly uniform particle image distribution. μ and η are the control variables for the convolution integral. The coordinates (X,Y) are on the image plane and (ξ,ψ) correspond to the correlation plane. The integration limits are $-\infty$ or $+\infty$, respectively.

Generally, it is only required to compute the theoretical equation for the correlation function and apply this as a fit-function to the experimental data in order to identify the probability density function.

3.1.2 Reynolds stresses for a specified PDF

Equation (3.7) gives a universal expression for a correlation function. However, in order to solve the integral, it is necessary to specify the PDF. The following derivation is made under the assumption that the probability density function $PDF(X,Y)$ is Gaussian, which is a very good approximation in general. The Gaussian distribution has an elliptical cross section (major axis P_{X}, minor axis P_Y) and is rotated by the angle α:

$$PDF(X,Y) = \frac{8}{\pi \cdot P_{\mathrm{X}} \cdot P_{\mathrm{Y}}} \cdot \exp\left[-\left(\frac{\cos\alpha\cdot(X-\Delta X)-\sin\alpha\cdot(Y-\Delta Y)}{P_{\mathrm{X}}}\right)^2 \cdot 8 - \left(\frac{\sin\alpha\cdot(X-\Delta X)+\cos\alpha\cdot(Y-\Delta Y)}{P_{\mathrm{Y}}}\right)^2 \cdot 8\right] \tag{3.8}$$

The factor in front of the exponential term in Eq. (3.8) ensures that the integral of the PDF over all velocities is always equal one. The shape of the probability density function can generally change for each point of the image plane, hence P_X, P_Y, and α are functions of the position vector (X,Y). The image plane parameters P_X and P_Y are derived from the equivalent quantities in the measurement plane as follows:

$$(P_\mathrm{X},P_\mathrm{Y}) = (p_\mathrm{x},p_\mathrm{y}) \cdot \Delta t \cdot M/S. \tag{3.9}$$

Solving Eq. (3.7) for the defined particle images (Eq. (3.5)) and the specified PDF from Eq. (3.8) gives an analytical expression for the correlation function:

$$\begin{aligned} &C(\xi,\psi,X,Y) \sim \\ &\exp\left[-\left(\tfrac{\cos\varphi\cdot(\xi-\Delta X)-\sin\varphi\cdot(\psi-\Delta Y)}{C_\mathrm{X}}\right)^2\cdot 8-\left(\tfrac{\sin\varphi\cdot(\xi-\Delta X)+\cos\varphi\cdot(\psi-\Delta Y)}{C_\mathrm{Y}}\right)^2\cdot 8\right] \end{aligned} \tag{3.10}$$

The parameters C_X, C_Y, and φ in Eq. (3.10) are functions of the position vector (X,Y). For a Gaussian PDF the correlation function is also Gaussian. The elliptical cross section is enlarged due to the correlation procedure, but it has the same orientation as the PDF for the case without velocity gradients:

$$\varphi = \alpha. \tag{3.11}$$

C_X and C_Y depend on the parameters P_X, P_Y of the PDF as follows:

$$C_\mathrm{X} = \sqrt{P_\mathrm{X}^2 + 2\cdot D^2} \tag{3.12a}$$

$$C_\mathrm{Y} = \sqrt{P_\mathrm{Y}^2 + 2\cdot D^2} \tag{3.12b}$$

Where D is the digital particle image diameter. Equations (3.10) - (3.12b) are only exact solutions for the case without velocity gradients. The velocity is assumed to be constant in the surroundings of the point of interest. The effect of gradients will be discussed in Sec. (3.2.5).

Now that the PDF is estimated from the correlation peak, the Reynolds stresses can be calculated from Eqs. (3.2a), (3.2b), and (3.2c) using Eq. (3.8) and (3.9):

$$\left\langle u'^2 \right\rangle = \frac{1}{16}\cdot\left(\cos^2\!\alpha\cdot p_\mathrm{x}^2 + \sin^2\!\alpha\cdot p_\mathrm{y}^2\right) \tag{3.13a}$$

$$\left\langle v'^2 \right\rangle = \frac{1}{16}\cdot\left(\sin^2\!\alpha\cdot p_\mathrm{x}^2 + \cos^2\!\alpha\cdot p_\mathrm{y}^2\right) \tag{3.13b}$$

$$\langle u'\cdot v'\rangle = \langle v'\cdot u'\rangle = \frac{1}{16}\cdot\cos\alpha\cdot\sin\alpha\left(p_\mathrm{y}^2 - p_\mathrm{x}^2\right) \tag{3.13c}$$

In the case of isotropic stresses, the minor and major axes are equal ($p_\mathrm{x} = p_\mathrm{y}$) and the

shear stress vanishes along with the dependence on the angle α of all stresses.

The Reynolds stresses on the image plane are directly related to the stresses on the measurement plane via the time Δt, the magnification M, and the pixel-grid spacing S:

$$\left(\left\langle U'^2\right\rangle, \left\langle V'^2\right\rangle, \langle U' \cdot V'\rangle\right) = \left(\left\langle u'^2\right\rangle, \left\langle v'^2\right\rangle, \langle u' \cdot v'\rangle\right) \cdot \left(\frac{\Delta t \cdot M}{S}\right)^2 \tag{3.14}$$

3.1.3 Effect of velocity gradients

Keane and Adrian (1990) reported an analysis of correlation peaks and their dependency on velocity gradients in conventional PIV. They found that for a shear layer the amplitude decreases with increasing velocity gradients and that the diameter is broadened (by the same factor) in the direction of shear. This section investigates the shape of the correlation peak computed with single-pixel ensemble-correlation in a similar manner.

In order to analyze the influence of the velocity gradient on the shape of the correlation function, it is essential to find an expression for the velocity in the area surrounding the point of interest. Since in many cases the mean flow has a preferred orientation and strong gradients occur only in the perpendicular direction, it seems to be a good approach to develop the velocity in a Taylor series and neglect all higher terms except the first derivative of u with respect to y. For the shift vector on the image plane, this procedure results in the following expression:

$$\vec{\Delta X}(X_0,Y_0) \approx \begin{pmatrix} \Delta X(X_0,Y_0) + Y \cdot \frac{\partial \Delta X(X,Y)}{\partial Y}\Big|_{(X_0,Y_0)} \\ \Delta Y(X_0,Y_0) \end{pmatrix} \tag{3.15}$$

Where (X_0,Y_0) is the point of interest on the image plane for which the correlation function has to be computed.

Taking this velocity gradient into account leads to a rather complex solution of Eq. (3.7):

$$
\begin{aligned}
&C(\xi,\psi,X,Y) \sim \\
&\quad \exp\{ \\
&\qquad \Big[-32\cdot\left(P_\mathrm{X}^2+P_\mathrm{Y}^2\right)\cdot\Big\{\left(1+\Delta X_\mathrm{Y}^2\right)\cdot\Delta Y^2+2\cdot\Delta X\cdot(\Delta X_\mathrm{Y}\cdot\Delta Y-\xi) \\
&\qquad -2\cdot\Delta Y\cdot(\psi+\Delta X_\mathrm{Y}\cdot\xi)+\psi^2+\xi^2+\Delta X^2\Big\}+2\cdot D^2\cdot\Big\{2\cdot\xi^2+2\cdot\Delta X^2 \\
&\qquad +\left(2+\Delta X_\mathrm{Y}^2\right)\cdot\psi^2+\left(2+\Delta X_\mathrm{Y}^2\right)\cdot\Delta Y^2+2\cdot\Delta X\cdot[\Delta X_\mathrm{Y}\cdot(\psi+\Delta Y)-2\cdot\xi] \\
&\qquad -2\cdot\Delta Y\cdot(2\cdot\psi+\Delta X_\mathrm{Y}\cdot\xi)-2\cdot\Delta X_\mathrm{Y}\cdot\xi\cdot\psi\}+(P_\mathrm{X}-P_\mathrm{Y})\cdot(P_\mathrm{X}+P_\mathrm{Y})\cdot \\
&\qquad \{[\psi-\xi+(\Delta X_\mathrm{Y}-1)\cdot\Delta Y+\Delta X]\cdot[\xi+\psi-(\Delta X_\mathrm{Y}+1)\cdot\Delta Y-\Delta X]\cdot \\
&\qquad \cos(2\cdot\alpha)+2\cdot(\Delta X_\mathrm{Y}\cdot\Delta Y+\Delta X-\xi)\cdot(\Delta Y-\psi)\cdot\sin(2\cdot\alpha)\}] \\
&\qquad / \\
&\qquad \Big\{2\cdot D^2\cdot\Big[D^2\cdot\left(16+\Delta X_\mathrm{Y}^2\right)+\left(P_\mathrm{X}^2+P_\mathrm{Y}^2\right)\cdot\left(4+\Delta \mathrm{X}_Y^2\right)\Big] \\
&\qquad +6\cdot D^4\cdot\Delta X_\mathrm{Y}^2+8\cdot P_\mathrm{X}^2\cdot P_\mathrm{Y}^2+2\cdot D^2\cdot\left(P_\mathrm{X}^2+P_\mathrm{Y}^2\right)\cdot\left(4+\Delta X_\mathrm{Y}^2\right) \\
&\qquad -4\cdot D^2\cdot(P_\mathrm{X}-P_\mathrm{Y})\cdot(P_\mathrm{X}+P_\mathrm{Y})\cdot\Delta X_\mathrm{Y}\cdot(\Delta X_\mathrm{Y}\cdot\mathrm{Cos}(2\cdot\alpha)-2\cdot\sin(2\cdot\alpha))\Big\} \\
&\qquad \}
\end{aligned}
\tag{3.16}
$$

The term ΔX_Y in Eq. (3.16) identifies the velocity gradient (or more precisely the shift-vector gradient) $\partial\Delta X/\partial Y$. P_X, P_Y, and α are the parameters of the probability density function on the image plane from Eq. (3.8).

Again, Eq. (3.16) is Gaussian with an elliptical cross section. However, the minor and major axis and the angle of rotation can not be extracted from the equation as easily as before.

Figure 3.1 shows the correlation function from Eq. (3.16) for different conditions. The PDF was non-isotropic ($P_\mathrm{X} = 5\,\mathrm{px}$, $P_\mathrm{Y} = 1\,\mathrm{px}$) in all cases and the angle of orientation was $\alpha = 20°$. A particle image diameter D of 1 px, 3 px, and 5 px was used for the left, middle, and right column, respectively.

No gradient $\partial\Delta X/\partial Y$ was applied for the middle row. Here, the resulting correlation peaks look similar to the applied PDF (cross section shown as red solid line) and Eqs. (3.12a) and (3.12b) are sufficient to determine the parameters of the PDF.

The upper and lower rows in Fig. 3.1 show the influence of an additional velocity gradient $\partial\Delta X/\partial Y$. Here, the correlation functions are stretched in the direction of P_X according to the analysis of Keane and Adrian (1990) but, in addition, they are compressed in the direction of P_Y and rotated around the center due to the velocity gradient. The rotation direction depends on the sign of the velocity gradient.

Consequently, it is important to note that the shape of the PDF is not directly related to the shape of the correlation function in the case of strong velocity gradients. Therefore,

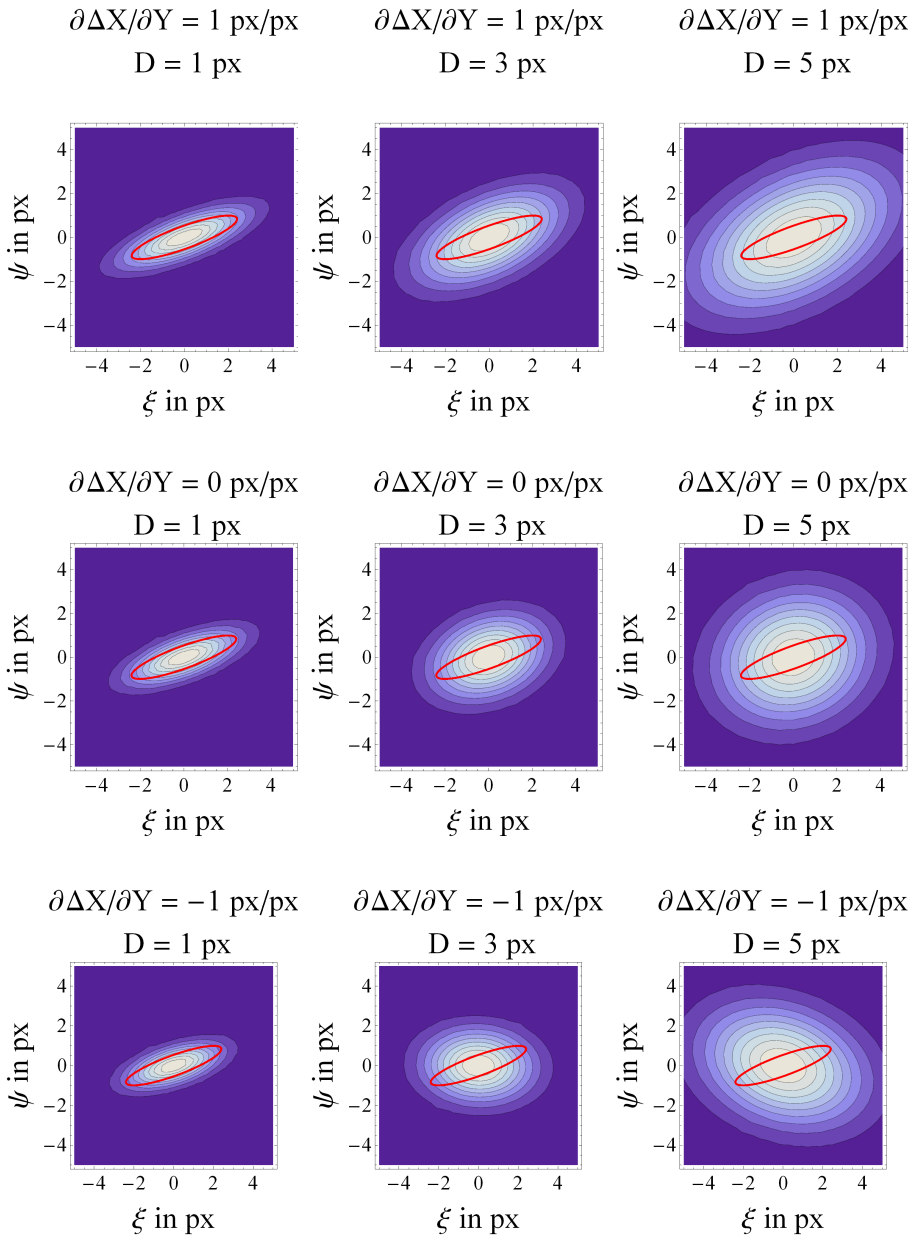

Figure 3.1: Contour plot of the analytical correlation function for different velocity gradients $\partial\Delta X/\partial Y$ ([1,0,−1] px/px from top to bottom) and different particle image diameters D ([1,3,5] px, from left to right). The size and orientation of the probability density function is indicated by the solid red line, the corresponding parameters P_X, P_Y, and α are 5 px, 1 px, and 20°, respectively.

it is essential to include the information about the surrounding velocity field in order to compute the Reynolds stresses for a given point.

Using Eqs. (3.12a) and (3.12b) for the reconstruction of the PDF and the estimation of the Reynolds stresses leads to a systematic error in the presence of velocity gradients. As a result of this, the normal stress in the $X-$direction is overestimated and the Reynolds shear stress is under- or over- estimated, depending on the orientation of the PDF and the sign of the velocity gradient.

Additionally, Fig. 3.1 shows that the influence of velocity gradients on the shape of the correlation function is strongly dependent on the size of the particle images. The deformation gets stronger with increasing digital particle image diameter D. The compensation of the velocity gradient effects will be discussed in Sec. 3.2.5.

The broadening of the correlation peaks under the influence of strong velocity gradients is in qualitative agreement with the considerations for conventional PIV made by Keane and Adrian (1990) and Kähler et al (2006).

3.2 Analysis of synthetic PIV images

In order to determine the accuracy of the method presented above, synthetic PIV images with different probability density functions were generated and the estimated Reynolds stresses were compared to the simulated values. This allows for a quantitative accuracy assessment.

The calculation procedure is described in Sec. 3.2.1. Section 3.2.2 deals with isotropic stresses and investigates the effect of several parameters on the accuracy of the estimated turbulence. Section 3.2.3 focuses on the more general case of homogeneous non-isotropic Reynolds stresses. The ability to estimate shear stresses as well as the demonstration of the presented method's spatial resolution are analyzed in Sec. 3.2.4 and 3.2.4, respectively. The last section studies velocity gradient effects and their compensation (Sec. 3.2.5).

3.2.1 Calculation procedure

All synthetic PIV images were generated as discussed in Sec. 2.3.3. Unless otherwise stated, each single test case consists of 20,000 PIV image pairs. A maximum of 20,000 counts was applied for the intensity of the particle images and a SNR of 100 was simulated. Each pixel´s gray value is computed from the integral of the intensity over the corresponding area, with respect to the finite pixel-grid spacing of the camera sensor by using Eq. (2.7). This procedure causes a difference between the applied particle image diameter $D_{\text{simulated}}$ and the resulting diameter computed with a Gaussian fit-function $D_{\text{estimated}}$.

The fraction of illuminated pixels was kept constant at 10% for all generated images, meaning that 10% of all pixels had an intensity of more than 20,000 counts/e^2 $\approx$ 2,700

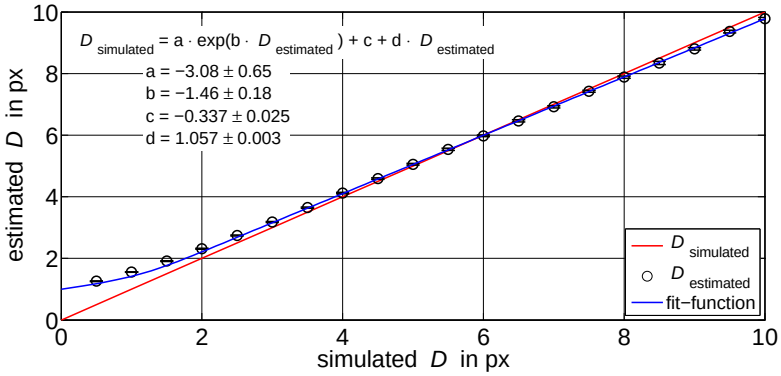

Figure 3.2: Estimation of the digital particle image diameter D for each 20,000 synthetic PIV image pairs. The graph shows the mean value over 20×20 px and the corresponding standard deviation as error-bar.

counts. Hence, the number of particle images changes with the particle image diameter according to Eq. (2.8). The average number of particle images in a 20×20 px region is, for example, 5.6 for a digital particle image diameter of $D = 3$ px.

For each particle in each first PIV image, the position is randomly chosen. The position in the second image changed with respect to the first one due to the velocity and its fluctuations. The vertical component of the velocity was zero, while a constant gradient was used for the horizontal component ($\partial \Delta X / \partial Y = 0.05$). The velocity fluctuations were random numbers with a Gaussian distribution. However, the amplitude of the fluctuations was controlled by the parameters P_X, P_Y, and α of the PDF. The theoretical Reynolds stresses were computed from the applied fluctuations.

Upon the generation of the synthetic PIV images, the correlation function for each pixel is computed using Eq. (2.1). In order to determine the digital particle image diameter D the auto-correlation function is also required (Kähler et al, 2006). The latter can be computed by using Eq. (2.1) and simply exchanging image B with image A. For better accuracy, D is also estimated from the auto-correlation of the B images. In theory, the auto-correlation of a Gaussian is also a Gaussian, but the width is increased by a factor of $\sqrt{2}$ (Raffel et al, 2007). Hence, fitting the auto-correlation peak gives an estimation of the particle image diameter. For experimental PIV recordings, it was found that the particle images can be stretched in case of supersonic or hypersonic flow. Hence, the auto-correlation peaks should be compared to a Gaussian with elliptical cross section.

Figure 3.2 shows the comparison between the input value and the estimated diameter. The proportionality only holds for particle images bigger than ≈ 3 px, whereas for smaller values the particle image size is estimated to be too large. The deviation can be corrected using the fit-function in Fig. 3.2.

A Gaussian fit-function with the same structure as Eq. (3.10) was applied to the correlation peaks in the next step. With this, the parameters C_X, C_Y, and φ of each correlation

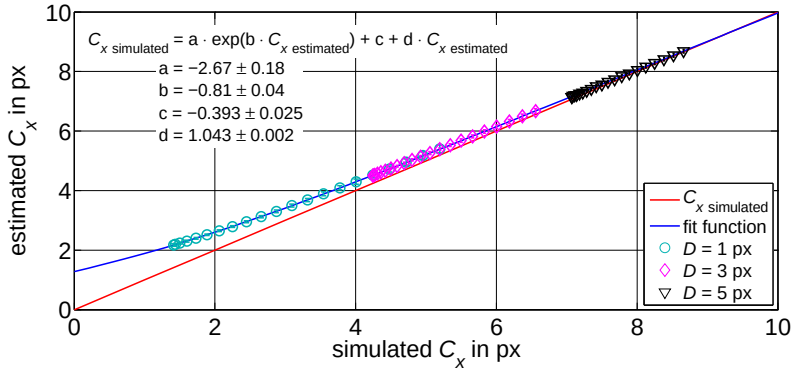

Figure 3.3: Estimation of the correlation peak diameter C_X for each 20,000 synthetic PIV image pairs. The graph shows the mean value over 20×20 px and the corresponding standard deviation as error-bar.

function were determined. The estimation of the correlation peak's diameter is also subject to a systematic error, as shown in Fig. 3.3 for the major axis C_X.

Both, particle image diameter and correlation peak diameter were corrected by using the fit-function shown in Fig. 3.2 and Fig. 3.3, respectively.

The parameters P_X and P_Y of the PDF were computed by using Eqs. (3.12a) and (3.12b) and finally the Reynolds stresses were determined from Eqs. (3.13a), (3.13b), and (3.13c).

3.2.2 Isotropic stresses

In this section, PIV images with isotropic stress distribution are evaluated. Isotropic stress means that the parameters P_X and P_Y are equal and Eq. (3.8) becomes:

$$PDF(X,Y,P_X = P_Y) = \frac{8}{\pi \cdot P_X^2} \exp\left[-\frac{(X-\Delta X)^2+(Y-\Delta Y)^2}{P_X^2} \cdot 8\right] \tag{3.17}$$

In this case the parameters C_X and C_Y of the fit-function (Eq. (3.10)) should also be equal. Thus, a symmetrical fit-function can be applied.

A turbulent flow with isotropic stresses has a rotationally symmetrical PDF and is thus free of shear stresses. In a laminar flow the Brownian motion of the tracer particles causes a broadening of the correlation peak. This can be treated as isotropic stresses to determine the temperature within the flow in a non-intrusive way. This was demonstrated by Hohreiter et al (2002) and Chamarthy et al (2009) for correlation functions computed from interrogation windows with averaged window-correlation PIV evaluation.

First, the influence of the particle image size on the accuracy of the determination of the correlation-peak's size and position was investigated. Figure 3.4a shows the RMS-uncertainty of the estimated correlation peak diameter C_X with respect to the particle

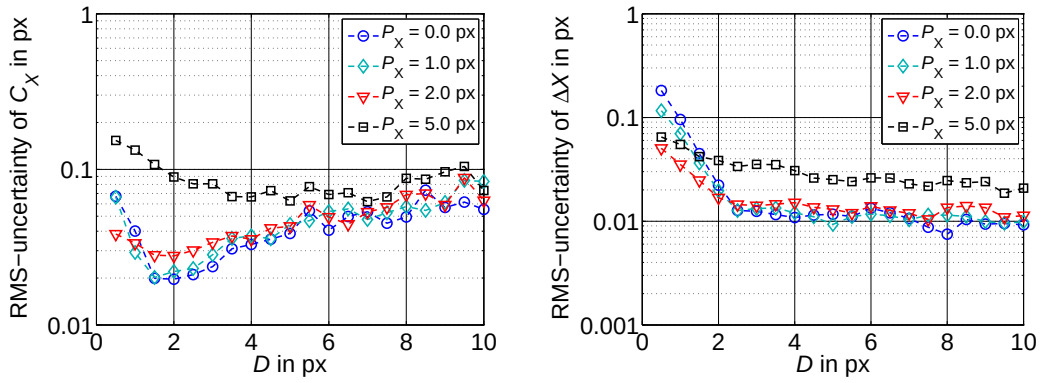

(a) (b)

Figure 3.4: Influence of the digital particle image diameter D on the accuracy of the estimated size of the correlation peak C_X (a) and the computed shift vector component ΔX (b).

image diameter D for four different values of P_X. Each point in Figs. 3.4a - 3.5 represents the standard deviation of 20×20 correlation peaks computed from 20,000 synthetic PIV image pairs using Eq. (2.1). For the generation of the synthetic PIV images the applied probability density function was constant for all pixel in the image plane.

All four curves in Fig. 3.4a show a local minimum for a certain particle image diameter, depending in the amplitude of the velocity fluctuations. The parameter P_X, in real measurements, not only depends on the turbulence in the flow but also on the time Δt between the acquisition of the two PIV images, the magnification M, and the pixel-grid spacing S and can thus be partially controlled by these parameters.

As an example, the investigation of the wake flow of a blunt axis-symmetric space launcher model in Bitter et al (2011) resulted in velocity fluctuations with a maximum of $P_\mathrm{X} = 4.5\,\mathrm{px}$ in the shear layer of the wake at $\mathrm{Ma} = 0.7$, while the maximum value in the turbulent boundary layer was around $P_\mathrm{X} = 1.5\,\mathrm{px}$.

Fig. 3.4a shows a minimum error for a digital particle image diameter of $D \approx 1.8\,\mathrm{px}$ without velocity fluctuations. This minimum shifts to larger values of D for increasing fluctuations. Additionally, the minimum RMS-uncertainty increases. The fact that the random error increases consistently for larger particle images can mainly be explained by the decreasing number of particle images (the fraction of illuminated pixels was kept constant at 10%).

The maximum position of the correlation peak represents the mean velocity and is estimated by using a three-point Gauss-fit. The accuracy of the estimated velocity is shown in Fig. 3.4b. Particle images smaller than $D \approx 1\,\mathrm{px}$ are not suitable for accurate velocity measurements, they cause so called “peak locking”. This is mostly visible by using a histogram plot as displayed first in Kähler (1997). For particle images larger than

$D \approx 2$ px the RMS-uncertainty remains nearly constant, and even drops slightly. This differs from the results presented by Raffel et al (2007) for single-pass window-correlation, where a global minimum error for $D \approx 1.8$ px was found. Overall, the minimum error of about 0.01 px is comparable to that obtained by using window-correlation based PIV methods.

The optimum particle image diameter seems to be around $D = 3\,\text{px}$. At this size the uncertainty for the estimation of correlation-peak diameter and its maximum position (or mean velocity) are fairly low and the particle image size can be well estimated.

The parameter P_X of the PDF can be determined from the correlation-peak size and the particle image diameter by using Eq. (3.12a) and the normal stresses are computed from Eqs. (3.13a) and (3.13b). Based on the two measured velocity components the turbulence level Tu is used to evaluate the computed stresses. It is defined as follows:

$$Tu = \sqrt{\frac{\langle U'^2 \rangle + \langle V'^2 \rangle}{2}} \tag{3.18}$$

Furthermore, with Eq. (3.13a) and (3.13b) this can be reduced to

$$Tu = \frac{P_\text{X}}{4} \tag{3.19}$$

in the case of isotropic stresses.

Figure 3.5 shows the estimated turbulence level with respect to the simulated turbulence level for three different particle image diameters. For small fluctuations the correlation and auto-correlation peaks have almost the same diameter. Since the PDF's diameter is computed from their difference (Eq. (3.12a) and (3.12b)), its error grows considerably in this case. However, for the precise determination of small Reynolds stresses, the time Δt between the two PIV images, and thus the correlation peak size, can be increased. For a turbulence level larger than $Tu > 0.2\,\text{px}$, the systematic error becomes negligible. For the real example of the round jet in Sec. 3.3 the turbulence level was between $Tu = 0.1\,\text{px}$ (undisturbed flow) and $Tu = 1.5\,\text{px}$ (in the shear layer). For the wake flow in Chapter 5 it was between $Tu = 0.25\,\text{px}$ (in the boundary layer) and $Tu = 1.3\,\text{px}$ (in the shear layer).

The accuracy of the estimated turbulence level is not only dependent on the digital particle image diameter and the turbulence level itself, but also on the number of image pairs. Figs. 3.6a and 3.6b illustrate how the number of PIV image pairs N affects the estimated turbulence and mean velocity, respectively. The fraction of illuminated pixels was still 10%. As expected, the error decreases with an increasing number of images. For the tested cases, 10,000 image pairs appear to be a sufficient number.

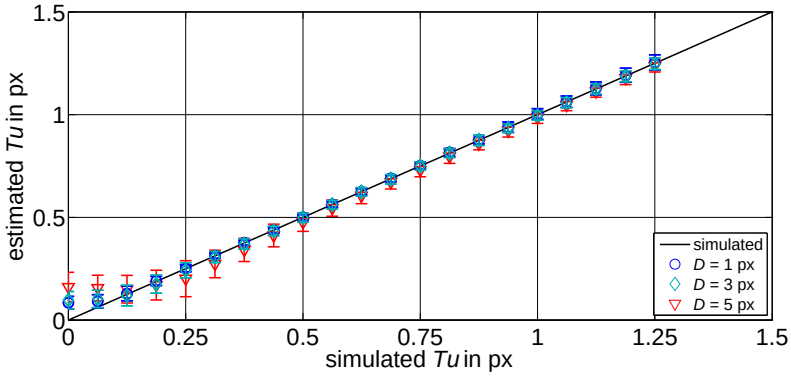

Figure 3.5: Systematic error of the estimated turbulence level Tu depending on the applied turbulence.

3.2.3 Homogeneous flow with non-isotropic stresses

So far, only synthetic PIV images with symmetric probability density functions were analyzed. In the following, the more general approach from Eq. (3.8) will be applied. Thus, the normal stresses $\langle U'^2 \rangle$ and $\langle V'^2 \rangle$ are not necessarily equal and the shear stress $\langle U' \cdot V' \rangle$ can differ from zero. However, the simulated stresses are still constant over the whole image plane. Figure 3.6c shows the RMS-uncertainty for the estimated Reynolds shear stress with respect to the number of image pairs N. The parameters P_X, P_Y of the PDF were fixed at 2 px and 0.5 px, respectively; while four different angles α were tested. The RMS-uncertainty decreases exponentially over N.

Figures 3.7a and 3.7b show the comparison between the applied and the estimated Reynolds stresses for different shapes of the PDF. In Fig. 3.7a the PDF's cross section has a constant size but is rotated by the angle α. The stresses for a constant angle of rotation and increasing ratio of $P_\mathrm{Y}/P_\mathrm{X}$ are shown in Fig. 3.7b. Each point was computed from 20,000 PIV image pairs with constant stress. 20×20 correlation peaks were analyzed. The digital particle image diameter was $D = 3$ px. The error-bars correspond to the standard deviation of the stresses for each 400 correlation peaks.

Overall, the estimated mean values for the stresses are in good agreement with the simulated ones. The maximum RMS-error is 0.03 px^2. Further tests with different probability density functions showed similar results.

According to the previous analysis, the developed method is suitable for estimating Reynolds stresses, in particular shear stresses. Although the stresses are computed for each single-pixel, only mean values over 400 px are plotted above. However, results for each single pixel are presented in the next two sections.

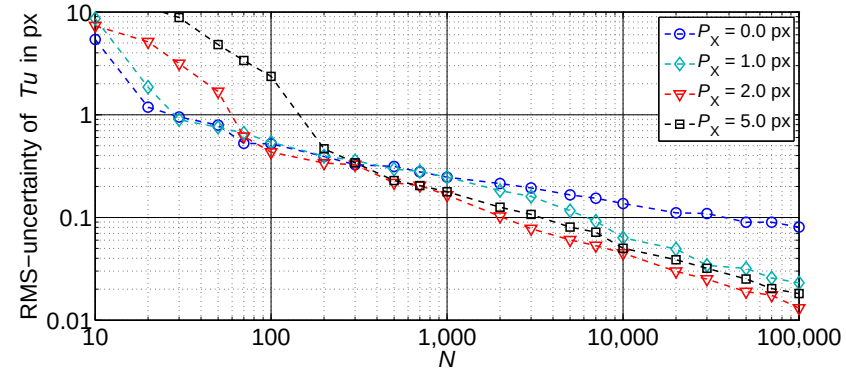

(a)

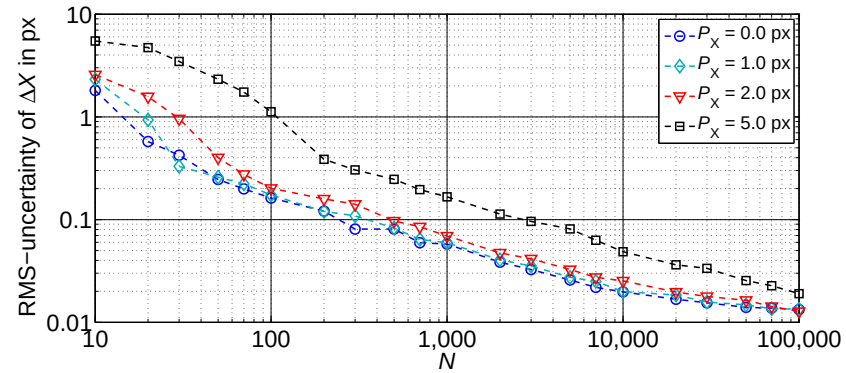

(b)

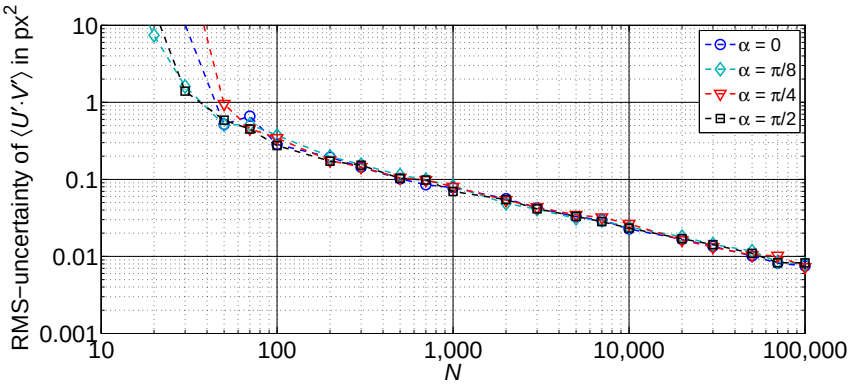

(c)

Figure 3.6: Influence of the number of synthetic PIV images on the accuracy of the estimated turbulence level Tu (a), mean shift vector (b), and the Reynolds shear stress (c). The particle image diameter was $D = 3\,\mathrm{px}$.

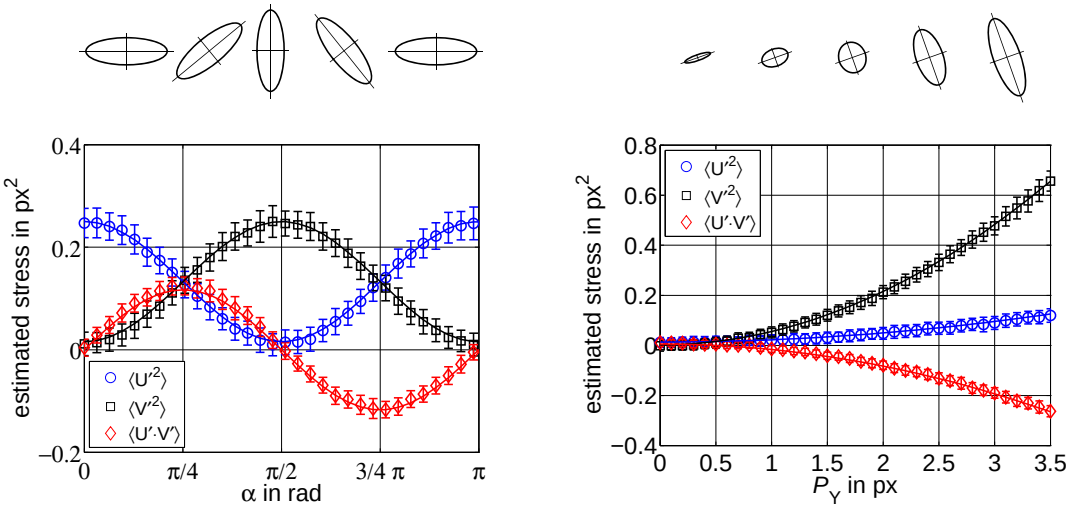

(a) (b)

Figure 3.7: Estimated Reynolds stresses for 20,000 PIV images (20 px × 20 px). For (a) the probability density function had a fixed axis ratio ($P_X = 2.0$ px, $P_Y = 0.5$ px) and a varying angle of rotation ($\alpha = 0 \ldots \pi$). In Case of (b) the PDF had a fixed angle of rotation ($\alpha = \pi/8$) and a fixed major axis ($P_X = 0.5$ px), the minor axis P_Y varied from 0 px to 2 px. A cross section through the correlation function is sketched in the top part.

3.2.4 Shear flow with non-isotropic stresses

This section demonstrates the enhanced spatial resolution for an example of non-homogeneous Reynolds stresses. Therefore, 100,000 synthetic PIV image pairs, $256 \times 256\,\mathrm{px}$ in size, were generated with a $Siemens - star$ shaped stress distribution. The mean velocity was kept constant about the whole image area. A digital particle image diameter of $D = 3\,\mathrm{px}$ was applied and the fraction of illuminated area was set to 2.5%. Hence, on average 0.9 particle images are within a $16 \times 16\,\mathrm{px}$ window. This corresponds to a relatively low seeding density.

The velocity fluctuations were totally uncorrelated, meaning that even two closely spaced particle images can move in different directions. This simulates small scale turbulent structures. The following parameters P_X, P_Y, and α of the PDF were applied:

$$P_\mathrm{X} = 0.5\,\mathrm{px} + 3\,\mathrm{px} \cdot \exp\left[-8 \cdot \left(\frac{X - 128\,\mathrm{px}}{|Y - 128\,\mathrm{px}| \cdot 1.25}\right)^2\right] \tag{3.20}$$
$$+1\,\mathrm{px} \cdot \exp\left[-8 \cdot \left(\frac{Y - 128\,\mathrm{px}}{|X - 128\,\mathrm{px}| \cdot 0.75}\right)^2\right]$$

$$P_\mathrm{Y} \;=\; 0.5\,\mathrm{px} \tag{3.21}$$

$$\alpha \;=\; \mathrm{sign}\,(Y - 128\,\mathrm{px}) \cdot \arctan\left[\frac{(X - 128\,\mathrm{px}) \cdot 2\pi}{|Y - 128\,\mathrm{px}| \cdot 1.25)} + \frac{\pi}{2}\right] \tag{3.22}$$

Figure 3.8 shows the computed results for the turbulence level Tu as defined in Eq. (3.18) and the Reynolds shear stress $\langle U' \cdot V' \rangle$ in the left and right column, respectively. The simulated values are plotted in the upper row, while the estimations using single-pixel ensemble-correlation and window-correlation are shown in the middle and lower row, respectively.

Although the single-pixel results for the turbulence level and shear stress in Fig. 3.8c are somewhat noisy, it is clearly shown that small scale flow phenomena can be resolved. The estimated values are consistent with the simulated ones in the single-pixel approach case.

On the other hand, the values computed with window-correlation approach (Fig. 3.8b) do not show such good spatial resolution and are not able to resolve small scale structures. Additionally, the stresses computed with the window-correlation method are significantly smaller than the simulated values. This is due to the fact that the information is averaged over the window size.

Figures 3.9a and 3.9b illustrate how the correlation window size influences the magnitude of the estimated stresses. For the window size of $32 \times 32\,\mathrm{px}$ and $16 \times 16\,\mathrm{px}$ the absolute values are always too small and for $8 \times 8\,\mathrm{px}$ windows, the number of spurious vectors

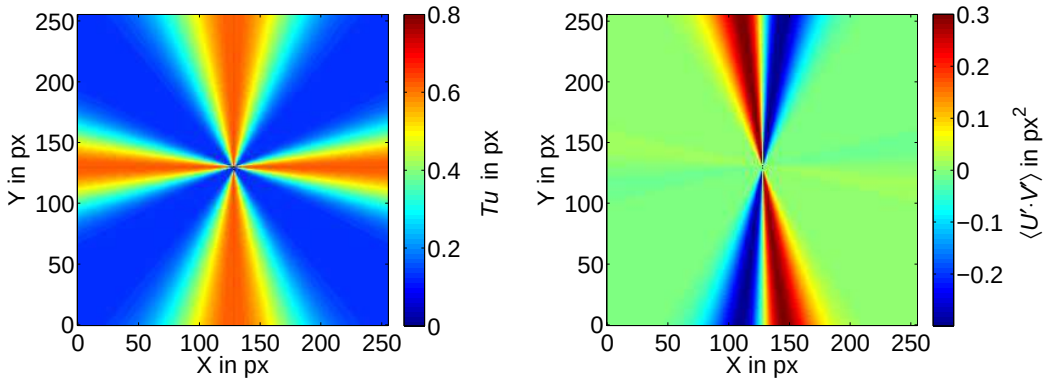

(a) simulated

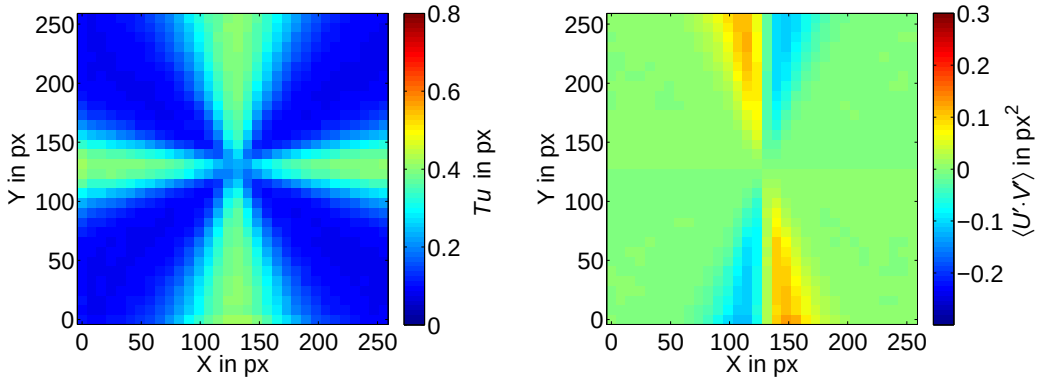

(b) window-correlation 16×16 px

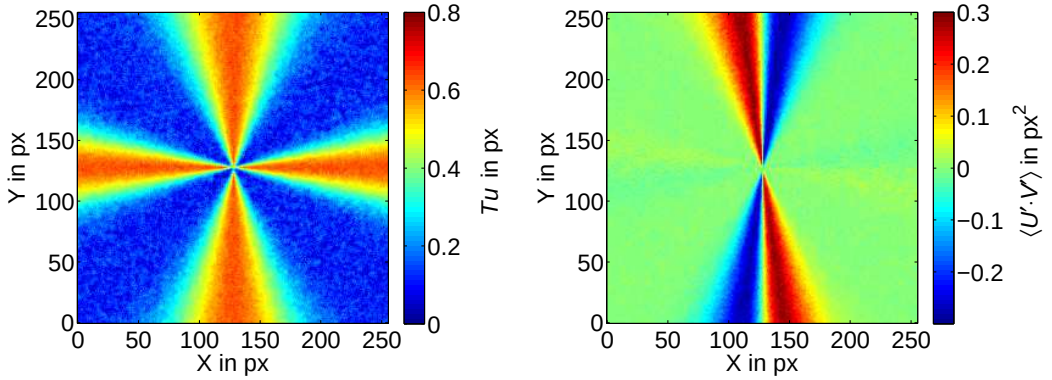

(c) single-pixel ensemble-correlation

Figure 3.8: Turbulence level (left) and Reynolds shear stress (right) for a synthetic test case of 100,000 PIV recordings. Simulated values (a) and computed results using standard window-correlation techniques (b) and the single-pixel approach (c).

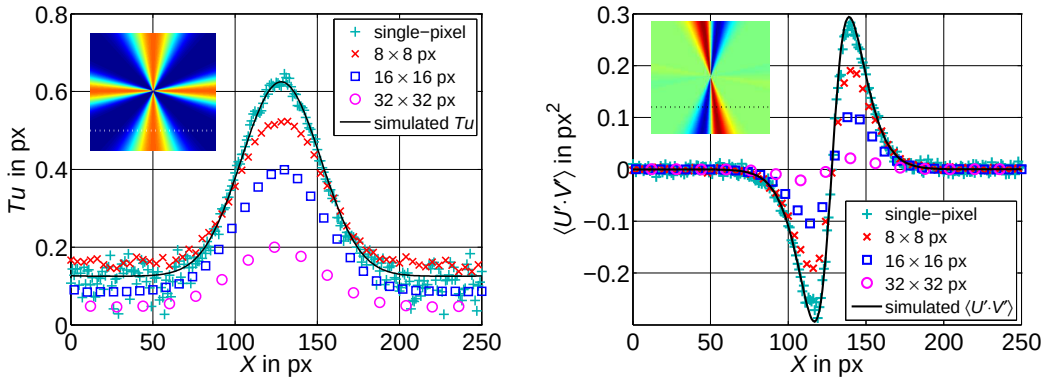

(a) (b)

Figure 3.9: Turbulence (a) and Reynolds shear stress (b) level for a cross section at $y = 50\,\text{px}$ of the data set from Fig. 3.8. The black solid line indicates the simulated level.

increases significantly, which introduces artificial stresses. The maximum deviation between simulated turbulence level and estimation using ensemble-correlation is only 0.10 px for the cross section at $y = 50\,\text{px}$, as shown in Fig. 3.9a, whereas it is 0.32 px in the case of $16 \times 16\,\text{px}$ window-correlation. For the Reynolds shear stress, the maximum deviations in Fig. 3.9b are 0.03 px and 0.25 px for the ensemble correlation and the $16 \times 16\,\text{px}$ window-correlation, respectively.

The evaluated synthetic test case shows that window-correlation based PIV evaluation cannot resolve small turbulent structures; only turbulent structures larger than the interrogation-window size contribute to the estimated stresses.

However, the ensemble-correlation based method is, in principle, capable to detect any small turbulent structures. It does not average velocity fluctuations over a certain area, not even over the single-pixel, and all fluctuations are stored within the correlation peak. Also, turbulent structures smaller than one pixel contribute to the broadening of the correlation peak even though the computed stresses correspond to the mean values over the area of one pixel.

3.2.5 Compensation of velocity-gradient effects

In paragraph 3.1.3 (Fig. 3.1) the deformation of the correlation peak due to a gradient in the velocity field was demonstrated. This effect is quantitatively analyzed in this section, for which PIV images with homogeneous stresses were generated. The parameters P_X, P_Y, and α of the PDF were chosen to be 2 px, 0.5 px, and 0°, respectively. The velocity gradient $\partial\Delta X/\partial Y$ varied from -1 to $+1\,\text{px/px}$.

Figures 3.10a, 3.10b, and 3.10c show the computed normal stresses and shear stresses. Three different particle image diameters were tested. The figures show a strong bias error that depends on the particle image size and the velocity gradient. Only the normal stress in the $Y-$direction is not affected by the velocity gradient.

The strong bias error is caused by the deformation of the correlation peaks in the case of velocity gradients. Figure 3.11 shows the correlation peaks for the first, last, and middle points of the data set from Figs. 3.10a, 3.10b, and 3.10c for $D = 5\,\mathrm{px}$. These peaks are computed by using Eq. (2.1) and are in qualitative agreement with the analytical functions in Fig. 3.1. The correlation peaks are stretched in the direction of the flow and compressed perpendicular to it. Additionally, a positive velocity gradient $\partial\Delta X/\partial Y$ rotates the correlation peak in the counter clockwise direction and vice versa.

Figures 3.10a, 3.10c, and 3.11 clearly show that the simple relations from 3.12a and 3.12b are not sufficient if strong velocity gradients are present.

A detailed inspection of Eq. (3.16) allows for a correction of the Reynolds stresses with respect to the velocity gradient $\partial\Delta X/\partial Y$:

$$\left\langle U'^2 \right\rangle_{\mathrm{corrected}} = \left\langle U'^2 \right\rangle_{\mathrm{gradient}} - \frac{D^2}{16} \cdot \left(\frac{\partial \Delta X}{\partial Y} \right)^2 \tag{3.23}$$

$$\left\langle V'^2 \right\rangle_{\mathrm{corrected}} = \left\langle V'^2 \right\rangle_{\mathrm{gradient}} - \frac{D^2}{16} \cdot \left(\frac{\partial \Delta Y}{\partial X} \right)^2 \tag{3.24}$$

$$\left\langle U' \cdot V' \right\rangle_{\mathrm{corrected}} = \left\langle U' \cdot V' \right\rangle - \frac{D^2}{16} \cdot \left(\frac{\partial \Delta X}{\partial Y} + \frac{\partial \Delta Y}{\partial X} \right) \tag{3.25}$$

For the derivation of Eqs. (3.23), (3.24), and (3.25), the analytical correlation peak from Eq. (3.16) was compared to a Gaussian with elliptical cross section like the one used in Eq. (3.10). In this way it was possible to identify the change of the parameters C_{X}, C_{Y}, and α with respect to the velocity gradient $\partial\Delta X/\partial Y$ and hence to correct the Reynolds stresses. Additionally, the influence of the velocity gradient $\partial\Delta Y/\partial X$ was investigated: both gradient effects can be corrected independently.

In order to verify Eqs. (3.23), (3.24), and (3.25), 20,000 synthetic PIV images with a size of $256 \times 256\,\mathrm{px}$ and varying velocity gradients were generated and evaluated. The particle image diameter was $D = 3\,\mathrm{px}$ and the parameters P_{X}, P_{Y}, and α were $2\,\mathrm{px}$, $2\,\mathrm{px}$, and $0°$, respectively. Isotropic Reynolds stresses were applied thus, the shear stress should be zero.

Figure 3.12 shows the distribution of the horizontal velocity, the Reynolds shear stress influenced by the velocity gradient $\langle U' \cdot V' \rangle_{\mathrm{gradient}}$ and the corrected shear stress $\langle U' \cdot V' \rangle_{\mathrm{corrected}}$ computed with Eq. (3.25). In the right column of Fig. 3.12, the projection of the data points on the $Y-$axis is shown together with the simulated values (red solid line). A sinusoidal velocity profile with increasing amplitude from top to bottom was generated (Fig. 3.12a). Thus, the velocity gradient also increases and the Reynolds shear stress seems to rise with it (Fig. 3.12b).

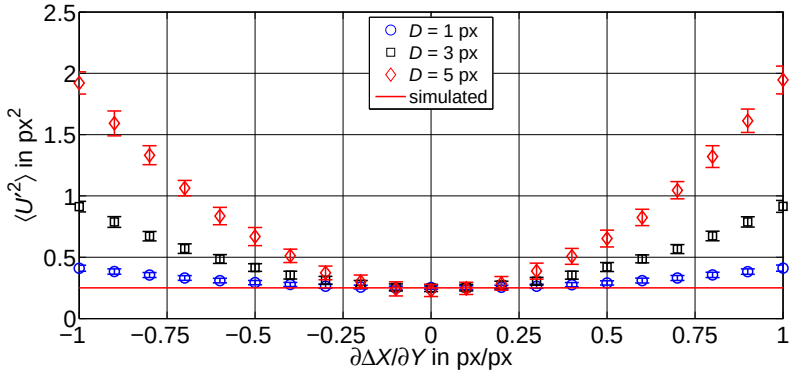

(a)

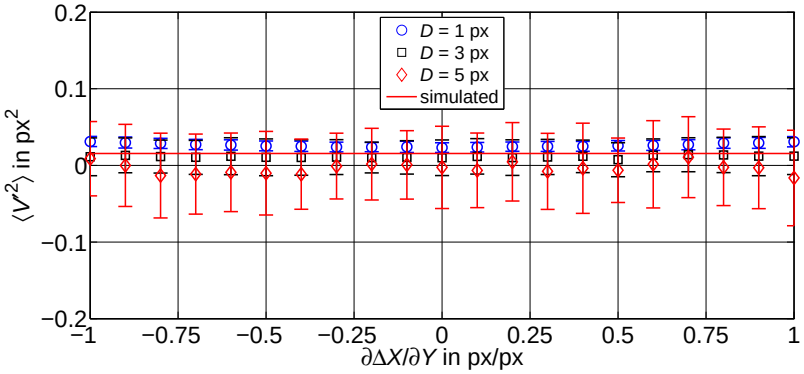

(b)

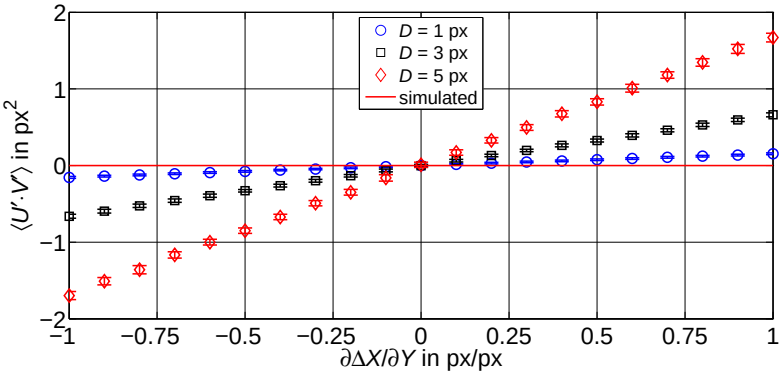

(c)

Figure 3.10: Reynolds normal stress in the $X-$direction (a) and in the $Y-$direction (b) as well as Reynolds shear stress (c) under the influence of the velocity gradient $\partial\Delta X/\partial Y$.

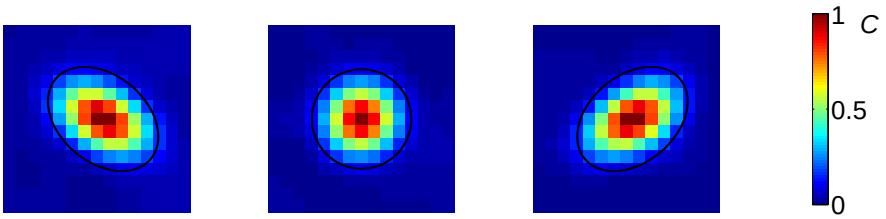

$$\partial\Delta X/\partial Y = [-1,0,1]$$

Figure 3.11: Computed correlation peak for each 20,000 synthetic PIV image pairs with different velocity gradients $\partial\Delta X/\partial Y$. A digital particle image diameter of $D = 5\,\mathrm{px}$ was applied. The parameters P_X, P_Y, and α of the PDF were 2 px, 0.5 px, and 0°, respectively. The solid lines indicate the size and orientation of the fitted Gaussian.

Note, however, that the estimation of the mean velocity is not affected. Thus, it is possible to determine the velocity gradient from the mean velocity field and to correct the Reynolds stresses. A correction, using Eq. (3.25), of the shear stress is shown in Fig. 3.12c. The remaining standard deviation of the corrected shear stress $\langle U' \cdot V' \rangle_\mathrm{corrected}$ is only $0.045\,\mathrm{px}^2$ (for the uncorrected stress it was $0.7\,\mathrm{px}^2$). An other test case with both gradients $\partial\Delta X/\partial Y$ and $\partial\Delta Y/\partial X$ (not presented in this work) confirmed that these can be compensated independently.

In conclusion, it can be stated, that the estimation of the Reynolds stresses is strongly influenced by the velocity gradients $\partial\Delta X/\partial Y$ and $\partial\Delta Y/\partial X$. It was found that the computed values can be categorized between real and artificial stresses. The latter depend on the particle image diameter squared, for all in-plane Reynolds stress components. The analytical results are in good agreement with the computed values from the synthetic PIV recordings.

It should be emphasized again, that only the first derivative of u with respect to y was considered for the derivation of the correlation function (see Eq. (3.15)). However, a higher order expansion might lead to even better results.

3.3 Analysis of real PIV images: water jet flow

So far only synthetic PIV images were analyzed. This section presents computed Reynolds stresses for real PIV recordings using the method discussed in this chapter. Only the shear stresses is presented here, since this is usually of major interest as long as no flow separation is studied in detail. Nevertheless, the normal stresses require almost no additional computing time and can easily be extracted for the complete description.

The experimental example analyzes a round jet flow in water at a Reynolds number of $\mathrm{Re_d} \approx 26{,}000$ based on the nozzle diameter which was $\varnothing d = 2.4\,\mathrm{mm}$. The pipe had an

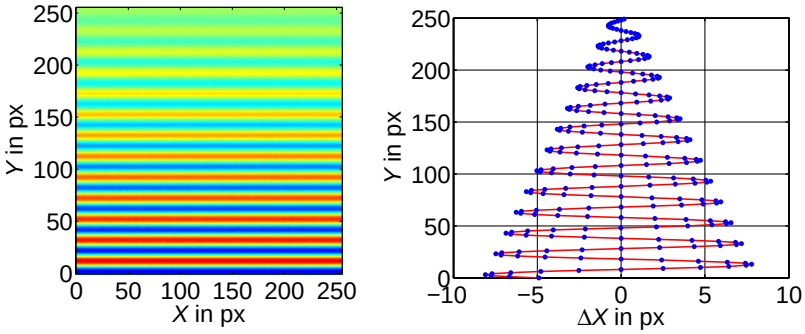

(a) horizontal velocity

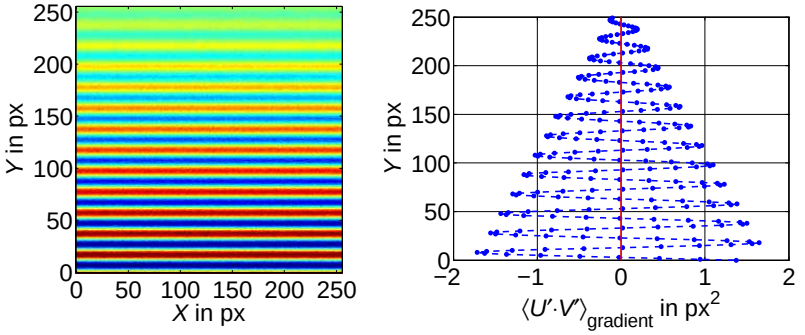

(b) uncorrected Reynolds shear stress

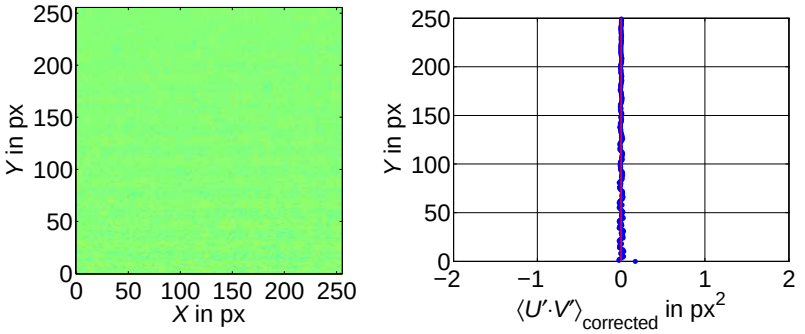

(c) corrected Reynolds shear stress

Figure 3.12: Influence of the velocity gradient $\partial\Delta X/\partial Y$ on the Reynolds shear stress for a synthetic shear flow with varying gradient. 20,000 synthetic PIV images with isotropic stresses were analyzed.

inner diameter of approximately 10 mm and was connected to a diaphragm pump. The setup is illustrated in Fig. (3.13). The near field of the jet was selected, as the resolution of the strong gradient at the outlet of the nozzle is very difficult.

A high repetition rate CMOS camera (*Phantom V12* by Vision Research Inc.) with a Zeiss $Makro - PlanarT * f2/100$ objective lens plus a teleconverter ($Kenko\,2 \times Pro\,300$) were used to observe the jet. The working distance was approximately 0.5 m, which led to an optical magnification of $M = 0.73$ and a scaling factor of 27.5 µm/px. A continuous-wave laser (*Millennia* by Spectra-Physics) with 10 W optical power and a wave length of 532 nm illuminated tracer particles in a light sheet (approximately 300 µm in thickness). Hollow class spheres with a diameter of 10 µm were used as tracer particle (by Dantec Dynamics). 25,000 single exposed PIV image pairs with a size of only 384×256 px were captured at a frequency of 250 Hz, while the time separation between each two images was set to $\Delta t = 20$ µs. The exposure time of the camera was set to 1.8 µs.

The analysis of the PIV recordings revealed that the particle image diameter on the image plane was around $D \approx 1.9$ px and the particle density was such that approximately 1% of the images was illuminated, this corresponds to about 1.3 particle images in an area of 16×16 px. The maximum velocity of the jet was determined to be 9.77 m/s corresponding to a shift vector of 7.1 px.

Figure 3.14 shows a comparison of the Reynolds shear stress distribution directly behind the nozzle, between window-correlation using a standard software (*DaVis* by LaVision GmbH) and the developed single-pixel ensemble-correlation approach.

A multi-pass algorithm with decreasing window size (from 32×32 px to 16×16 px with 50% overlap) and a Gaussian window weighting was applied for the window-correlation method. Thus, a total of 252 independent vectors could be computed for 25,000 vector fields leading to 252 independent data points for the Reynolds shear stress distribution, computed from this ensemble of vector fields (Fig. 3.14a).

On the other hand, for the single-pixel approach, 59,400 correlation peaks were computed

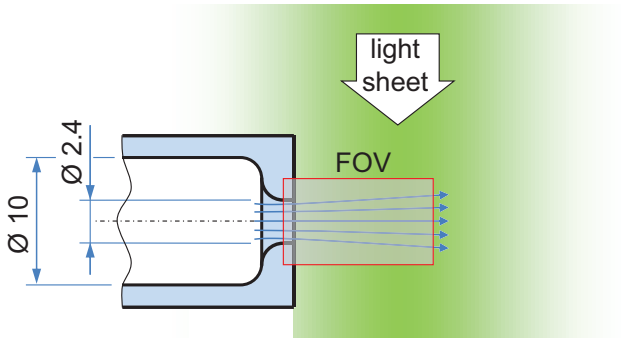

Figure 3.13: Sketch of the axis-symmetric pipe exit for the jet flow analysis. The laser light sheet and the field of view (FOV) are illustrated. Numerical values are given in mm.

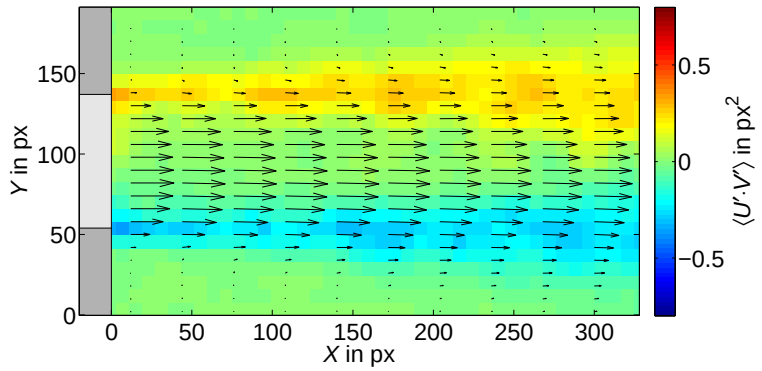

(a) 16×16 px window-correlation: every $4th$ vector in $X-$direction and each vector in $Y-$direction is shown.

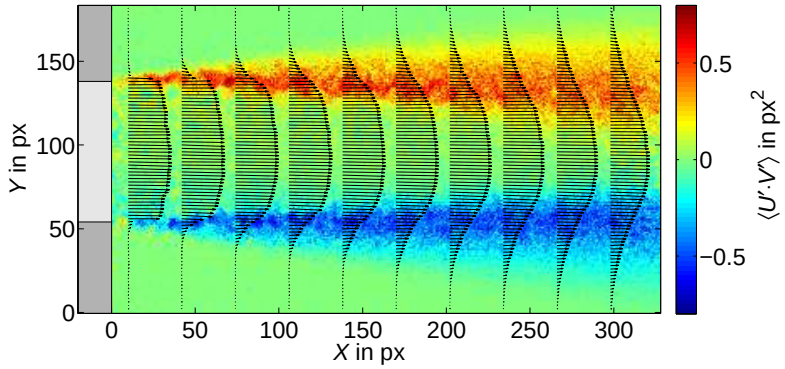

(b) ensemble correlation: every $32nd$ vector in $X-$direction and every $2nd$ vector in $Y-$direction is shown.

Figure 3.14: Reynolds shear stress distribution and velocity vectors for a round water jet at $\mathrm{Re_d} = 26{,}000$ computed with 16×16 px windows-correlation (a) and single-pixel ensemble-correlation (b) and from 25,000 PIV recordings.

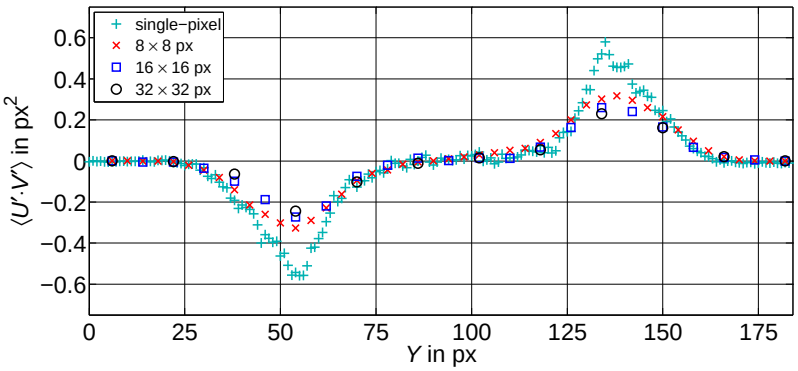

Figure 3.15: Reynolds shear stress for a cross section of the jet flow from Fig. 3.14 at $X = 150\,\mathrm{px}$.

leading more than 10,000 independent Reynolds shear stress data points for a digital particle image diameter of $D \approx 1.9\,\mathrm{px}$, according to Chapter (2.3). A locally active filter was used to replace single outliers by the median value of the surroundings.

The comparison of the flow fields computed using window-correlation and single-pixel ensemble-correlation shows a similar distribution: A shear layer with positive shear stress in the upper part and one with negative shear stress in the lower part. Both shear layers grow in thickness with propagation, while the broadening is proportional to the distance from the nozzle. Although, this measurements were not performed in the self-preserving region, this results are in agreement with the analysis on the self-preserving region of a round jet made by Wygnanski and Fiedler (1969).

Regarding the comparison in Fig. 3.14, a significantly better spatial resolution was achieved with the developed single-pixel method. Furthermore, it is evident that the absolute values of the shear stresses are considerably higher in the case of single-pixel evaluation. Referring to the example of synthetic PIV images from Fig. 3.8, these values are more reliable than those obtained from window-correlation. The single-pixel results are neither spatially low-pass filtered by the correlation-window size, nor do they suffer from error propagation during the calculation of Reynolds stresses from individual vector fields.

Additionally, the velocity vectors in Fig. 3.14 clearly show that only the single-pixel approach is capable of resolving the very high velocity gradients right behind the nozzle exit. The window-correlation method only computes mean values averaged over the window size.

Conclusions

The presented chapter illustrates that Reynolds normal and shear stresses can be estimated in general from the shape of the correlation function. This allows for computing

statistical values with significantly increased spatial resolution compared to standard window-correlation. It should be emphasized here, that the spatial resolution of the estimated Reynolds stresses is limited by the digital particle image diameter in the same way as it limits the resolution of the mean displacement (see Chapter 2.3).

The developed method is suitable for PIV recordings with particle image diameters $D > 1\,\mathrm{px}$ (see Fig. 3.4a and 3.4b), whereas the optimum value is between 1.5 and 5 px. The number of images has a strong impact on the accuracy of the computed stresses and the mean velocity (see Figs. 3.6a, 3.6b, and 3.6c). An insufficient number of PIV images (or low seeding density) can be compensated by averaging the correlation peaks over several pixels. Velocity gradients in the observed flow stretch the correlation peaks and rotate them. This causes strong bias errors for the computed Reynolds stresses, which must be corrected by using Eqs. (3.23) -(3.25).

The application of the evaluation method on an experimental data sets in Sec. 3.3 demonstrated the suitability of this approach for the analysis of real PIV recordings. The comparison between the developed single-pixel approach and a standard evaluation using interrogation windows illustrates the increased spatial resolution and enhanced measurement precision (see Fig. 3.14). It was found that the estimated Reynolds stresses are significantly larger compared to results from standard PIV evaluations that only compute mean values averaged over the interrogation-window size.

In summary, for a PIV data set of several thousand image pairs all Reynolds stresses in a $2D$ regime can be computed with drastically improved resolution, with an error of only a few percent points. This is of great importance for the analysis of small-scale flow phenomena appearing, for instance, at large Reynolds and Mach numbers. The developed method can also be used to analyze correlation peaks from sum-of-correlation procedures, computed with conventional available software. However, in this case the received information is averaged over the interrogation-window size.

The present calculations are based on a Gaussian probability density function. For instationary flows with complex behavior, the probability density function might have to be generalized. A sum of two or more Gaussian functions like the one defined in Eq. (3.8) should solve a variety of problems.

4 Detection of vortices from PIV vector fields

The formation and motion of vortices is of fundamental importance for space launcher's wake flows. Schrijer et al (2011) as well as Hannemann et al (2011) showed that in the case of the *ARIANE V* the flow separates at the end of the main stage and vortices are generated in the shear layer, as discussed in the introduction of the thesis. These vortices may interfere with the main engine's nozzle or other components and can cause serious damage.

To analyze the risk for components in the wake it is important to know where the vortices are generated and which way they are traveling. Additionally, the size and strength of the vortices need to be known to estimate the danger caused by them. PIV is in principle well suited to measure all these quantities, since it evaluates instantaneous vector fields from which the vortices can be identified. In order to determine the range of detectable vortices, synthetic PIV images of vortices with different size and swirling strength will be analyzed in this chapter.

Section 4.1 discusses how the vortices are identified from the velocity vector fields by using the discriminant of the velocity gradient matrix. The influence of the interrogation-window size and the window overlapping on the estimated vortex size and the swirling strength is analyzed in Secs. 4.2 and 4.3, respectively. Section 4.4 discusses the possibility to estimate the vortex tube orientation with respect to the measurement plane.

4.1 Identification of vortices

The Lamb-Oseen vortex is a frequently used vortex model in fluid dynamics. It is based on a relatively simply mathematical description, which is close to real vortices. The circumferential velocity component V_φ of this vortex model is given by the following equation:

$$V_\varphi(r) = \frac{\Gamma}{2\pi r}\left(1 - \exp\left[\frac{-r^2}{r_c^2}\right]\right) \tag{4.1}$$

Where Γ is the total circulation and r_c the vortex core radius. Figure 4.1 illustrates the circumferential velocity (green line) for a cross section through the vortex center. In principle the vortex projection on the measurement plane can be directly identified from

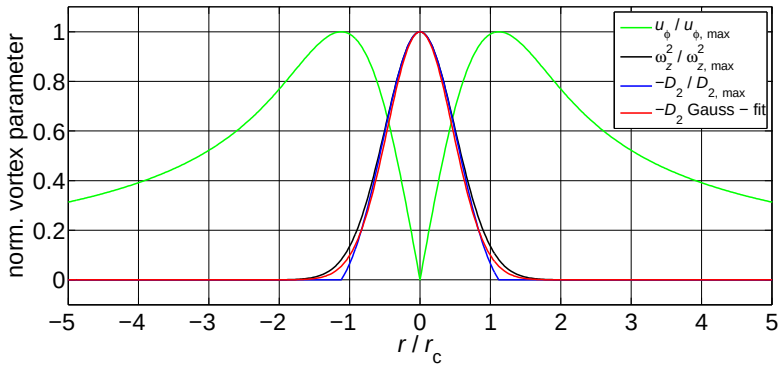

Figure 4.1: Normalized circumferential velocity and swirling strength for a Lamb-Oseen vortex.

the velocity field. However, this becomes difficult in the case of an additional drift velocity. The superposition of a vortex and a constant velocity field can be analyzed using the vorticity. For a velocity field in the $xy-$plane the vorticity around the $z-$axis is given by:

$$\omega_z = \frac{\partial u}{\partial y} - \frac{\partial v}{\partial x} \tag{4.2}$$

If the vortex is superimposed with a shear layer the vorticity is not a sufficient indicator. In this case the non-real eigenvalues of the velocity gradient matrix

$$\frac{\partial \vec{v}}{\partial \vec{x}} = \begin{pmatrix} u_x & u_y \\ v_x & v_y \end{pmatrix} = \begin{pmatrix} \frac{\partial u}{\partial x} & \frac{\partial u}{\partial y} \\ \frac{\partial v}{\partial x} & \frac{\partial v}{\partial y} \end{pmatrix} \tag{4.3}$$

can be used to identify vortices (Chong et al, 1990; Vollmers, 2001; Adrian et al, 2000). The discriminant

$$D_2 = \left(\mathrm{trace}\frac{\partial \vec{v}}{\partial \vec{x}}\right)^2 - 4 \cdot \det \frac{\partial \vec{v}}{\partial \vec{x}} = (u_x + v_y)^2 - 4 \cdot (u_x \cdot v_y - u_y \cdot v_x) \tag{4.4}$$

of the velocity gradient matrix is negative for vortices and positive for other patterns. Figure 4.1 shows that the squared vorticity ω_z^2 and the discriminant of the velocity gradient matrix D_2 have the same shape if no drift velocity is superimposed. On the other hand, Fig. 4.2 illustrates the influence of an additional constant velocity and of an additional shear layer. From the figure it can be concluded that the vorticity is not sufficient to identify vortices in the case of a superimposed shear layer, whereas the discriminant of the velocity gradient matrix is sufficient. Thus D_2 will be used to identify vortices in the following.

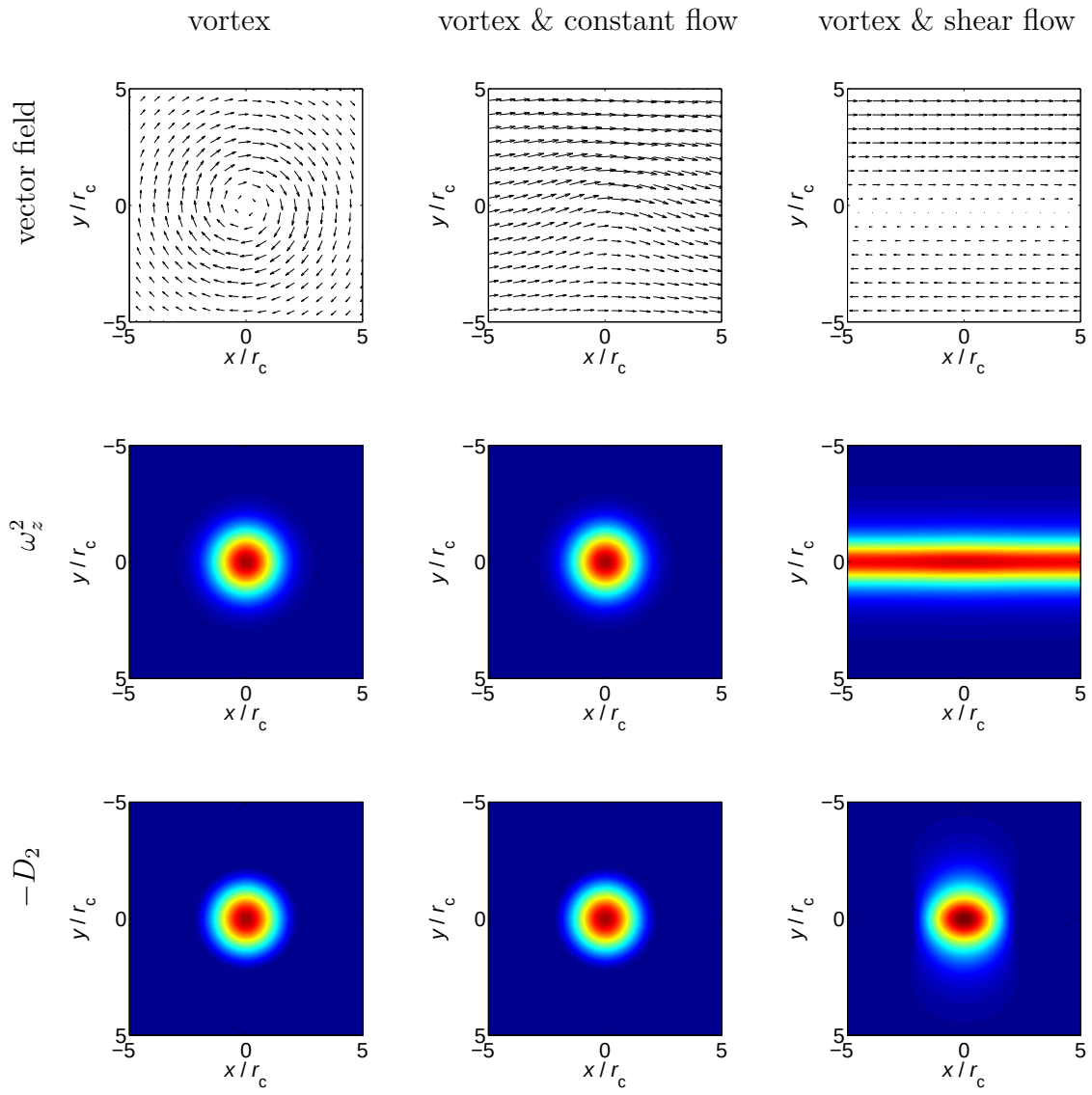

Figure 4.2: Velocity vector field (top row), vorticity squared (middle row) and discriminant of the velocity gradient matrix (bottom row) for a Lamb-Oseen vortex (left column), for an additional constant drift velocity (middle column) and for an additional shear layer (right column).

4.2 Estimation of vortex size

Window-correlation based PIV evaluation methods result in volume averaged velocity vectors as discussed in Sec. 2.2.1. Thus, it is expected that small vortices (smaller than the interrogation-window size) are smeared out and cannot be detected reliable. The aim of this section is to analyze the detectability of vortices with respect to their size and with respect to the interrogation-window size using window-correlation based PIV.

In order to investigate vortices of different sizes synthetic images are generated, as discussed in Sec. 2.3.3. 100 synthetic image pairs, 512×512 px in size, with a stationary Lamb-Oseen vortex in the image center were generated for different vortex core sizes ranging from $r_c = 1\,\text{px}$ to $r_c = 100\,\text{px}$. A particle image density of 25% was applied, meaning that 25% of the image area was covered by particle images. The digital particle image diameter was $D = 3\,\text{px}$, hence, the number of particle images per pixel was $N_{ppp} = 0.035$ on average, according to Eq. (2.8). A Gaussian particle image shape was assumed and the maximum intensity of the particle images was $I_0 = 2^{14}$. A Gaussian noise with zero mean and a standard deviation of $I_0/100$ was added to the images, leading to a SNR of 100. The particle image positions in the second frame were shifted with respect to those in the first one: The distance to the vortex center was kept constant and the angular displacement was computed from Eq. (4.1). A maximum shift of 10 px was applied.

The PIV images were evaluated with window-correlation methods including image deformation, iterative window shifting and Gaussian window weighting by using a standard software (*Davis* by LaVision). The interrogation-window size for the first pass was 64×64 px, for the final pass different window sizes were tested. For each interrogation-window size at least two passes were performed. Due to the large particle image density and the high SNR no post-processing was required.

In order to detect the generated vortices the swirling strength *swirl* of the vector fields were computed as follows:

$$swirl = \max\left(0; -D_2\right) \cdot \text{sign}\left(\omega_z\right) \tag{4.5}$$

Where *swirl* is the negative part of the discriminant of the velocity gradient matrix. The multiplication by the sign of the vorticity ω_z allows for the determination of the rotation direction: negative swirling strength corresponds to clockwise rotation and positive swirling strength corresponds to counter-clockwise rotation. The swirling strength distribution of all vector fields was used to detect the vortices: The cross-correlation between the swirling distribution and a set of Gaussian peaks with different diameters was computed, as described in Cierpka et al (2008). Thus, a three dimensional correlation map was formed, which allows to identify the vortex position (x_0,y_0) and the vortex core radius r_c. Additionally, the correlation value itself indicates how good the shape of the detected vortex follows the shape of the Gaussian.

Figure 4.3 shows the estimated vortex size with respect to the simulated one. Each

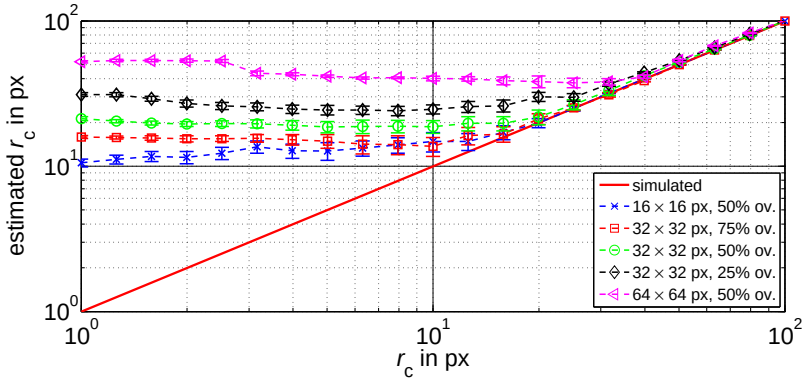

Figure 4.3: Estimated vortex core radius with respect to the simulated core radius for different interrogation-window sizes and different overlapping.

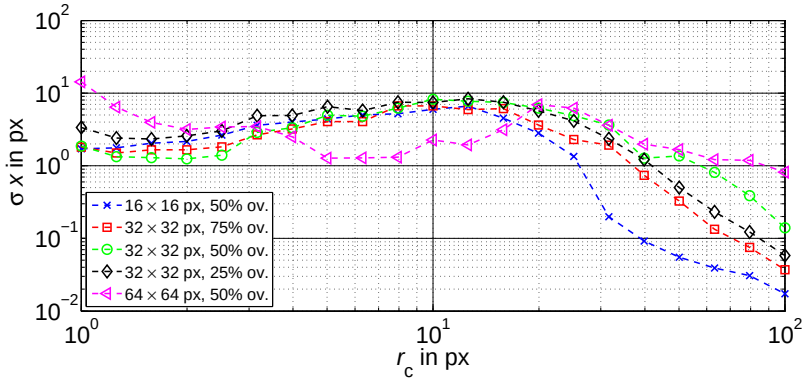

Figure 4.4: Random error of the estimated vortex center position with respect to the simulated core radius for different interrogation-window sizes and different overlapping.

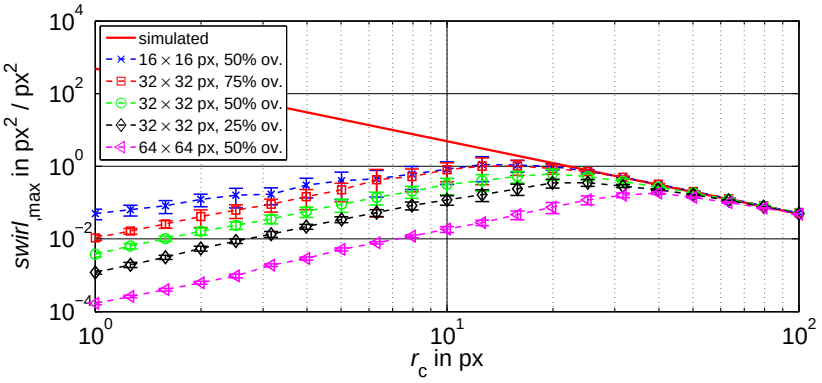

Figure 4.5: Estimated swirling strength with respect to the simulated core radius for different interrogation-window sizes and different overlapping. The simulated swirling strength is indicated by the red solid line.

measurement point represents an average value over 100 vortices and the error-bar indicates the corresponding standard deviation. Three different interrogation-window sizes were used ranging from 16×16 px to 64×64 px. Additionally, different overlaps of 25%, 50%, and 75% were tested for one window size. The results in Fig. 4.3 clearly show that the vortex size of small vortices is overestimated. The smallest size that can be detected without a significant bias error depends on the vector grid spacing (window size times overlap) rather than on the interrogation-window size. Thus, a large overlap allows to detect smaller vortices without bias. On the other hand, it should be emphasized that due to the high SNR also the smallest vortices could be detected although their size is drastically overestimated. For small vortices ($r_c < 10$ px) the estimated size is rather independent of the simulated vortex size but strongly dependents on the interrogation-window size and the window overlap, as can be seen from the constant slope in the left part of Fig. 4.3.

The random error of the detected vortex center positions σx is illustrated in Fig. 4.4. It was computed from the distance between the simulated and estimated center position, whereas the simulated position was the image center plus a random number between -16 px and $+16$ px. From Fig. 4.4 it can be seen that only the position of the larger vortices could be determined correctly. The remaining uncertainty depends mainly on the interrogation-window size, whereas the best results are obtained for small windows. The window overlap seams to have minor influence on the accuracy of the estimated vortex center position.

4.3 Estimation of swirling strength

The same data set as discussed in the previous section was used to analyze the effect of the vortex size on the estimated swirling strength. For a vortex core radius of $r_c = (1 \ldots 100)$ px 100 synthetic PIV image pairs were generated and analyzed with window-correlation

using different interrogation-window sizes and overlapping. The results are shown in Fig. 4.5. As before, each measurement point represents an average value over 100 vortices and the error-bar indicates the corresponding standard deviation. From Fig. 4.5 it is evident that only for large vortices the swirling strength is determined correctly. For small vortices the swirling strength is underestimated, since mainly the outer region of the vortex is captured. The bias error strongly depends on the interrogation-window size as well as on the window overlap. The smallest vortex size for which the swirling strength can be determined accurately is in the range of the interrogation-window size.

4.4 Estimation of vortex orientation

Only for the case that the vortex-tube axis is perpendicular to the measurement plane the swirling distribution is axisymmetric. Otherwise, if the vortex tube is cut under an arbitrary angle its cross section is an ellipse. The angle between the vortex-tube axis and a axis normal to the measurement plan is referred to as β. For $\beta \neq 0$ the swirling distribution is stretched. Furthermore, the resulting ellipse can be stretched in any direction within the measurement plane depending on the azimuthal angle γ of the vortex tube, illustrated in Fig. 4.6.

To account for that, the swirling distribution is analyzed locally with a fit function. The information about location and size of the correlation procedure discussed in Sec. 4.2 are used as start point. The fit-function allows to include more parameters, thus, it is possible to compare the swirling distribution to a Gaussian with an elliptical cross-section:

$$swirl(x,y) \approx \exp\left[-\left(\frac{\cos\gamma\cdot(x-x_0)-\sin\gamma\cdot(y-y_0)}{L_1}\right)^2\cdot 8-\left(\frac{\sin\gamma\cdot(x-x_0)+\cos\gamma\cdot(y-y_0)}{L_2}\right)^2\cdot 8\right] \tag{4.6}$$

Where L_1 and L_2 are the major and minor axis length and γ is the angle of orientation. The angle between the vortex-tube axis and a axis normal to the measurement plan can be computed from the ratio of the minor and major ellipsis axis:

$$\cos\beta = \frac{L_2}{L_1} \tag{4.7}$$

Thus, both angles β and γ can be extracted from the elliptical fit function.

In order to test the ability to measure the angles β and γ synthetic PIV images were generated and analyzed, as before. Figure 4.7a shows the results for a varying angle β. The measurement points represent the mean value over 100 vortices and the error-bar indicates the corresponding standard deviation. The simulated vortex core radius was $r_c = 25$ px and the evaluation was performed using 16×16 px interrogation windows. From Fig. 4.7a it can be seen that angles between 20° and 80° can be detected accurately. For small angles the ration L_2/L_1 is close to one, where the inverse cosine has a very steep slope which causes increased uncertainty. The random error of the vortex major and

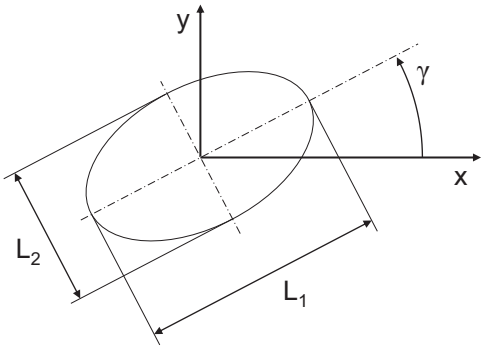

Figure 4.6: Sketch of the vortex core cross section in the measurement plane. The swirling distribution appears generally as rotated ellipse.

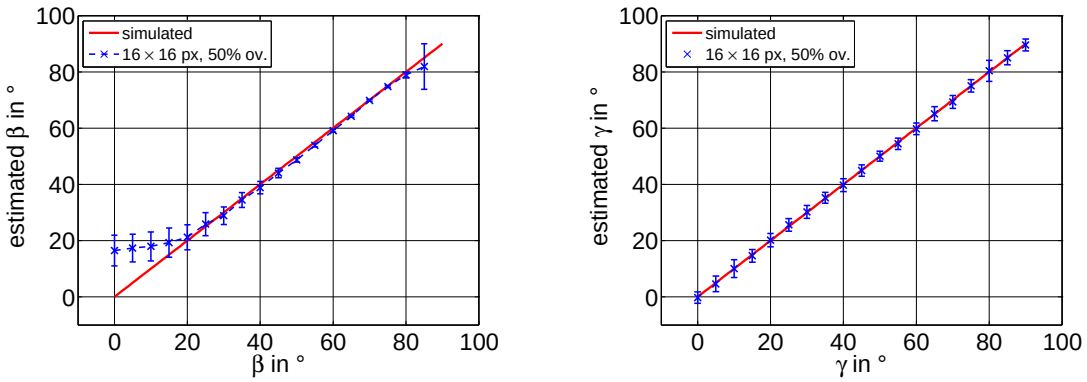

(a) (b)

Figure 4.7: Estimation of the angle of inclined vortex-tube axis β and the azimuthal angle γ from synthetic PIV images evaluated with window-correlation.

minor axis length L_1 and L_2 causes a slightly elliptical shape for round vortices, in general. As a result, the angle beta is overestimated for vortex tubes that are aligned (almost) perpendicular to the measurement plan.

To investigate the detectability of the azimuthal angle γ another set of synthetic images was generated: The angle β was kept constant at 45° and the angle γ varied from 0 to 90°. Thus the swirling distribution has an elliptical shape, whereas the ratio L_2/L_1 is approximately 0.7 (according to Eq. (4.7)) and the in-plane orientation varied with γ. The data set was again analyzed using 16×16 px interrogation windows with 50% overlap, the swirling distribution was computed according to Eq. (4.5) and it was approximated by the Gaussian fit-function from Eq. (4.6). Figure (4.7b) shows the estimated orientation of the detected ellipses with respect to the simulated one. It can be seen that the azimuthal angle γ can reliable be detected over the tested range.

Conclusions

This Chapter illustrates that vortices can be detected from PIV vector fields. Using the discriminant of the velocity gradient matrix allows to distinguish between shear and vorticity, which is very important for the detection of vortices within a shear layer. Synthetic Lamb-Oseen vortices were used to analyze the detectability of vortices from PIV vector fields. The vector fields were computed from synthetic images by using window-correlation based PIV evaluation methods implemented in a standard software. It was shown, that even vortices that are much smaller than the interrogation-window size can be detected with the developed approach. However, in this case the vortex size is overestimated and the swirling strength is underestimated. The interrogation-window size and the window overlapping strongly influence the minimum size of vortices whose size and swirling strength can be detected reliable. This minimum size is generally in the order of the interrogation-window size.

If the vortex-tube axis is not aligned perpendicular to the measurement plane the shape of the swirling distribution becomes elliptical. Using a Gaussian fit-function with an elliptical shape allows for the estimation of the orientation of the vortex tube.

In the case of real PIV images the error level of the estimated velocity vector filed can be much higher than applied for the simulations. As a result, the gradients are also erroneous and the swirling distribution might show small peaks that look like vortices but are only measurement noise. Thus, the detection of vortices with a size smaller than the interrogation window is challenging for real PIV data.

The developed approach will be applied to experimentally achieved vector fields of a generic space launcher model's wake in Chapter 5, where the spatial distribution of the detected vortices is shown with respect to their size, to their swirling strength and to the vortex tube orientation.

5 Transonic wake flow of a generic space launcher model

The wake flow of a space launcher is of fundamental importance for its aerodynamic performance, as motivated in the introduction of this thesis. In this Chapter, a detailed analysis of a generic space launcher model's wake flow by means of PIV measurements is presented. Reliable and accurate measurements of the mean velocity distribution and the Reynolds stress distribution with high spatial resolution are important for the validation of modern simulation concepts or for the comparison with other measurements. Furthermore, a detailed analysis of the wake flow reveals fundamental understanding of the flow physics. Transonic Mach numbers are of particular interest, because at moderate heights, the ambient conditions (air pressure and density) cause strong flow/ structure-interactions that lead to high mechanical stresses in the involved components (Hannemann et al, 2011; Schrijer et al, 2011).

The fluid mechanical principles of a space launcher's wake can be described by a very simple model: the backward-facing step. Although many publications concentrated on the backward-facing step flow, only a very limited amount of experimental data on axisymmetric models is available, especially for high subsonic or transonic Mach numbers. The objective of this Chapter is a detailed analysis of a axisymmetric backward-facing step's flow field at Ma = 0.7 with sophisticated PIV evaluation methods.

This Chapter is structured as follows: Section 5.1 describes the measurement setup. The acquired date set was analyzed with respect to different aspects: The mean velocity field is presented and discussed in Sec. 5.2. The spatial distribution of the Reynolds normal and shear stress in the space launcher model's wake is analyzed in Sec. 5.3. Section 5.4 presents the spatial distribution of shear layer vortices with respect to their size, swirling strength and orientation. Additionally, two-point correlation is applied to instantaneous velocity fields in order to identify coherent structures.

5.1 Measurement setup

The measurements were performed in the Trisonic Wind tunnel Munich (TWM) at the Bundeswehr University. The facility is described in detail in Sec. 5.1.1. The space launcher model and the setup of the high-repetition PIV system used are discussed in Sec. 5.1.2 and 5.1.3, respectively.

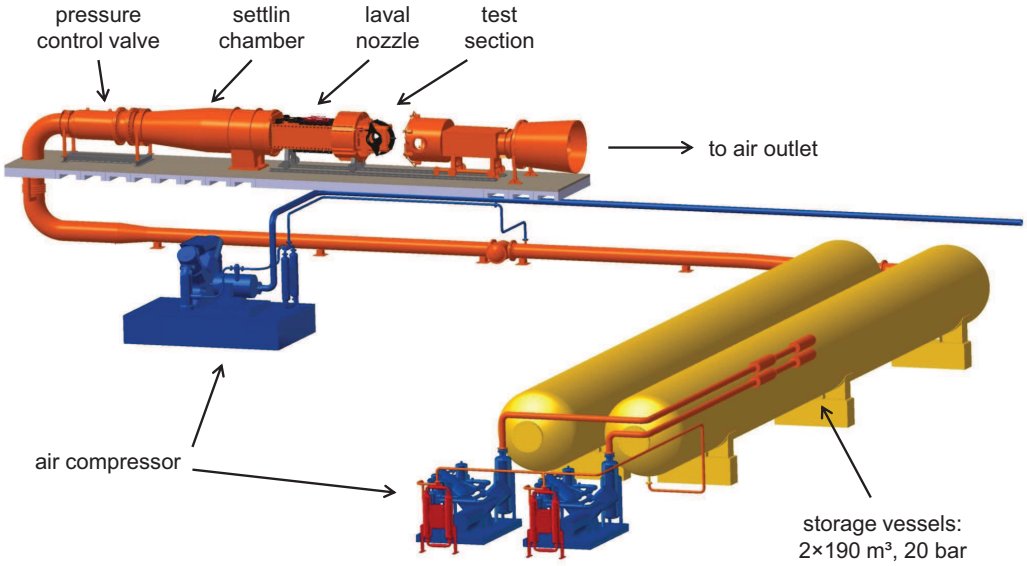

Figure 5.1: Sketch of the TWM

5.1.1 TWM

The Trisonic Wind tunnel Munich (TWM) facility is equipped with independently adjustable Laval nozzle and diffuser and it is therefore capable of generating sub-, trans-, and super-sonic flow. The TWM is a blow down type wind tunnel with two 30 m long storage vessels each with a volume of 190 m^3 (yellow in Fig. 5.1). Three air compressors with a total power of roughly 650 kW achieve a volume flow rate of 4,000 m^3/h. The compressed and dried air is stored in the two vessels at a maximum pressure of 20 bar. Less than 2 hours are required for a complete filling of the storage vessels.

The upper part of Fig. 5.1 shows the flow control devices, which are needed for adjusting Reynolds number and Mach number independently. During a wind tunnel run the pressure in the settling chamber is adjusted by the control valve in a closed-loop regime. While the pressure in the storage vessels drops continuously, the control valve is opened more and more so that the pressure in the settling chamber is kept constant. The total pressure range of the wind tunnel is $p_t = (1.2 \ldots 5)$ bar. This leads to a Reynolds number range of $\mathrm{Re} = (7 \ldots 80)\ \mathrm{m}^{-1}$.

For the PIV measurements the flow is seeded with DEHS tracer particles via a flange fitted to the wall of the settling chamber close to the control valve (see Fig. 5.1). The settling chamber is several meters long and has a diverging cross section. After the flow settles down, it passes several flow straighteners at the end of the settling chamber to reduce the lateral turbulence level. After setting the Reynolds number and reducing the turbulence level, the Mach number is adjusted in the Laval nozzle, which has a rectangular cross section with continuously deformable side walls. A Mach number range between 0.3 and

3.0 can be obtained. For a Mach number of 0.7 the turbulence level in the test section of the TWM facility is approximately 1.3% of the mean velocity.

The 675 mm high, 300 mm wide and 1,200 mm long test section can be equipped with solid or perforated walls. The latter allows for boundary-layer suction. Both side walls have round windows, 500 mm in diameter, for optical access to the test section. Additionally, the ceiling is equipped with a 200 mm window for optical investigations. Models can be mounted either on one of walls or on a rear sting. In both cases, the angle of attack can be controlled by means of a hydraulic adjusting unit. The test section is surrounded by the plenum chamber, which is opened pneumatically in order to get full access to the inside. Just before reaching the air outlet, through a tower outside the building (not shown in Fig. 5.1), the flow passes through the adjustable diffuser. The operating time of the TWM facility depends on the adjusted Reynolds and Mach number, it reaches up to 300 seconds at Mach = 3. The maximum flow rate of 240 kg/s is achieved at Mach = 1 and $p_t = 5$ bar. In this case the run-time of the facility is still approximately 40 seconds.

5.1.2 Space launcher model

The tests were performed on a blunt axisymmetric space launcher model, shown in Fig. 5.2. The configuration consists of a 36° cone with a spherical nose of $R = 5$ mm and a cylindrical part with a length of 164.3 mm and a diameter of $d = 54$ mm. The total length, from nose to base, is 231.3 mm. The model was made of aluminum and the surfaces were polished to avoid diffuse reflections at the wall, which would bias the near wall PIV velocity measurements, see Kähler et al (2006).

A rear sting (Ø21.5 mm) in the base of the cylinder was used for mounting the model in the test section of the wind tunnel. Compared to a strut-mounting, the rear sting avoids strong three-dimensional effects on the flow in a nnd around the base region of the model (see van Oudheusden and Scarano (2008)). A sketch of the model and the field of view (FOV) are shown in Fig. 5.3.

5.1.3 PIV system

For the PIV measurements the flow is seeded with DEHS tracer particles with a mean diameter of 1 µm, as described in (Kähler et al, 2002). Due to the limited run time of the facility and the large number of recordings required for reliable data, a high-repetition PIV system using a Quantronix Darwin Duo Nd:YLF double-pulse laser with a wavelength of 527 nm, a pulse duration of $t_p \approx 120$ ns, and a laser energy of 11 mJ per cavity at 2 kHz was used. The laser beam is transformed into a light sheet using two spherical lenses for adjusting the height, followed by two cylindrical lenses for width adjustment. The M^2-factor of the laser was approximately $M^2 \approx 25$, which led to a light sheet thickness in the focal plane of ≈ 1.5 mm for the chosen setup.

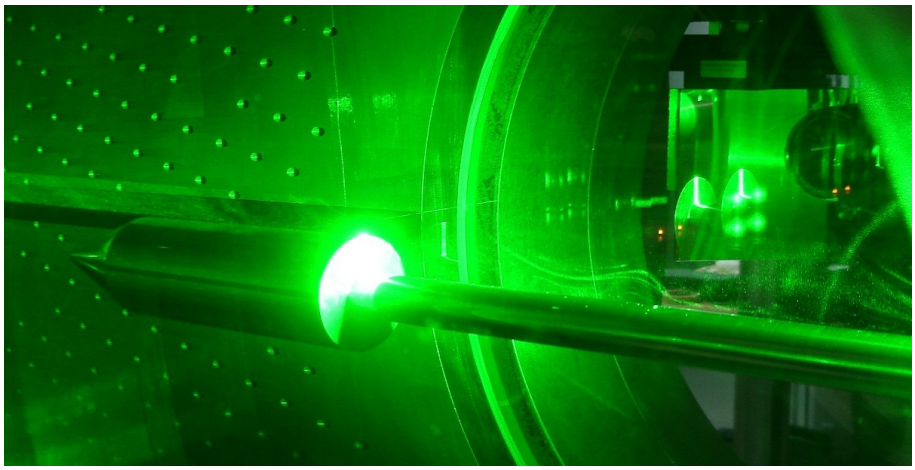

Figure 5.2: Generic space launcher model mounted in the test section of the TWM.

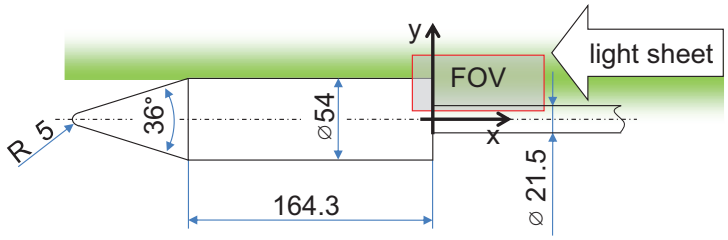

Figure 5.3: Axisymmetric space launcher model with rear sting. The laser light sheet and the field of view (FOV) for high-repetition rate PIV measurements are illustrated. Numerical values are given in mm.

The recordings were captured by using a *Phantom V12* high repetition rate CMOS camera (by Vision Research Inc.) with a 1,280 × 800 px sensor and 8 GB of internal memory. By cropping the image's size to 1,280 × 400 px, more than 5,000 double frame PIV images could be captured during one wind tunnel run.

The time between the laser pulses was adjusted to 3 µs, which corresponds to a particle shift of < 0.7 mm between the tow illuminations of one double frame image (or < 8 pixel on the image plane). Due to the strong three–dimensional motion, this relatively short temporal difference is required to ensures that a large fraction of the tracer particles is observed in both frames. The recording rate was adjusted to2,000 image pairs per second. Since the vortex shedding frequency is around 900 Hz (Bitter et al, 2012), the images are considered as uncorrelated, which is essential for the computation of statistical values.

A $Makro - PlanarT * f2/100$ objective lens (by Carl Zeiss AG) with a focal length of 100 mm and an f-number of 2.8 was mounted in front of the camera. The camera was located inside the plenum chamber in order to reach a small working distance, which is required for good resolution and high SNR, as discussed in Chapter 2.3. The most relevant measurement parameters are summarized in Tab. 5.1.

5.2 Mean velocity field

The analyzed data set was acquired at a Mach number of Ma = 0.7 and a Reynolds number of $\mathrm{Re_d} = 1.1 \cdot 10^6$ (related to the forebody's diameter $d = 54$ mm). A total number of 21,500 PIV image pairs was acquired in four wind tunnel runs at a recording frequency of 2 kHz. During the wind tunnel run the space launcher model vibrates in the $y-$ and $z-$directions. The motion is dominated by a frequency of ≈ 37 Hz and the amplitude reaches ± 1 mm ($= \pm 11$ px), which corresponds to a variation of the angle of attack of $\pm 0.2°$ (Bitter et al, 2011). As a result the model moves slightly up and down in the recorded images. Furthermore, due to the out of plane motion the measurement plane moves with respect to the model's symmetry axis. This slightly increases the thickness of the averaging volume.

In a first evaluation step a high-pass filter was applied to the intensity distribution of each pixel over the ensemble, as introduced by Scarano and Sciacchitano (2011). This procedure eliminates wall reflections and enhances the particles peak intensity relative to the reflections and the background light. Secondly, the images were shifted to compensate for the space launcher model's in-plane motion. In the next step, the correlation function was computed for each pixel using the single-pixel evaluation discussed in Sec. 2.2.2. Finally, the mean velocity was estimated from the correlation peak's maximum position.

Figure 5.4a shows the mean shift vector field computed from 21,500 PIV image pairs using single-pixel ensemble-correlation. In the $x-$direction, every 50^{th} vector is shown and in the $y-$direction every 10^{th}. According to the findings of Chapter 2.3 the spatial resolution of the vector field is $res \approx D \cdot S/M = 2\,\mathrm{px} \cdot 90\,\mu\mathrm{m/px} = 180\,\mu\mathrm{m} = 0.003 \cdot d$.

Table 5.1: Overview of the measurement parameters.

Wind tunnel & model	
Mach number	$\mathrm{Ma} = 0.7$
Reynolds number	$\mathrm{Re_d} = 1.1 \cdot 10^6$
Total pressure	$p_\mathrm{t} = 1.5\,\mathrm{bar}$
Total temperature	$T_\infty = 264\,\mathrm{K}$
Measurement section size	$1200 \times 675 \times 300\,\mathrm{mm}^3$
Model diameter	$d = 54\,\mathrm{mm}$
Rear sting diameter	$21.5\,\mathrm{mm}$
Step height	$16.25\,\mathrm{mm} \approx 0.3 \cdot d$
Imaging system	
Active camera-sensor size	$25.6 \times 8\,\mathrm{mm}^2 (1280 \times 400\,\mathrm{px})$
Pixel spacing	$20 \times 20\,\mu\mathrm{m}^2$
Objective lens focal length	$100\,\mathrm{mm}$
f-number	2.8
Working distance	$450\,\mathrm{mm}$
Magnification	0.22
Scaling factor	$90\,\mu\mathrm{m/px}$
Field of view	$115 \times 36\,\mathrm{mm}^2$
Digital particle image diameter	$\approx 2\,\mathrm{px}$
Laser system	
Repetition rate	$2\,\mathrm{kHz}$
Wave length	$527\,\mathrm{nm}$
M^2	≈ 25
Divergence	$\approx 10\,\mathrm{mrad}$
Light-sheet thickness	$\approx 1.5\,\mathrm{mm}$
Pulse duration	$\approx 120\,\mathrm{ns}$
Pulse separation	$3\,\mu\mathrm{s}$
Pulse energy	$11\,\mathrm{mJ}$

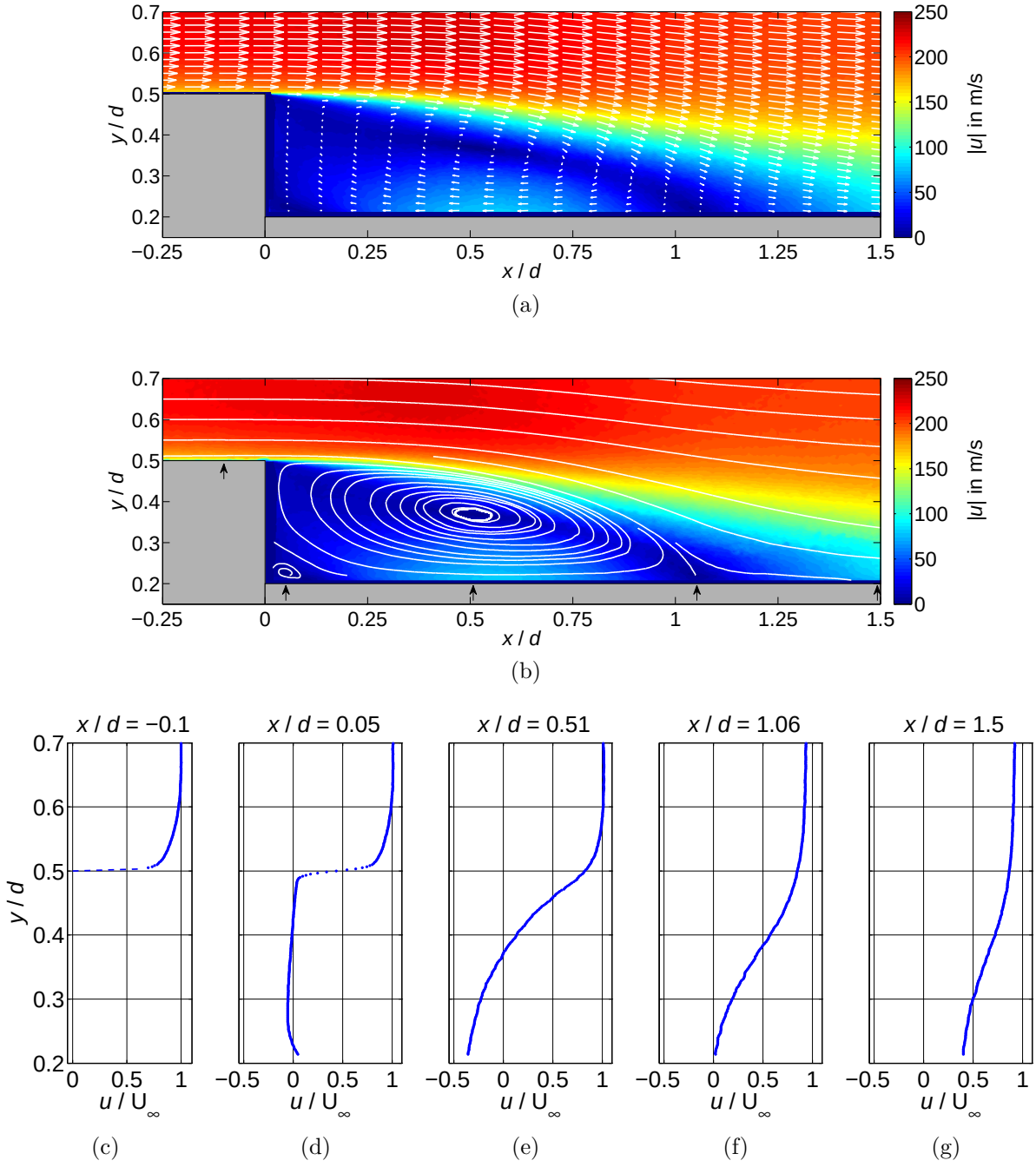

Figure 5.4: Velocity vector field (a) and stream lines (b) of the generic space launcher model's wake flow (Ma = 0.7, $\mathrm{Re_d} = 1.1 \cdot 10^6$) as well as profiles of the normalized horizontal mean velocity (c) at the end of the cylindrical forebody, (d) shortly after separation, (e) at the center of the primary recirculation region, (f) at reattachment and (g) after reattachment.

Table 5.2: Location of the characteristic points of the space launcher's wake flow.

Characteristic point	x/d	y/d
Separation	0	0.5
Reattachment	0.2	1.06 ± 0.03
Center of primary recirculation region	0.51 ± 0.02	0.37 ± 0.02
Re-separation	0.3 ± 0.05	0
Re-reattachment	0	0.28 ± 0.02
Center of secondary recirculation region	0.05 ± 0.02	0.23 ± 0.02
Maximum downstream velocity ($\|\vec{u}\| = 276\,\mathrm{m/s}$)	0.40 ± 0.05	0.65 ± 0.04
Maximum upstream velocity ($\|\vec{u}\| = 88\,\mathrm{m/s}$)	0.56 ± 0.05	0.22 ± 0.02

Entering the field of view from the left side at $x/d = -0.25$, the mean flow features a fully developed turbulent boundary layer. The main flow direction is from left to right parallel to the $x-$ axis. The axisymmetric backward facing step at $x/d = 0$ causes a strong flow separation: A thin shear layer is formed at the end of the cylindrical fore body, which broadens further downstream. At $x/d = 1.06 \pm 0.03$ the ensemble-averaged flow reattaches on the rear sting. The stream-wise extension of the recirculation region corresponds to 3.52 times the step height, which is slightly shorter than numerical predictions presented by Deck et al (2007). The difference might be due to a larger turbulence level in the experiment. Inside the dividing streamline a distinct recirculation region develops, wherein the maximum upstream mean velocity is $\approx 88\,\mathrm{m/s}$.

The streamlines of the mean wake flow in Fig. 5.4b clearly show an out-of-plane motion within the recirculation region; the lines do not form closed loops but they bend inwards indicating a three-dimensional motion with a fluid drain center at $x/d \approx 0.51$ and $y/d \approx 0.37$. Although the images are only $1280 \times 400\,\mathrm{px}$ in size, the single-pixel ensemble-correlation allows for the resolution of a secondary vortex in the wake's corner, which is only $\approx 50\,\mathrm{px}$ in diameter. The dividing streamline between the primary and secondary recirculation regions starts on the rear sting at $x/d \approx 0.3$ to re-separate and impinges on the base of the cylindrical main body at $y/d \approx 0.28$. The stream lines of the secondary vortex bend outwards, indicating a fluid source for the mean motion centered at $x/d \approx 0.05$ and $y/d \approx 0.23$. The most important characteristic points are summarized in Tab. 5.2.

Figure 5.4 shows characteristic profiles of the horizontal velocity component in the bottom line, extracted from Fig. 5.4a. The boundary layer upstream of the backward-facing step (Fig. 5.4c) strongly influences the wake flow topology (Bradshaw and Wong, 1972; Eaton and Johnston, 1981). The boundary layer thickness and the free stream velocity were estimated to be $\delta_{99} = (0.120 \pm 0.005) \cdot d = (6.5 \pm 0.3)$ mm and $U_\infty = (237 \pm 1)$ m/s, respectively.

According to Bradshaw and Wong (1972), this backward-facing step can be considered as a strong perturbation, since the incoming boundary layer thickness is of the same order as

the step height, which is $0.301 \cdot d$. The displacement thickness at $x/d = -0.1$ is:

$$\frac{\delta_1}{d} = \frac{1}{d}\int_{0.5\mathrm{d}}^{\infty}\left[1 - \frac{u\,(y)}{u_\infty}\right]\mathrm{d}y > 0.0106 \tag{5.1}$$

and the momentum thickness is:

$$\frac{\delta_2}{d} = \frac{1}{d}\int_{0.5\mathrm{d}}^{\infty}\frac{u\,(y)}{u_\infty}\left[1 - \frac{u\,(y)}{u_\infty}\right]\mathrm{d}y > 0.0091 \tag{5.2}$$

leading to a shape factor of $H_{12} = \delta_1/\delta_2 \approx 1.17$. Thus, for the analyzed Mach and Reynolds number combination the boundary layer at the end of the main body is fully turbulent. The digital particle image diameter was around $D \approx 2\,\mathrm{px}$ (corresponding to $180\,\mu\mathrm{m}$). Thus, for single-pixel evaluation the first reliable data point, which is closest to the wall, has a wall-normal distance of $y^* = 90\,\mu\mathrm{m}$, according to the analysis in Chapter 2.4. From the last data points, the near wall gradient was estimated to be $\partial u/\partial y|_{y=0.5} > 8.6 \cdot 10^5\ \mathrm{s}^{-1}$. Hence, the wall-shear stress is $\tau_\mathrm{w} > 14.3\,\mathrm{N/m^2}$ according to Eq. (2.15) and the friction velocity is $u_\tau > 3.16\,\mathrm{m/s}$ according to Eq. (2.14) ($\mu = 1.66 \cdot 10^{-5}\,\mathrm{Pa \cdot s}$, $\rho = 1.43\,\mathrm{kg/m^3}$).

The viscous sub-layer could not be resolved with the chosen setup. A higher resolution would be required for this task. However, due to the model motion during the wind tunnel run, the near-wall resolution is limited to the accuracy of the shift correction of the PIV images, which is about 0.05 px. Furthermore, the out-of-plane motion shifts the measurement plane with respect to the model's symmetry axis. As a result, the estimated mean velocity vectors represent an average over a volume whose width depends on the out-of-plane vibration amplitude (and the light-sheet thickness). Thus, the resolution of PIV measurements cannot be further improved by using a higher magnification, since this only gives control of the in-plane dimensions of the averaging volume.

Figure 5.4d shows the estimated profile of the horizontal velocity component in the shear layer shortly after separation at $x/d = 0.1$. The maximum shift vector gradient on the image plane is larger than $\partial U/\partial Y = 0.5\,\mathrm{px/px}$ (corresponding to $\partial u/\partial y \approx 1.7 \cdot 10^5\,\mathrm{s}^{-1}$). The strong change of the gradient in the $y-$direction could only be measured reliable with single-pixel ensemble-correlation. Window-correlation methods would smear out the profile and underestimated the gradient as discussed in detail in Chapter 2.3.

The profile of the horizontal velocity component at the center of the recirculation region is shown in Fig. 5.4e. It is characterized by a large upstream component in the near wall region and a slightly increased outer velocity compared to the profiles at $x/d = -0.1$ and $x/d = 0.05$. The profile at the location of reattachment (Fig. 5.4f) shows a small gradient in the near-wall region and has a decreased horizontal velocity component in the outer region.Downstream of reattachment, the profile starts to develop into a turbulent boundary layer profile. The velocity profiles are in qualitative agreement with results presented in the literature (Scarano et al, 1999; Deck et al, 2007; Schram et al, 2004). But quantitatively there are significant differences: The experimental results based on

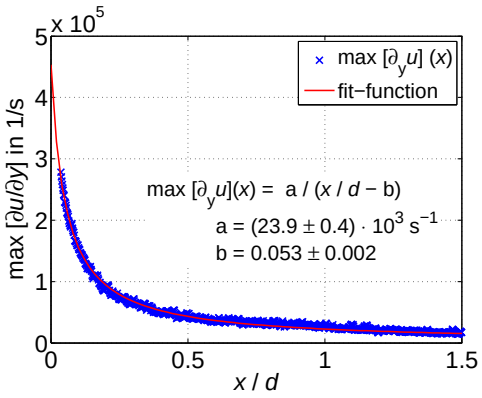

Figure 5.5: Maximum velocity gradient in the shear layer.

window correlation evaluation methods results in reduced spatial resolution. As a result, the strong gradients in the incoming boundary layer as well as in the free shear layer are underestimated.

Figure 5.5 shows the development of the maximum velocity gradient with respect to the horizontal location estimated from the velocity distribution in Fig. 5.4. A reciprocal fit function shows good agreement with the measurement points. The decay of the velocity gradient goes hand in hand with a growing shear layer thickness, which reaches values in the order of the step height downstream of reattachment.

5.3 Reynolds stress distribution

Besides the mean velocity distribution, analyzed in Sec. 5.2, the velocity fluctuations are essential to characterize the flow over the backward–facing step and to validate turbulence models used for CFD simulations. The Reynolds stress tensor summarizes the pairwise products of the fluctuations for the different directions in space:

$$\langle u_\mathrm{i} \cdot u_\mathrm{j} \rangle = \frac{1}{N} \sum_{\mathrm{n}=1}^{\mathrm{N}} (u_{\mathrm{i,n}} - \overline{u_\mathrm{i}}) \cdot (u_{\mathrm{j,n}} - \overline{u_\mathrm{j}}) \tag{5.3}$$

Where u_i and u_j are the velocity components for which the stresses are computed and N and n are the total number of vector fields and the corresponding control variable, respectively. The Reynolds normal stresses in the axial and radial direction as well as the in-plane shear stress, are analyzed in detail in this section. It should be emphasized that the Reynolds stresses are defined as the product of the pairwise velocity fluctuations and the negative mass density of the fluid (Schlichting and Gersten, 2006). However, for the sake of simplicity, only the pairwise products of the velocity fluctuations $\langle u_\mathrm{i} \cdot u_\mathrm{j} \rangle$ are identified as Reynolds stresses in the following discussion.

5.3.1 Reynolds normal stress in the axial direction $\langle u'^2 \rangle$

Figure 5.6 shows the distribution of the Reynolds normal stress in the axial direction using two different methods. Figure 5.6a illustrates the results achieved with the standard evaluation method: Window-correlation based PIV, as discussed in Sec. 2.2.1, was used to compute 21,500 vector fields with a final interrogation window size of 32×32 px and 75% overlap. The ensemble of 21,500 vector fields was used to estimate the Reynolds stress for each grid point according to Eq. (5.3). As discussed in Chapter 3, each vector represents only the mean motion averaged over the interrogation-window size. Thus, the computed Reynolds stresses are spatially low-pass filtered meaning that small turbulent structures (smaller than the interrogation-window size) are weighted lower than large ones. Consequently, the Reynolds normal stresses are underestimated. This effect is also known from hot wire anemometers, where the wire length limits the detected turbulence spectrum (Smits et al, 2011).

The results of the second method for estimating Reynolds stresses are shown in Fig. 5.6b. In this case, the whole ensemble of PIV image pairs is used to compute a map of correlation functions by using single-pixel ensemble-correlation as discussed in Sec. 2.2.2. The shape of each correlation function contains the information about the probability-density-function (PDF) of the in-plane velocity components, from which the Reynolds stresses are computed as discussed in detail in Chapter 3. In order to achieve reliable results with high accuracy, the correlation functions were averaged over 8×8 px, wich results in smooth correlation functions that allow for the reliable estimation of the PDF. With this method, also turbulent structures smaller than the pixel grid spacing are included in the Reynolds stresses and the results are no longer low-pass filtered.

Both Figs. 5.6a and 5.6b show a generally similar distribution. The normal stress in the axial direction has a maximum around $x/d \approx 0.8$ and it decreases towards the upstream part of the recirculation region as well as for locations downstream of reattachment, in agreement with the findings of Eaton and Johnston (1981). The values are close to zero in regions above $y/d = 0.5$ and close to the model's rear sting as well as to its base at $x/d = 0$. However, the results differ significantly in the following points:

- Using classical spatial correlation analysis of image pairs with window shifting and window correlation techniques (Fig. 5.6a) does not allow for reliable measurements close to the model's surface, whereas smaller interrogation-windows yield much better results, as can be seen in the first part of the shear layer in Fig. 5.6b.
- The turbulence within the shear layer, shortly after separation, is dominated by small structures which can only be detected using correlation peak analysis (Fig. 5.6c). Larger vortices, that can be detected with window-correlation are of minor importance for the thin developing shear layer.
- The single-pixel evaluation detects increasing Reynolds stresses near the surface of the rear sting at $y/d = 0.2$, see Figs. 5.6c -5.6f.

- The Reynolds stress distribution in Fig. 5.6b clearly shows two maxima and a valley in between at y/d ≈ 0.42 for the first part of the recirculation region, which can only be assumed in the case of window correlation (see also Fig. 5.6d). This valley is formed between the shear layer and the vortices fed into the recirculation region as shown in Sec. 5.4.

Profiles of the axial Reynolds stress at the location of reattachment presented in the literature (Schram et al, 2004; Eaton and Johnston, 1981; Hudy et al, 2005) are in good qualitative agreement with those in Fig. 5.6e. However, they did not report a strong increase in the near wall region. The high Reynolds stress values at the reattachment location indicate a strong fluctuation of the reattachment line. Furthermore, the two regions of high Reynolds stress intensity with the valley in between were not reported in the early works based on point–wise measurements (Bradshaw and Wong, 1972; Eaton and Johnston, 1981). Also, more recent PIV measurements by Hudy et al (2005) and Bitter et al (2011) did not resolve this topology, which is most likely due to the limited spatial resolution and spatial low-pass filtering.

5.3.2 Reynolds normal stress in the radial direction $\langle v'^2 \rangle$

Figure 5.7 shows the distribution of the Reynolds normal stress in the radial direction. Again, two evaluation methods are presented in order analyze the influence of small vortices. As before, the single-pixel PIV evaluation approach (Fig. 5.7b) results in a significantly higher Reynolds stress level, indicating that the small turbulent structures play an important role in the space launcher model's wake flow. The maximum position is similar for both methods and it is shifted downstream compared to that of the $\langle u'^2 \rangle$ −distribution. In the axial direction the $\langle v'^2 \rangle -$ distribution has its maximum at $x/d \approx 1$ close to reattachment. In this region, the vortices from the Kelvin–Helmholtz instability interact with the rear sting, they change their direction, and generate counter–clockwise rotating ones, as it will be discussed in Sec. 5.4.

The line plot at $x/d = 0.1$ in Fig. 5.7c shows that also the $\langle v'^2 \rangle$ −distribution starts directly after separation, while the larger vortices are generated further downstream. Figure 5.7d shows not a very deep valley, as in the case of $\langle u'^2 \rangle$, but two inflection points around $y/d \approx 0.4$ can be resolved in the case of the single-pixel approach. On the other hand, Figs. 5.7d - 5.7f show an inflection point close to the rear sting ($y/d \approx 0.25$) only in the case of window-correlation which is followed by a rapidly decreasing $\langle v'^2 \rangle$. This is due to the fact that only small vortices, which are not detected with window-correlation, can reach the near-wall region.

5.3.3 Reynolds shear stress $\langle u' \cdot v' \rangle$

Figure 5.8 shows the Reynolds shear stress distribution computed with window-correlation (vector based) and with single-pixel ensemble-correlation (PDF based), as before. The

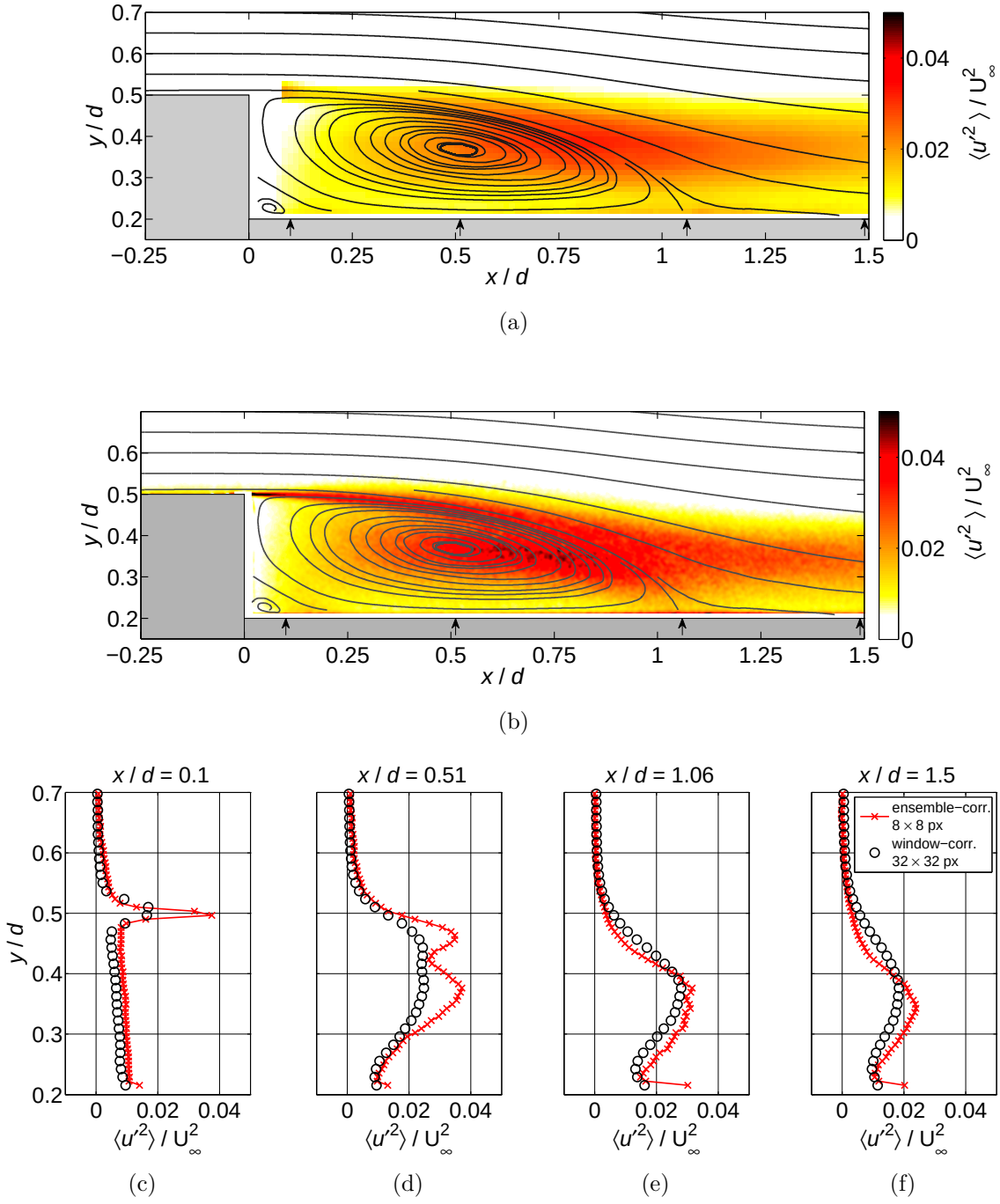

(a) (b) (c) (d) (e) (f)

Figure 5.6: Distribution of the Reynolds normal stresses in the axial direction estimated from 21,500 window-correlation vector fields with a final interrogation-window size of 32×32 px and 75% overlap (a) and from the shape of the correlation functions using single-pixel ensemble-correlation averaged over 8×8 px (b) as well as line plots shortly after separation (c), at the center of the primary recirculation region (d), at reattachment (e) and after reattachment (f).

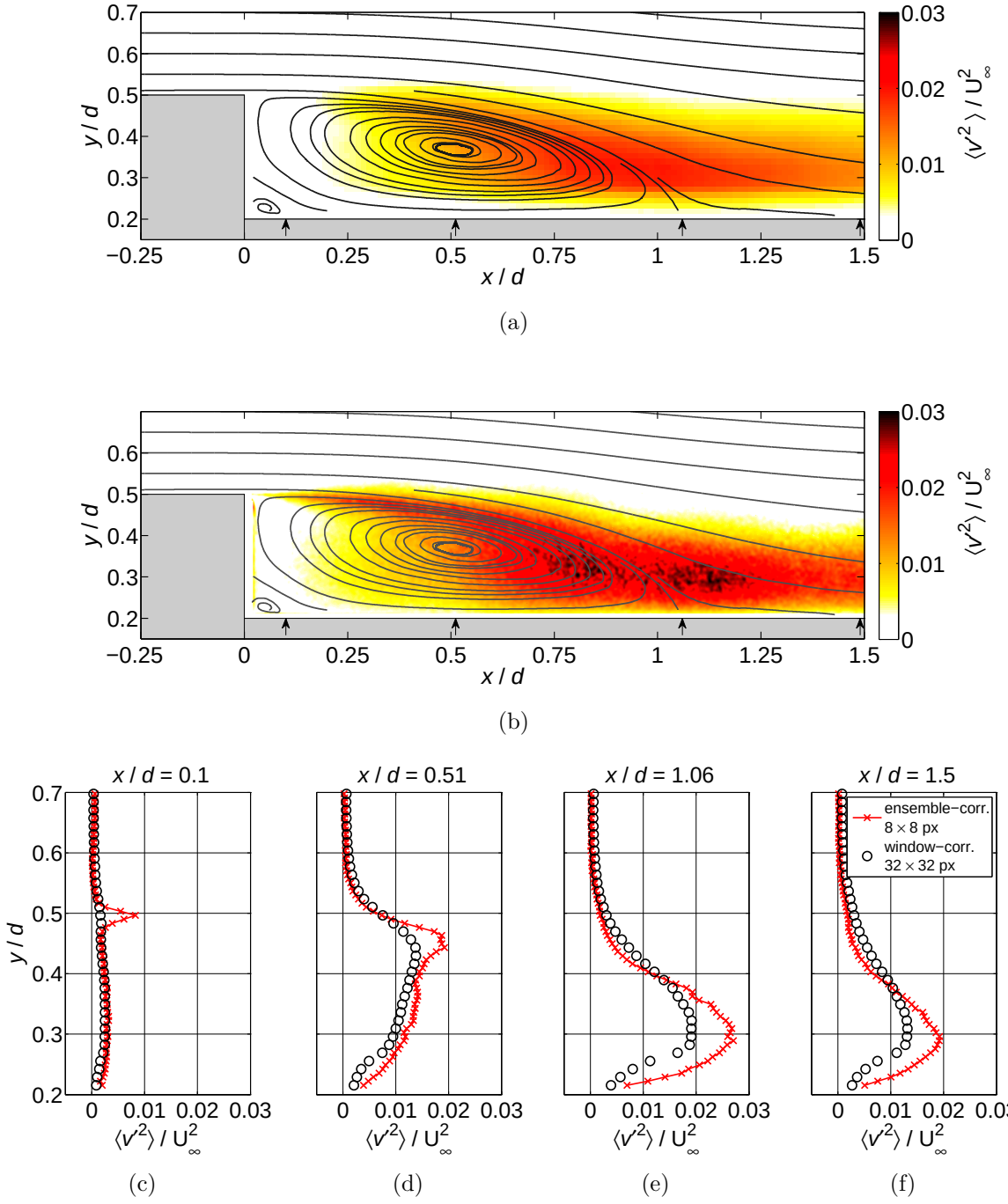

(a) (b) (c) (d) (e) (f)

Figure 5.7: Distribution of the Reynolds normal stresses in the radial direction estimated from 21,500 window-correlation vector fields with a final interrogation-window size of 32×32 px with 75% overlap (a) and from the shape of the correlation functions using single-pixel ensemble-correlation averaged over 8×8 px (b) as well as line plots shortly after separation (c), at the center of the primary recirculation region (d), at reattachment (e) and after reattachment (f).

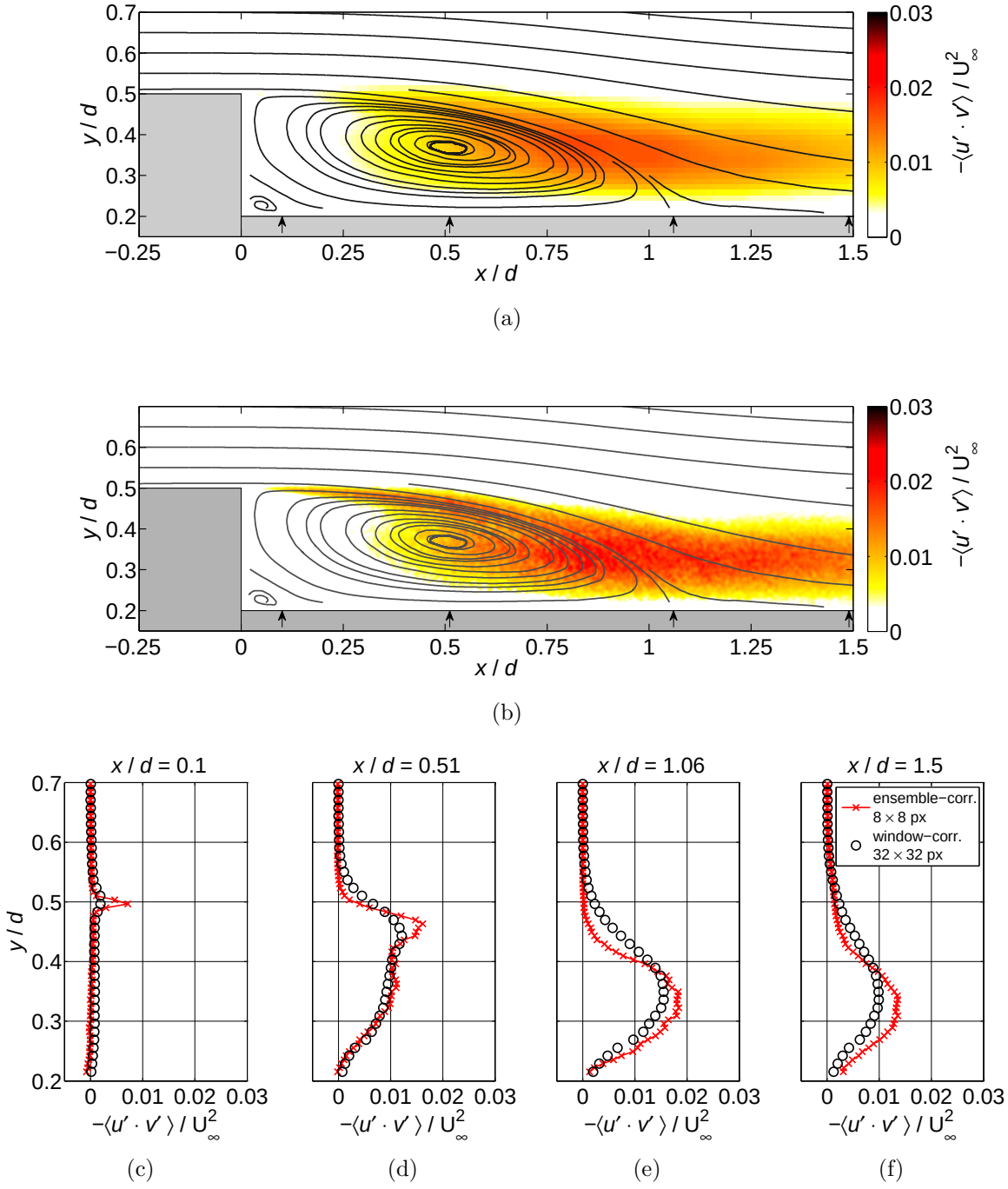

Figure 5.8: Reynolds shear stress distribution estimated from 21,500 window-correlation vector fields with a final interrogation-window size of 32×32 px with 75% overlap (a) and from the shape of the correlation functions using single-pixel ensemble-correlation averaged over 8×8 px (b) as well as line plots shortly after separation (c), at the center of the primary recirculation region (d), at reattachment (e) and after reattachment (f).

Reynolds shear stress $\langle u' \cdot v' \rangle$ is an indicator of the turbulence production in the $xy-$plane and is therefor an important parameter for the validation of modern numerical flow simulations as well as for physical interpretations of the flow.

As before, a significant difference between the intensity of the estimated shear stress with the two methods is observed. Furthermore, the shape of the stress distribution differs: The window-correlation approach is not suited for the detection of the first part of the shear layer (see Fig. 5.8c), indicating that the shear stress here is dominated by small turbulent structures. The maximum position is around $x/d \approx 0.9$ in the case of window-correlation and around $x/d \approx 1.1$ for the single-pixel approach, which includes the effect of small flow structures.

The line plot in Fig. 5.8d shows again two maxima in the case of single-pixel ensemble-correlation function analysis, which correspond to downstream traveling vortices within the shear layer and upstream traveling ones inside the primary recirculation region. The stress estimation based on window-correlation cannot resolve this valley, which indicates the need for the approach applied here. It should also be noted that numerical simulations which are validated based on the classical PIV results would not be able to predict correct results!

Figures 5.8d - 5.8f show a steep slope at the upper border of the shear layer for the sum-of-correlation approach, whereas this border is much smoother for the window-correlation results. Additionally, the absolute value of the shear stress is somewhat larger at the upper border in the case of window-correlation. This fact indicates that the shear stress produced by larger vortices is partly canceled by small ones, which might be due to the different spatial distribution for the different sizes as discussed in Sec. 5.4.1.

The $\langle u' \cdot v' \rangle$ distribution is mainly negative within the separated region. Thus, the shape of the PDF is stretched along the $x-$direction and rotated in the clockwise direction by an angle between 0° and 90°. Furthermore, the negative sign in the turbulence production in boundary layer approximation

$$P = -\langle u'v' \rangle \frac{\partial \langle u \rangle}{\partial y} \tag{5.4}$$

is canceled out for regions with positive gradient and negative shear stress. Figure 5.9 shows the spatial distribution of P. It can be seen, that the largest values for turbulence production are reached within the first part of the shear layer. Further downstream at $x/d \approx 0.5$, two plateaus develop at $y/d \approx 0.35$ and $y/d \approx 0.45$ and a shallow valley is located in between.

5.4 Shear layer vortices

The Reynolds stress distributions (Figs. 5.6 and 5.8) as well as the distribution of the turbulence production (Fig. 5.9) showed a characteristic shape with two plateaus and a

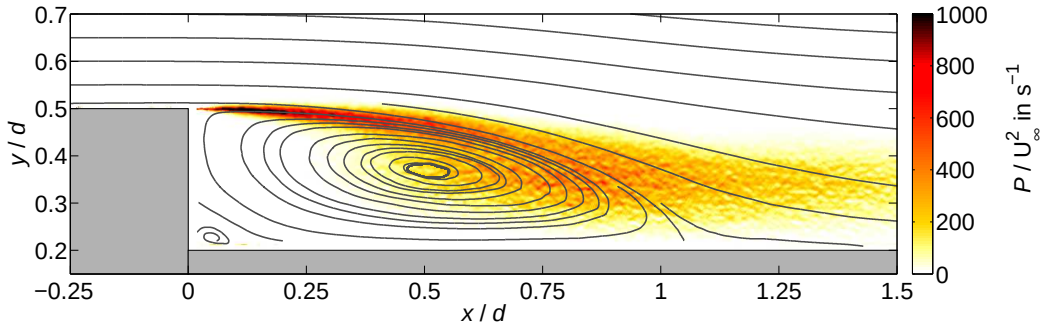

Figure 5.9: Turbulence production computed from the shear stress distribution in Fig. 5.8.

valley in between. This formation cannot be explained using only the statistical properties presented in the previous section. Therefore, the instantaneous velocity fields are now used to detect vortices within the separated region of the axisymmetric backward–facing step flow.

The acquired PIV data set was evaluated with window-correlation by using a standard software (DaVis by LaVision GmbH) in order to analyze instantaneous vector fields. After performing the shift correction and filtering discussed in Sec. 5.2, the shift vectors were computed from interrogation windows with a final size of 32×32 px and an overlap of 75%. Such a large overlap is required in order to detect vortices that are smaller than the interrogation-window size. In a post processing step vectors that differ from their neighbors by more than two times the standard deviation of the neighbors (for each velocity component) were rejected and replaced by interpolated ones. The replacement of spurious vectors is important for a reliable estimation of velocity gradients.

The resulting 21,500 vector fields consist of about $160 \times 50 = 8{,}000$ data points each. Figure 5.10a shows a characteristic instantaneous vector field and the corresponding vorticity ω_z. Every 11^{th} vector in the axial direction and every 2^{nd} one in the radial direction is shown in the figure. The 21,500 individual vector fields were used to detect vortices within the space launcher model's wake as discussed in Chapter 4.

Figure 5.10b shows the swirling strength distribution of the vector field from Fig. 5.10a computed from Eq. (4.5). The swirling strength was locally approximated by a Gaussian with elliptical cross section using Eq. 4.6 on page 85. Where L_1 and L_2 are the major and minor axis length and γ is the angle of orientation. Assuming a round cross section of the vortex tubes, it is possible to determine its orientation with respect to the measurement plan from the ration L_2/L_1, as discussed in Sec. 4.4. The detected vortices are marked by ellipses. It should be emphasized again that the swirling strength is multiplied with the sign of the vorticity to detect the rotation direction.

Approximately 350,000 vortices were detected in 21,500 vector fields. Their position, size (minor and major axis), and orientation was stored together with the swirling strength at the center of the ellipses. The spatial distribution of these quantities will be analyzed in

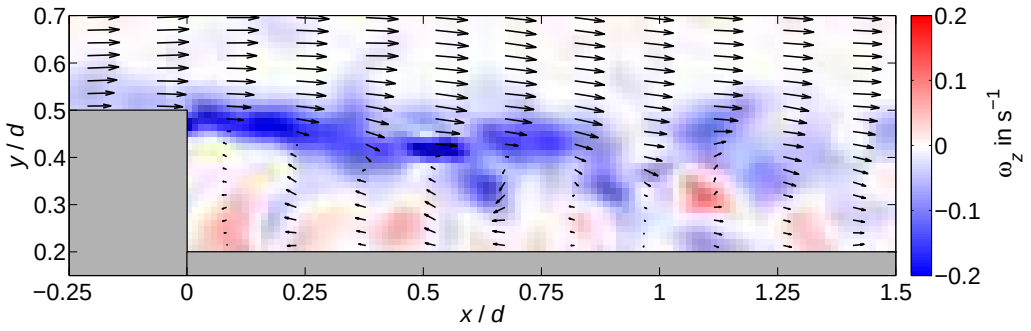

(a)

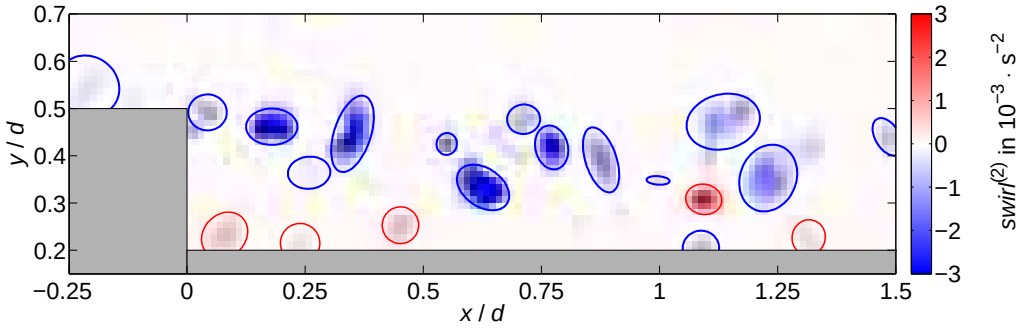

(b)

Figure 5.10: Characteristic instantaneous vector field of a generic space launcher model's wake and its vorticity (a) as well as the swirling distribution and detected vortices (b) at $\mathrm{Ma} = 0.7$ and $\mathrm{Re_d} = 1.1 \cdot 10^6$.

detail in the following sections.

5.4.1 Vortex size

Figure 5.11a shows a histogram of the major axis length L_1 of the 350,000 detected vortices' cross sections. Since the interrogation windows for the final evaluation step were 32×32 px in size and overlapped by 75%, the resulting vector field grid spacing is 8×8 px corresponding to $0.72\,\mathrm{mm} \times 0.72\,\mathrm{mm}$ or $0.013 \cdot d \times 0.013 \cdot d$. On the other hand, due to spurious vectors at least two neighboring vectors in each direction are required to reliably detect a vortex from experimental data. Thus, only vortices larger than two times the grid spacing $= 0.026 \cdot d$ could be reliably detected. Furthermore, due to the spatial filtering of window-correlation based evaluation and due to seeding inhomogeneities it is likely that only a certain fraction of the small vortices is detected. On the other hand, the detection of larger vortices should not be affected as strongly, as long as their size is significantly larger than the interrogation window size and their swirling strength is large enough to be

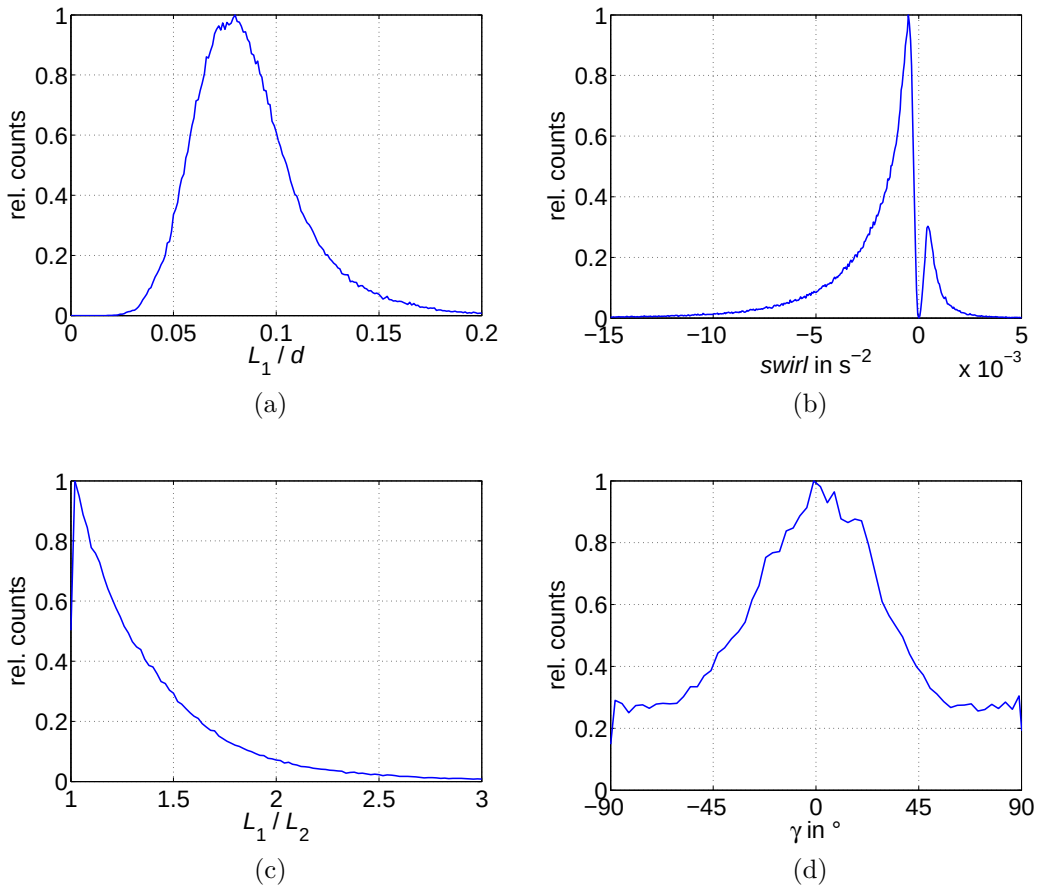

Figure 5.11: Histogram of the vortex size (a), swirling strength (b), aspect ration (c), and orientation of the detected vortices.

distinguished from measurement noise.

Regarding Fig. 5.11a, most of the detected vortices have a size of around $0.08 \cdot d$. Due to the limited detectability of smaller vortices, as discussed above, it is likely that the true maximum is at a smaller size. However, this result allows to estimate the size of the dominant large scale vortices whose dynamic affects the topology of the separated region. The number of detected vortices with $L_1/d > 0.08$ decreases rapidly : it drops to 50% for core diameters of $L_1/d = 0.11$ and to 5% for core diameters of $L_1/d = 0.17$, as shown in Fig. 5.11a.

In order to identify the spatial distribution of the detected vortices, Fig. 5.12 illustrates where the vortices were detected. The field of view was divided into 160×50 boxes and the amount of vortex centers per box is color coded in the figure. The three sub-figures show the distribution for different vortex sizes: For Fig. 5.12a only vortices with a major axis length smaller than $0.06 \cdot d$ were considered. The results in Fig. 5.12a show that the small vortices are generated in the shear layer starting at the point of separation on the base of the main model and that they are convect downstream to the reattachment region. The maximum in the vertical direction is within the recirculation region, below the dividing stream line (dashed line). For $0.5 < x/d < 1$. At can be seen in the figure, that at $x/d = 0.75$ the number of vortices (sum over all y-locations) is larger than those of $x/d = 0.5$. Thus, new small vortices are generated in the shear layer downstream from separation. The distribution in $y-$direction is fairly narrow right after separation and broadens further downstream indicating that the shear layer is fluctuating. Only very few small vortices can be found in the upstream half of the recirculation region. The number of small vortices decreases rapidly downstream of reattachment. This is due to the fact that the shear layer vortices, which were generated further upstream, have grown in size and only few small vortices are generated further downstream.

Figure 5.12b shows the distribution of vortices with a size of $L_1 = (0.08 \pm 0.02) \cdot d$. Most of the vortex centers are located within the first part of the shear layer at $x/d < 0.4$, the distribution broadens further downstream. In contrast to the small vortices, some of the medium sized ones also penetrate into the upstream half of the recirculation region. The maximum in vertical direction is close the dividing stream line until $x/d \approx 0.9$.

The distribution of the large vortices is illustrated in Fig. 5.12c. The smaller vortices generated at the beginning of the shear layer grow in size while they are traveling downstream. This can be seen from the fact that the maximum is shifted to $x/d \approx 0.3$ in contrast to that of the smaller vortices. Additionally, Fig. 5.12c shows a significant signal within the recirculation region, which was not observed for smaller vortices.

The prediction of Bradshaw and Wong (1972), that large vortices are torn into two at reattachment, cannot be confirmed: Large vortices can be found within the recirculation region as well as downstream of reattachment, whereas the density of smaller vortices decreases in these regions. Thus, it can be concluded that the large vortices split up in the region where the dividing streamline becomes strongly curved. Some vortices are fed into the recirculation region while the others are transported further downstream. Most of

the upstream traveling vortices stay close to the model's rear sting, they can hardly be found in a region just below the shear layer. In this region ($0 < x/d < 0.4$, $y/d \approx 0.4$) a distinct valley of the probability to detect vortices is formed.

5.4.2 Swirling strength

Figure 5.11b on page 107 shows a histogram of the swirling strength *swirl* of the 350,000 detected vortices. A large majority of the vortices has a negative swirling strength, which corresponds to a clockwise rotation direction. This was expected from the model's geometry and the flow direction. The histogram shows two distinct maxima at $swirl = -5 \cdot 10^{-4}\,\mathrm{s}^{-2}$ and $swirl = +5 \cdot 10^{-4}\,\mathrm{s}^{-2}$ and a strong decay for larger swirling strength of both signs. According to the findings in Chapter (4), vortices with a size comparable to the interrogation window or smaller are artificially weakened in their swirling strength due to the spatially low-pass filtering of window-correlation based evaluation. Thus, the true position of the two maxima is likely to be further away from zero.

The minimum at $swirl = 0$ is due to the detection limit of vortices: The computed velocity vectors always have a certain uncertainty, which also affects the swirling strength (due to error propagation). If the swirling strength of a vortex is smaller than its uncertainty level, these vortex can not be detected reliable. The minimum detectable swirling strength was $swirl = \pm 3 \cdot 10^{-5}\,\mathrm{s}^{-2}$for the evaluated vector fields.

The spatial distribution of the detected vortices depending on the swirling strength is illustrated in Fig. 5.13. Figure 5.13a and 5.13b show clockwise rotating vortices with strong and weak swirling strength, respectively. The distribution of the counter-clockwise vortices is shown in Fig. 5.13c. It can be seen that the strongest clockwise rotating vortices ($swirl < -0.003\,\mathrm{s}^{-2}$) are concentrated in the first part of the shear layer. These vortices grow in size while following the shear layer. Although their total circulation remains constant, the swirling strength decreases for the larger vortices. Only very few vortices with $swirl < -0.003\,\mathrm{s}^{-2}$ can be found close to the rear sting, in the inner part of the recirculation region, or downstream of reattachment.

The weaker clockwise rotating vortices with $-0.003\,\mathrm{s}^{-2} \leq swirl \leq 0$ (shown in Fig. 5.13b) are generated directly after the point of separation. Thereafter, their swirling strength is amplified leading to a maximum in the distribution of the stronger vortices at $x/d \approx 0.3$ (Fig. 5.13a). However, most of the detected vortices remain at a rather weak clockwise rotation. Figure 5.13b shows an almost homogeneous distribution an a region close to the model's rear sting for $0.25 \leq x/d \leq 1.5$.

As observed for the Reynolds stresses, a valley is formed at $y/d \approx 0.4$ between the center of the recirculation region and the shear layer where only very few vortices were detected. This reduced probability in the vortex distribution is the source of the characteristic shape of the Reynolds stresses in Sec. 5.3.

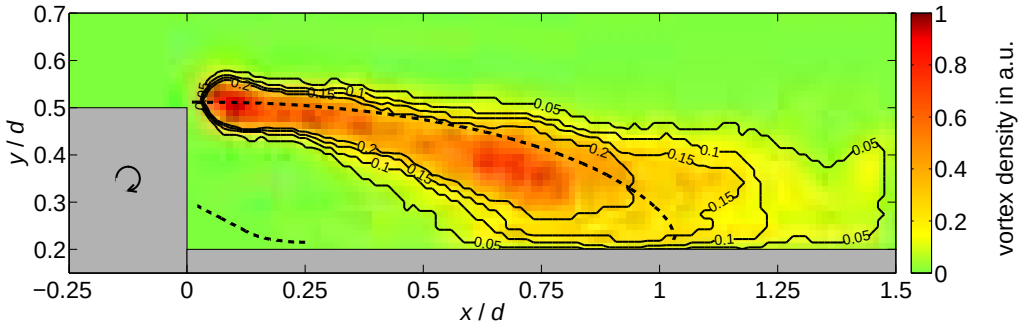

(a) $L_1 < 0.06 \cdot d$

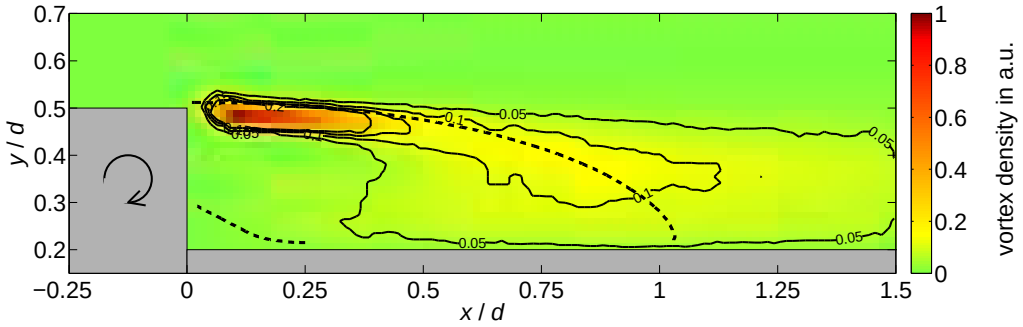

(b) $0.06 \cdot d \leq L_1 \leq 0.10 \cdot d$

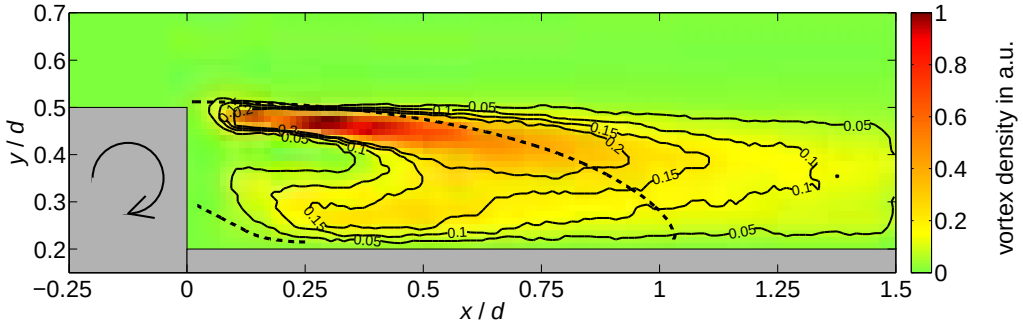

(c) $L_1 > 0.10 \cdot d$

Figure 5.12: Relative number of detected vortices per area for small (a), intermediate (b), and large (c) vortices.

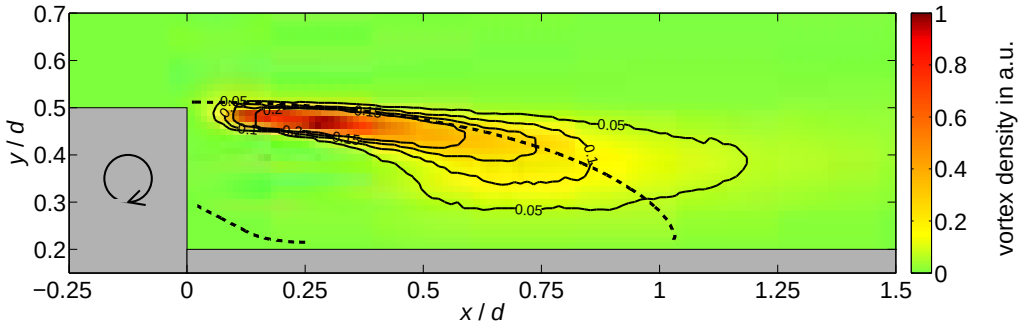

(a) $swirl < -0.003\,\mathrm{s}^{-2}$

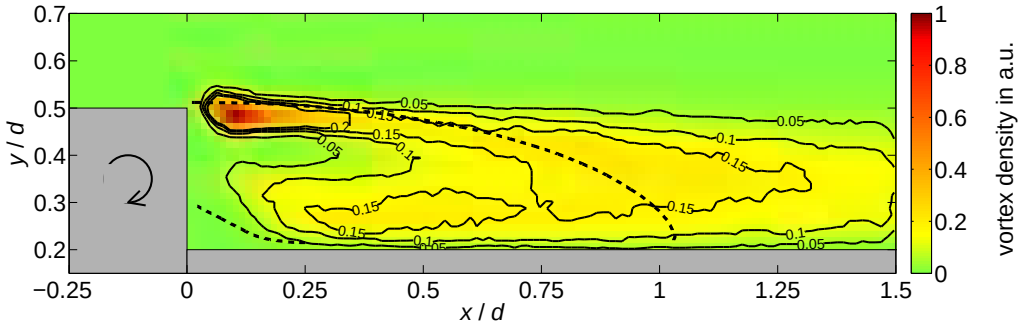

(b) $-0.003\,\mathrm{s}^{-2} \leq swirl \leq 0$

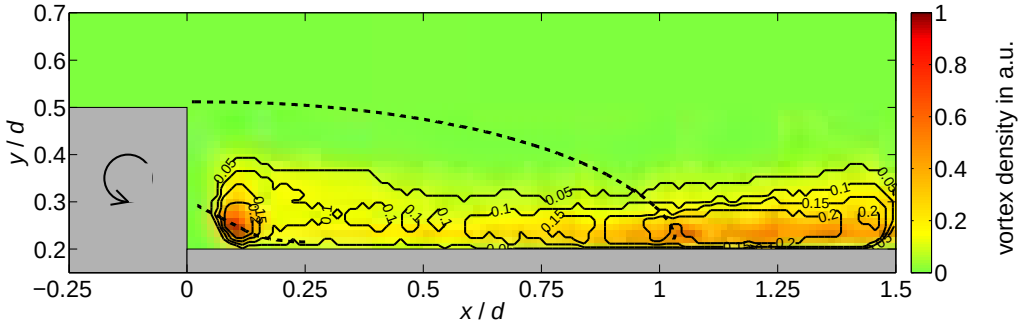

(c) $swirl > 0$

Figure 5.13: Relative number of detected vortices per area for strong (a) and weak (b) clockwise rotation and for counter-clockwise rotation (c).

Figure 5.13c shows the distribution of the counter-clockwise rotating vortices. These vortices are not generated from the separation at the and of the cylindrical main body, but they are generated from the clockwise rotating vortices. The counter-clockwise rotating vortices are concentrated in a region close to the rear sting of the model at $y/d \approx 0.25$ and can rarely be found elsewhere. Scarano et al (1999) also detected counter-rotating vortices further away from the wall in a $2D$ backward facing step flow. These vortices were fairly small and could probably not be detected with the chosen setup. A local maximum of counter-rotating vortices exists close to the base at $x/d \approx 0.1$, where the dividing streamline between recirculation region and re-recirculation region is located (dashed line).

5.4.3 Vortex orientation

Most detected vortices appear nearly round, however, some are stretched indicating that the vortex tubes cut the measurement plane under a certain angle, as discussed in Chapter 4 (compare Fig. 5.10b on page 106). Figure 5.11c shows a histogram of the ratio of the major and minor axis of the detected ellipses. The histogram of the orientation of the detected ellipses is shown in Fig. 5.11d. A rotation of 0° and ±90° correspond to stretching in axial and radial direction, respectively.

The spatial distribution of the detected vortices depending on the aspect ratio L_1/L_2 is illustrated in Fig. 5.14. While the round vortices ($L_1/L_2 < 1.3$) are concentrated in the first part of the shear layer, the stretched ones (Figs. 5.14b and 5.14c) have their maximum further downstream and are more equally distributed. This leads to the conclusion that the axis of vortex tubes generated at the main body's rear end is tilted towards the measurement plan while traveling downstream.

Figure 5.15 illustrates the spatial distribution for different orientations of the vortex ellipses. Only vortices with an aspect ratio of $L_1/L_2 > 1.5$ were considered here. Vortices with their major axis aligned along the $x-$axis are shown in Fig. 5.15b. They are generated in the shear layer shortly after separation, have a maximum at $x/d \approx 0.3$ and can be found within the recirculation region as well as downstream of reattachment. The distribution for the downward pointing vortex tube cross sections (shown in Fig. 5.15a) is similar to that with horizontal orientation. The main difference is that the maximum is shifted downstream to $x/d \approx 0.35$. On the other hand, the distribution of upwards pointing vortex tubes differs significantly from the other two: These vortices do not reach the region close to the model's rear sting. Furthermore, upward pointing vortex tubes can only rarely be found for $x/d > 1.25$.

The analysis oft the shape and the orientation of the vortices lead to the conclusion that the investigated transonic wake flow is strongly three-dimensional: A significant fraction of vortex tubes cuts the measurement plane under an acute angle. While the vortex tubes are traveling downstream, their axis is further tilted towards the measurement plane and towards the axis of symmetry. This three dimensional behavior was also detected in zonal

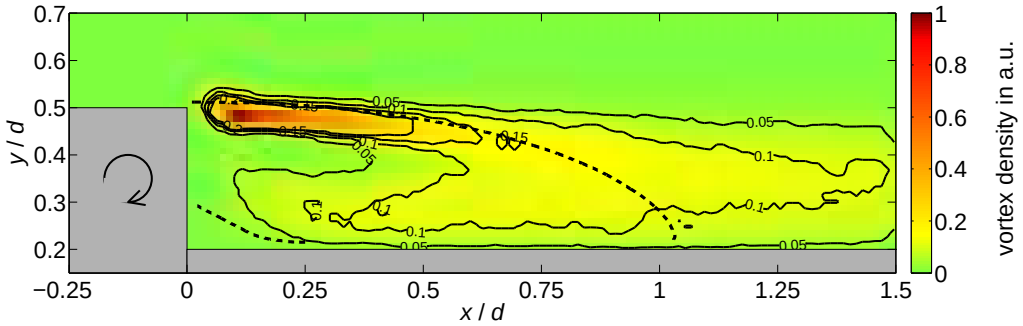

(a) $L_1/L_2 < 1.3$

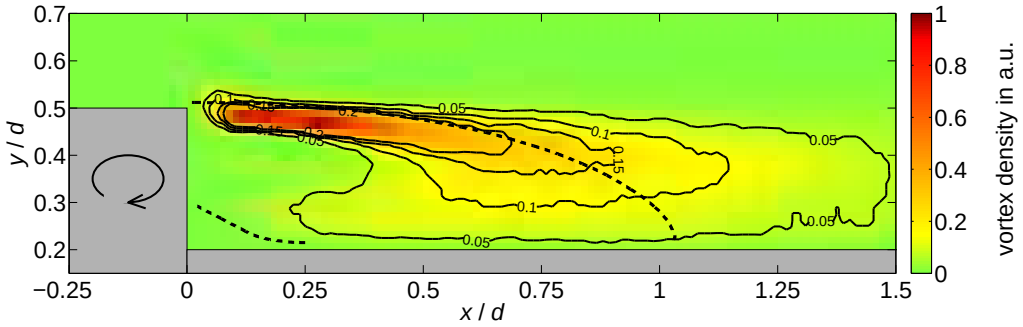

(b) $1.3 \leq L_1/L_2 \leq 2.0$

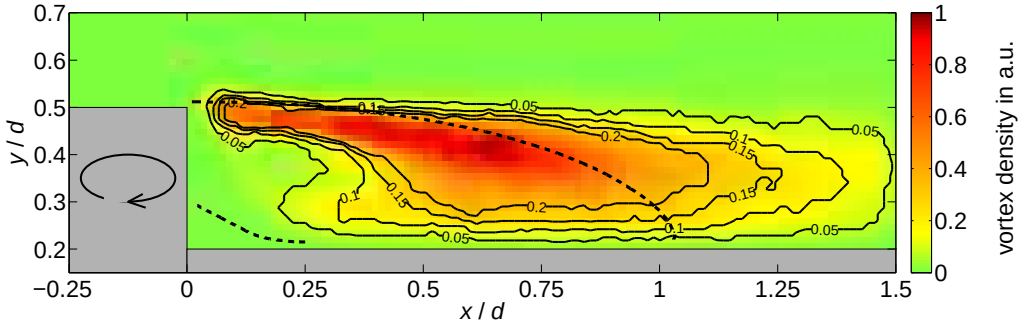

(c) $L_1/L_2 > 2$

Figure 5.14: Relative number of detected vortices per area for round (a), slightly stretched (b) and significantly stretched swirling cross sections (c).

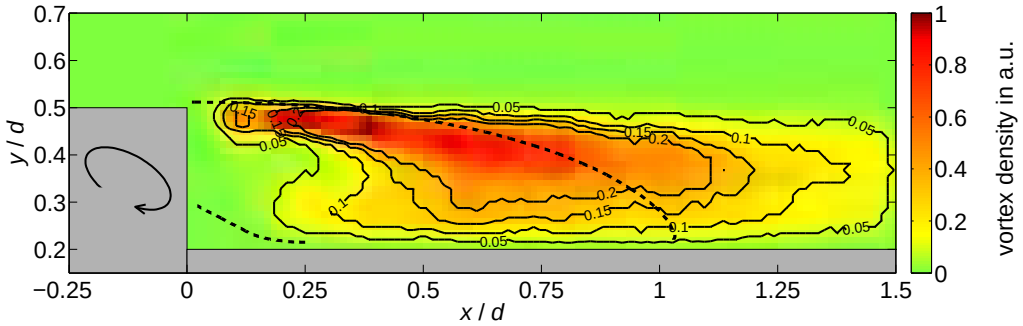

(a) $\gamma < -20°$

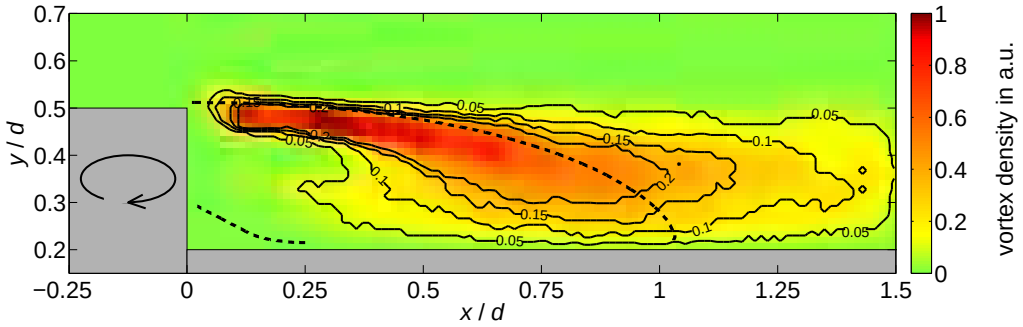

(b) $-20 \leq \gamma \leq 20$

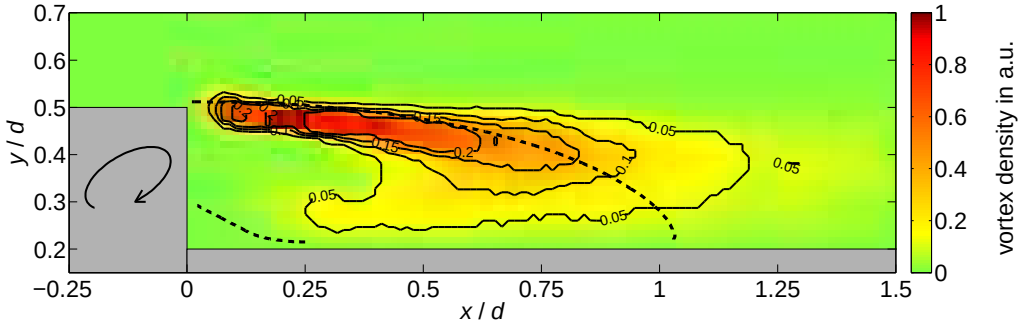

(c) $\gamma > 20$

Figure 5.15: Relative number of detected vortices per area for downwards (a), stream wise (b) and upwards pointing stretched swirling cross sections (c).

detached eddy simulations by Deck et al (2007) for a similar geometry and similar flow conditions.

5.4.4 Coherent structures

So far the vortices were treated as individual structures. A remaining issue is to identify the connection between individual vortices. In order to fully follow the turbulent structures in a time series of velocity fields, PIV measurements with a repetition rate in the order of 100 kHz would be required, which are not yet available. Thus, the connection can only be analyzed in a statistical way. The two-point correlation was shown to be well suited to identify the size and shape of coherent structures (Liu et al, 2001; Nakagawa and Hanratty, 2001; Ganapathisubramani et al, 2005). For the velocity component u_i, the two-point correlation is defined as follows:

$$R\left(x_0,y_0,x,y\right) = \frac{\sum_{n=1}^{N}\left[u_\mathrm{i,n}\left(x_0,y_0\right) - \left\langle u_\mathrm{i}\left(x_0,y_0\right)\right\rangle\right]\left[u_\mathrm{i,n}\left(x,y\right) - \left\langle u_\mathrm{i}\left(x,y\right)\right\rangle\right]}{\sigma u_\mathrm{i}\left(x_0,y_0\right)\sigma u_\mathrm{i}\left(x,y\right)} \tag{5.5}$$

Where N is the total number of vector fields, n is the corresponding control variable and $\langle u_\mathrm{i}\rangle$ is the average velocity component. An ensemble of PIV vector fields allows for the correlation of the point of interest (x_0,y_0) with all points within the field of view (x,y).

Figure 5.16 shows the spatial distribution of the two-point correlation coefficient of the axial R_uu and radial velocity component R_vv for different characteristic locations. It can be seen from R_uu (left in Fig. 5.16) that large coherent structures develop in the separated region. The shape of the structures reveals a direct connection between both sides of the dividing stream line, leading to the conclusion that the shear layer vortices are generated more or less periodically and that vortices inside and outside the recirculation region are coherent with each other.

Figure 5.17 shows the spatial distribution of the size of the correlation function R_uu from Fig. 5.16. The largest extension at a height of 1/e is color coded. The incoming boundary layer is characterized by coherent structures larger than 0.3 times the model diameter, which is equal to the step height. The size of these structures decreases significantly downstream of separation, due to the mixing with the highly turbulent recirculation region. Coherent structures that fill most of the primary recirculation region can be found in its center. Since the coherence length is much larger than the size of the detected vortices, the coherence is caused by periodic vortex shedding or by large vortices that are too weak to be detected from the PIV velocity fields.

In the right part of Fig. 5.16, the two-point correlation of the vertical velocity component R_vv is illustrated. The negative correlation next to the maximum indicates vortices with their center axis aligned perpendicular to the measurement plane: The vertical velocity component in the upstream and downstream part of a vortex are of opposite sign, which causes a negative correlation coefficient. Additionally, the correlation with the previous and the following vortex can be seen from the neighboring extrema in the $R_\mathrm{vv}-$distribution.

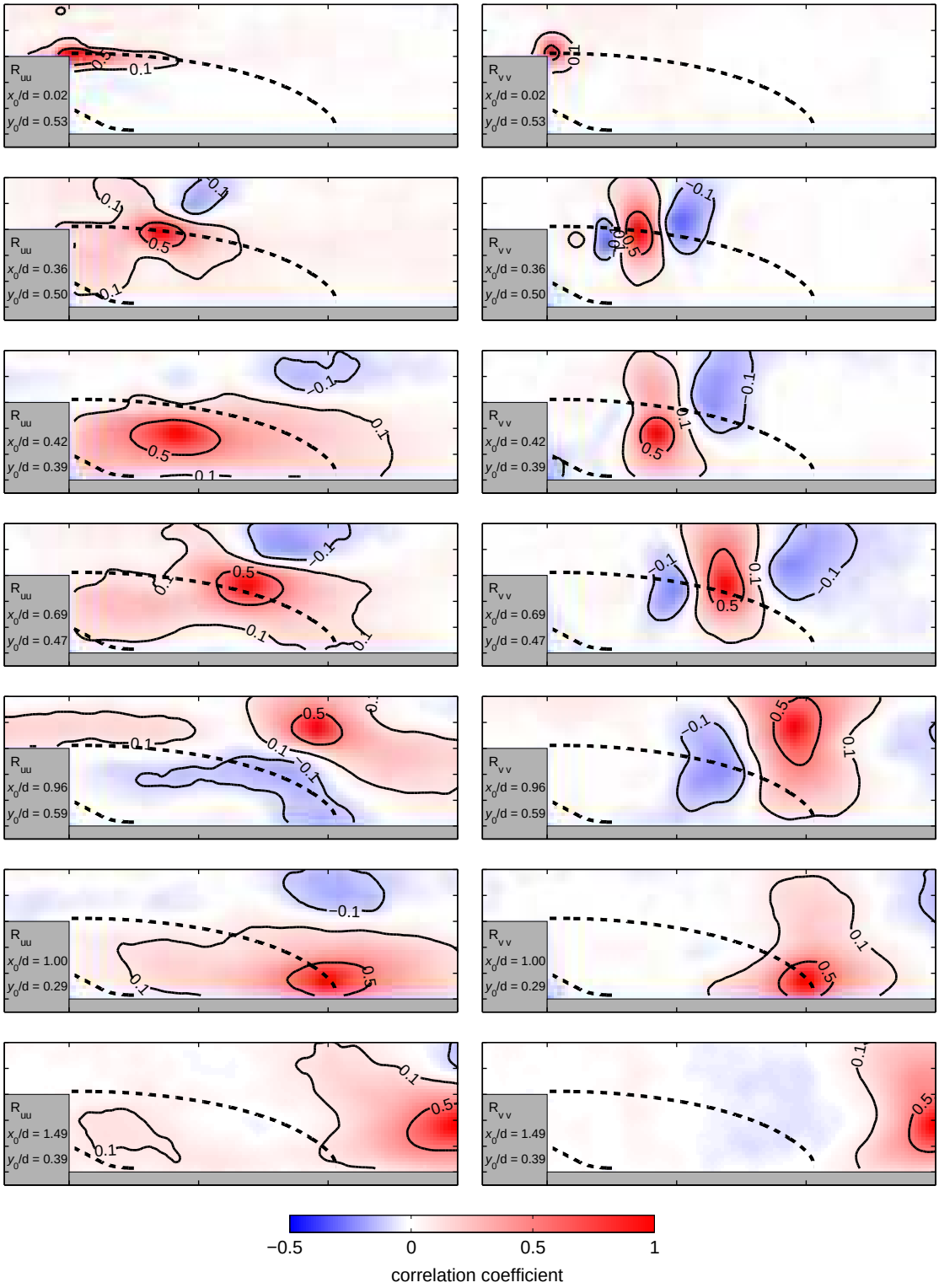

Figure 5.16: Two-point correlation of the axial (left) and radial (right) velocity component for different locations. Dividing streamlines of the primary and secondary recirculation regions are indicated by dashed lines. See Fig. 5.17 for scaling.

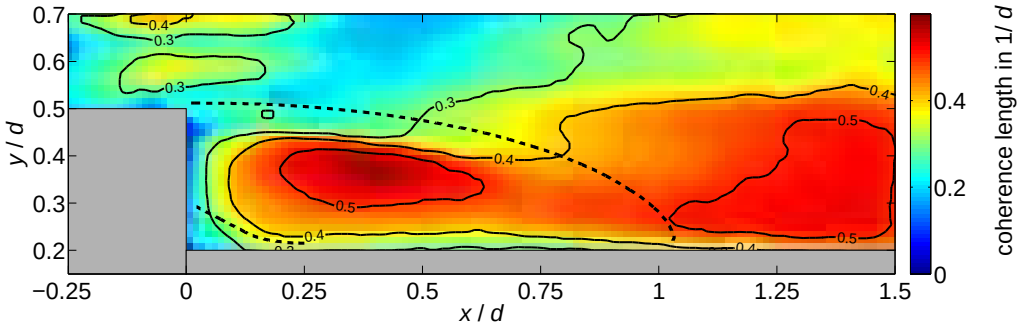

Figure 5.17: Spatial distribution of the coherence length: largest extension of the R_{uu} correlation function at a height of 1/e. Dividing streamlines of the primary and secondary recirculation regions are indicated by dashed lines.

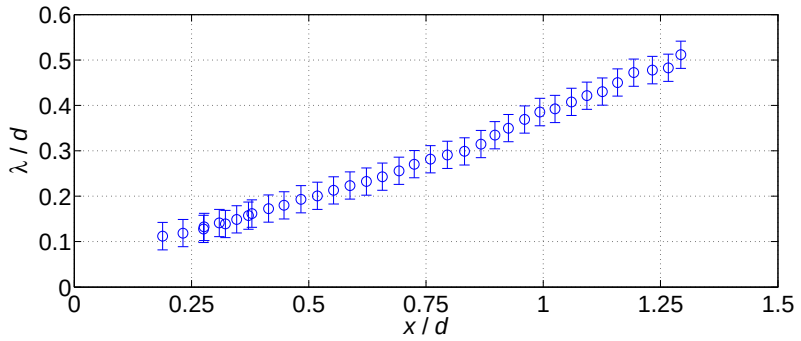

Figure 5.18: Separation between neighboring coherent structures estimated from the distance between minimum and maximum of R_{vv} from Fig. 5.16.

The distance between neighboring minimum and maximum in R_{vv} grows with increasing distance from the model's base. Figure 5.18 shows this distance with respect to the horizontal position x/d for shear layer vortices at $y/d = 0.5$. Where λ is the distance between the maximum and the minimum and the corresponding $x-$location in 5.18 is the mean between the center position of both extrema. The distance 2λ is the mean separation of two coherent vortices, which increases nearly linearly with x, as can be seen from the figure. From this it can be concluded that vortices in the shear layer grow in size and are accelerated while traveling downstream.

Conclusions

A generic space launcher model's wake was investigated experimentally at Ma = 0.7 and $\mathrm{Re_d} = 1.1 \cdot 10^6$ by means of high repetition rate PIV. The evaluation of 21,500 PIV image pairs, 1280 × 400 px in size, with single-pixel ensemble-correlation allows for a

very large dynamic spatial range and high accuracy. Approximately $640 \times 200 = 128{,}000$ independent mean velocity vectors were computed with a spatial resolution better than $180\,\mu m$ $(= 0.003 \cdot d)$.

It was shown that the mean flow field features a recirculation region that extents more than one model diameter in axial direction. The shear layer reattaches on the model's rear sting at $x/d = 1.06 \pm 0.03$. Additionally, the high resolution approach resolved a secondary recirculation region. The location of characteristic points in the flow field was determined with high accuracy.

The acquired data set also allowed for the determination of 21,500 instantaneous velocity vector fields with $160 \times 50 = 8{,}000$ data points and a spatial resolution of $\approx 3\,mm$ $(= 0.05 \cdot d)$. From the swirling strength of this vector fields more than 350,000 vortices were detected. The implemented method is capable of detecting the vortices and of identifying their size, shape and position. Furthermore, fitting ellipses to the swirling distribution allows for the estimation of the vortex tube's orientation with respect to the measurement plane.

It is evident that small vortices, which are generated at the point of separation, grow in size while traveling along the shear layer. A significant fraction of the larger vortices penetrates into the primary recirculation area, while smaller ones have a lower probability to be found in this region. Thus, it can be concluded that the vortices either penetrate into the recirculation region or they travel further downstream. A splitting of large vortices in the reattachment region, as suggested by Bradshaw and Wong (1972), cannot be confirmed. However, it should be kept in mind that only a small fraction of the vortices are detected due to the limited resolution of the instantaneous velocity fields.

The vortices in the separated flow of the space launcher model's wake cause an increase in the velocity fluctuations and thus in the Reynolds stress level. The combination of two approaches for the estimation of the Reynolds normal and shear stresses revealed the contribution of turbulent structures with respect to their size. Standard window-correlation computes spatially low-pass filtered vector fields, from which the contribution of large scale vortices for the Reynolds stresses is estimated. On the other hand, the analysis of single-pixel ensemble-correlation functions allows for the direct determination of the velocity's PDF, which also includes velocity fluctuations from vortices that are smaller than the pixel grid spacing. Furthermore, this approach results in significantly improved spatial resolution.

The use of both methods revealed the significance of small scale structures for the Reynolds stress distribution in the space launcher model's wake. It was found that the first part of the shear layer is dominated by small structures, which cause a significantly different shaped stress distributions. A distinct valley in the stress distributions was found between the shear layer and the primary recirculation region. This valley is related to a decreased vortex detection probability between the shear layer and the recirculation region.

For the first time, the full spectrum of turbulence was used to determine the Reynolds stress distributions of a generic space launcher model's wake at a transonic Mach number.

This is very important for the validation of new numerical methods as well as for the fundamental understanding of the flow physics.

Two-point correlation of the in-plane velocity components revealed large coherent structures in the recirculation region. A periodic generation of shear layer vortices was found, which is the source of buffeting. In the case of a space launcher wake, the periodic vortex shedding causes strong mechanical loads for the main engine's nozzle.

Nomenclature

All relevant symbols and abbreviations used in this thesis are summarized in the following:

Symbols

Symbol	Unit	Quantity
A	counts	First PIV image's intensity distribution
B	counts	Second PIV image's intensity distribution
C	counts	Correlation function
C_X	px	Correlation function major axis length
C_Y	px	Correlation function minor axis length
d_p	m	Particle diameter
d_τ	m	Particle image diameter
D	px	Digital particle image diameter at I_0/e^2
D_a	m	Lens aperture diameter
$f_\#$	m/m	F-number
$I\,(X,Y)$	counts	Particle image intensity distribution
I_0	counts	Maximum particle image intensity
L	px	Discrete sensor size
M	m/m	Optical magnification
p_t	bar	Total pressure
p_x	m/s	PDF major axis on measurement plane
p_y	m/s	PDF minor axis on measurement plane
P_X	px	PDF major axis on image plane
P_Y	px	PDF minor axis on image plane
R	counts	Auto-correlation function
s_0	m	Object distance
S	µm/px	Sensor pixel-grid spacing
SRW	px	Step response width
t_p	ns	Laser pulse duration
u,v	m/s	Velocity components on measurement plane
u_τ	m/s	Friction velocity
W_Y	px	Interrogation window height
x,y	m	Coordinates on measurement plane

Symbol	Unit	Quantity
A	counts	First PIV image's intensity distribution
B	counts	Second PIV image's intensity distribution
C	counts	Correlation function
X,Y	px	Coordinates on image plane
Y^*,y^*	px, mm	Wall-normal image coordinates
z	m	Distance from focal plane
α	rad	PDF ellipsis orientation
φ	rad	Correlation function ellipsis orientation
Δt	µs	Toime separation between Laser pulses
ΔX,ΔY	px	Shift vector components
ΔX^*	px	Wall-parallel shift vector component
ΔY^*	px	Wall-normal shift vector component
λ	nm	Wave length
ρ	kg/m^3	Mass density
σ_n	counts	Image noise standard deviation
τ_w	N/m^2	Wall-shear stress
ξ,ψ	px	Coordinates on correlation plane

Abbreviations

AWM	Atmospheric Wind tunnel Munich
CCD	Charge-Coupled Device
CMOS	Complementary Metal Oxide Semiconductor
DNS	Direct Numerical Simulation
DEHS	Di-Ethyl-Hexyl-Sebacat
DSR	Dynamic Spatial Range
FFT	Fast Fourier Transformation
FOV	Field Of View
LES	Large Eddy Simulation
Ma	Mach number
MTF	Modular Transfer Function
$\mathrm{N_{ppp}}$	Number of Particles Per Pixel
PDF	Probability Density Function
PIV	Particle Image Velocimetry
PTV	Particle Tracking Velocimetry
px	Pixel
RANS	Reynolds Averaged Navier-Stokes Simulation
Re	Reynolds number
RMS	Root Mean Square

sCMOS	Scientific CMOS
SNR	Signal to noise ratio
TWM	Trisonic Wind Tunnel Munich
Θ	Heaviside step function

Bibliography

Adrian RJ (1991) Particle-imaging techniques for experimental fluid mechanics. Annu Rev Fluid Mech 23:261–304, URL http://dx.doi.org/10.1146/annurev.fl.23.010191.001401

Adrian RJ (1997) Dynamic ranges of velocity and spatial resolution of particle image velocimetry. Meas Sci Tech 8:1393, URL http://dx.doi.org/10.1088/0957-0233/8/12/003

Adrian RJ, Westerweel J (2010) Particle Image Velocimetry. Cambridge University Press

Adrian RJ, Christensen KT, Liu Z (2000) Analysis and interpretation of instantaneous turbulent velocity fields. Exp Fluids 29:275–290, URL http://dx.doi.org/10.1007/s003489900087

Alfredsson PH, Örlü R, Schlatter P (2011) The viscous sublayer revisited exploiting self-similarity to determine the wall position and friction velocity. Exp Fluids 51:271–280, URL http://dx.doi.org/10.1007/s00348-011-1048-8

Arnold W, Hinsch KD, Mach D (1986) Turbulence level measurement by speckle velocimetry. Appl Optics 25:330–331, URL http://dx.doi.org/10.1364/AO.25.000330

Astarita T (2007) Analysis of weighting windows for image deformation methods in piv. Exp Fluids 43:859–872, URL http://dx.doi.org/10.1007/s00348-007-0314-2

Billy F, David L, Pineau G (2004) Single pixel resolution correlation applied to unsteady flow measurements. Meas Sci Tech 15:1039–1045, URL http://dx.doi.org/10.1088/0957-0233/15/6/002

Bitter M, Scharnowski S, Hain R, Kähler CJ (2011) High-repetition-rate PIV investigations on a generic rocket model in sub- and supersonic flows. Exp Fluids 50:1019–1030, URL http://dx.doi.org/10.1007/s00348-010-0988-8

Bitter M, Hara T, Hain R, Yorita D, Asai K, Kähler C (2012) Characterization of pressure dynamics in an axisymmetric separating/reattaching flow using fast-responding pressure-sensitive paint. Exp Fluids 53:1737–1749, URL http://dx.doi.org/10.1007/s00348-012-1380-7

Born M, Wolf E (2000) Principles of Optics. Cambridge University Press

Bradshaw P, Wong FYF (1972) The reattachment and relaxation of a turbulent shear layer. J Fluid Mech 52:113–135, URL http://dx.doi.org/10.1017/S002211207200299X

Canuto V (2009) Compressible turbulence. Astrophys J 482:827, URL http://dx.doi.org/10.1086/304175

Chamarthy P, Garimella SV, Wereley ST (2009) Non-intrusive temperature measurement using microscale visualization techniques. Exp Fluids 47:159–170, URL http://dx.doi.org/10.1007/s00348-009-0646-1

Chandrasuda C (1975) A reattaching turbulent shear layer in incompressible flow. PhD thesis, Imperial College London (University of London)

Chesnakas C, Dancey C (1990) Three-component lda measurements in an axial-flow compressor. J Propul Power 6:474–481, URL http://dx.doi.org/10.2514/3.25459

Chong MS, Perry AE, Cantwell BJ (1990) A general classification of three-dimensional flow fields. Phys Fluids 2:765–777, URL http://dx.doi.org/10.1063/1.857730

Christensen K (2004) The influence of peak-locking errors on turbulence statistics computed from PIV ensembles. Exp Fluids 36:484–497, URL http://dx.doi.org/10.1007/s00348-003-0754-2

Cierpka C, Weier T, Gerbeth G (2008) Evolution of vortex structures in an electromagnetically excited separated flow. Exp Fluids 45:943–953, URL http://dx.doi.org/10.1007/s00348-008-0512-6

Clauser FH (1956) The turbulent boundary layer. Adv Appl Mech 4:1–51, URL http://dx.doi.org/10.1016/S0065-2156(08)70370-3

Corrsin S (1947) Extended Applications of the Hot-Wire Anemometer. Rev Sci Instrum 18:469–471, URL http://dx.doi.org/10.1063/1.1740981

Darcy H (1858) Note relative à quelques modifications à introduire dans le tube de Pitot. Annales des Ponts et Chaussées 1:351–359

David C, Radulovic S (2005) Prediction of buffet loads on the ariane 5 afterbody. In: 6th International Symposium on Launcher Technologies, Munich, Germany

Deck S, Thepot R, Thorigny P (2007) Zonal Detached Eddy Simulation of flow induced unsteady side-loads over launcher configurations. In: 2nd European Conference For Aerospace Sciences, Brussels, Belgium

Deprés D, Reijasse P, Dussauge JP (2004) Analysis of Unsteadiness in Afterbody Transonic Flows. AIAA Journal 42:2541–2550, URL http://dx.doi.org/10.2514/1.7000

Deprés D, Radulovic S, Lambare H (2005) Reduction of Unsteady Effects in Afterbody Transonic Flows. In: 6th International Symposium on Launcher Technologies, Munich

Dumitra M, Schanz D, Schröder A, Kähler CJ (2011) Large-scale turbulent boundary layer investigation with multiple camera PIV and hybrid evaluation up to single pixel resolution. In: 9th International Symposium on Particle Image Velocimetry, Kobe, Japan, July 21-23

Eaton JK, Johnston JP (1981) A Review of Research on Subsonic Turbulent Flow Reattachment. AIAA Journal 19:1093–1100, URL http://dx.doi.org/10.2514/3.60048

Elsinga G, Scarano F, Wieneke B, Van Oudheusden B (2006) Tomographic particle image velocimetry. Exp Fluids 41:933–947, URL http://dx.doi.org/10.1007/s00348-006-0212-z

Favre A (1965) The equations of compressible turbulent gases. Tech. rep., DTIC Document

Fernholz HH, Finley PJ (1996) The incompressible zero-pressure-gradient turbulent boundary layer: an assessment of the data. Prog Aerosp Sci 32:245–311, URL http://dx.doi.org/10.1016/0376-0421(95)00007-0

Foreman JW, George EW, Lewis RD (1965) Measurement of Localized Flow Velocities in Gases with a Laser Doppler Flowmeter. Appl Phys Lett 7:77–78, URL http://dx.doi.org/10.1063/1.1754319

Ganapathisubramani B, Clemens NT (2006) Effect of Laser Pulse Duration on Particle Image Velocimetry. AIAA Journal 44:1368–1370, URL http://dx.doi.org/10.2514/1.18404

Ganapathisubramani B, Hutchins N, Hambleton WT, Longmire EK, Marusic I (2005) Investigation of largescale coherence in a turbulent boundary layer using twopoint correlations. J Fluid Mech 524:57–80, URL http://dx.doi.org/10.1017/S0022112004002277

Gülhan A (ed) (2008) RESPACE - Key Technologies for Reusable Space Systems. Springer-Verlag Berlin Heidelberg

Hain R, Kähler CJ (2007) Fundamentals of multiframe particle image velocimetry (PIV). Exp Fluids 42:575–587, URL http://dx.doi.org/10.1007/s00348-007-0266-6

Hain R, Kähler CJ, Tropea C (2007) Comparison of CCD, CMOS and intensified cameras. Exp Fluids 42:403–411, URL http://dx.doi.org/10.1007/s00348-006-0247-1

Hannemann K, Lüdeke H, Pallegoix JF, Ollivier A, Lambaré H, Maseland J, Geurts E, Frey M, Deck S, Schrijer F, Scarano F, Schwane R (2011) Launcher vehicle base buffeting - recent experimental and numerical investigations. In: Proceedings 7th European Symposium on Aerothermodynamics for Space Vehicles , Brugge, Belgium, 9-12 May

Hohreiter V, Wereley ST, Olsen MG, Chung JN (2002) Cross-correlatioin analysis for temperature measurement. Meas Sci Tech 13:1072–1078, URL http://dx.doi.org/10.1088/0957-0233/13/7/314

Huang HT, Fiedler HE (1997) A DPIV study of a starting flow downstream of a backward-facing step. Exp Fluids 23:395–404, URL http://dx.doi.org/10.1007/s003480050127

Hudy LM, Naguib AM, William M Humphreys J (2003) Wall-pressure-array measurements beneath a separating/reattaching flow region. Phys Fluids 15:706–717, URL http://dx.doi.org/10.1063/1.1540633

Hudy LM, Naguib AM, Humphreys WM, Bartram SM (2005) Particle Image Velocimetry Measurements of a Two/Threedimensional Separating/Reattaching Boundary Layer Downstream of an Axisymmetric Backward-facing Step. In: 43rd AIAA Aerospace Sciences Meeting and Exhibit, Reno, NV, United States, 10-13 Jan.

Ishihara T, Gotoh T, Kaneda Y (2009) Study of high-reynolds number isotropic turbulence by direct numerical simulation. Annu Rev Fluid Mech 41:165–180, URL http://dx.doi.org/10.1146/annurev.fluid.010908.165203

Kähler CJ (1997) Ortsaufgelöste Geschwindigkeitsmessungen in einer turbulenten Grenzschicht. DLR-FB:97–32

Kähler CJ (2004) The significance of coherent flow structures for the turbulent mixing in wall-bounded flows. PhD thesis, Georg-August-Universität,Göttingen, URL http://webdoc.sub.gwdg.de/diss/2004/kaehler/kaehler.pdf

Kähler CJ, Kompenhans J (2000) Fundamentals of multiple plane stereo PIV. Exp Fluids 29:70–77, URL http://dx.doi.org/10.1007/s003480070009

Kähler CJ, Scholz U (2006) Transonic jet analysis using long-distance micro PIV. In: 12th International Symposium on Flow Visualization, Göttingen, Germany

Kähler CJ, Sammler B, Kompenhans J (2002) Generation and control of particle size distributions for optical velocity measurement techniques in fluid mechanics. Exp Fluids 33:736–742, URL http://dx.doi.org/10.1007/s00348-002-0492-x

Kähler CJ, Scholz U, Ortmanns J (2006) Wall-shear-stress and near-wall turbulence measurements up to single pixel resolution by means of long-distance micro-PIV. Exp Fluids 41:327–341, URL http://dx.doi.org/10.1007/s00348-006-0167-0

Kähler CJ, Scharnowski S, Cierpka C (2012a) On the resolution limit of digital particle image velocimetry. Exp Fluids 52:1629–1639, URL http://dx.doi.org/10.1007/s00348-012-1280-x

Kähler CJ, Scharnowski S, Cierpka C (2012b) On the uncertainty of digital PIV and PTV near walls. Exp Fluids 52:1641–1656, URL http://dx.doi.org/10.1007/s00348-012-1307-3

Kalitzin G, Medic G, Iaccarino G, Durbin P (2005) Near-wall behavior of rans turbulence models and implications for wall functions. J Comput Phys 204:265–291, URL http://dx.doi.org/10.1016/j.jcp.2004.10.018

Keane RD, Adrian RJ (1990) Optimization of particle image velocimeters. Part I: double pulsed systems. Meas Sci Tech 1:1202–1215, URL http://dx.doi.org/10.1088/0957-0233/1/11/013

King LV (1914) On the Convection of Heat from Small Cylinders in a Stream of Fluid: Determination of the Convection Constants of Small Platinum Wires, with Applications Stream of Fluid: Determination of the Convection. P R Soc London 90:563–570

Kolmogorov AN (1962) A refinement of previous hypotheses concerning the local structure of turbulence in a viscous incompressible fluid at high Reynolds number. J Fluid Mech 13:82–85, URL http://dx.doi.org/10.1017/S0022112062000518

Kundu PK, Cohen IM (2008) Fluid Mechanics, 4th edn. Academic Press

Le H, Moin P, J Kim K (1997) Direct numerical simulation of turbulent flow over a backwardfacing step. J Fluid Mech 330:349–374, URL http://dx.doi.org/10.1017/S0022112096003941

Liao Q, Cowen EA (2005) An efficient anti-aliasing spectral continuous window shifting technique for piv. Exp Fluids 38:197–208, URL http://dx.doi.org/10.1007/s00348-004-0899-7

Liu Y, Daum P (2008) Relationship of refractive index to mass density and self-consistency of mixing rules for multicomponent mixtures like ambient aerosols. J Aerosol Sci 39:974–986, URL http://dx.doi.org/10.1016/j.jaerosci.2008.06.006

Liu Z, R J Adrian RJ, Hanratty TJ (2001) Large-scale modes of turbulent channel flow: transport and structure. J Fluid Mech 448:53–80, URL http://dx.doi.org/10.1017/S0022112001005808

Lüdeke H, Calvo JB, Filimon A (2006) Fluid structure interaction at the Ariane-5 nozzle section by advanced turbulence models. In: European Conference on Computational Fluid Dynamics - ECCOMAS CFD, TU Delft, The Netherlands

Maas H, Gruen A, Papantoniou D (1993) Particle Tracking Velocimetry in 3-Dimensional flows. 1. Photogrammetric determination of particle coordinates. Exp Fluids 15:133–146, URL http://dx.doi.org/10.1007/BF00190953

Marusic I, McKeon BJ, Monkewitz PA, Nagib HM, Smits AJ, Sreenivasan KR (2010) Wall-bounded turbulent flows at high Reynolds numbers: Recent advances and key issues. Phys Fluids 22:065–103, URL http://dx.doi.org/10.1063/1.3453711

Mason P (2006) Large-eddy simulation: A critical review of the technique. Q J Roy Meteor Soc 120:1–26, URL http://dx.doi.org/10.1002/qj.49712051503

McGuinness M (1978) Flow with a separation bubble: Steady and unsteady aspects. PhD thesis, University of Cambridge

Meinhart CD, Wereley ST, Santiago JG (2000) A PIV algorithm for estimating time-averaged velocity fields. J Fluids Eng 122:285–289, URL http://dx.doi.org/10.1115/1.483256

Meiss JH, Schröder W (2008) Large-Eddy Simulation of the Base Flow of a Cylindrical Space Vehicle Configuration. In: 6th European Symposium on Aerothermodynamics for Space Vehicles, Versailles, France

Melling A (1997) Tracer particles and seeding for particle image velocimetry. Meas Sci Tech 8:1406–1416, URL http://dx.doi.org/10.1088/0957-0233/8/12/005

Menter F, Kuntz M, Langtry R (2003) Ten years of industrial experience with the SST turbulence model. Begell House, Inc, vol 4, pp 625–632

Meyers J (1991) Generation of particles and seeding. VKI Laser Velocimetry 1

Mie G (1908) Beiträge zur Optik trüber Medien, speziell kolloidaler Metallösungen. Ann Phys 25:377–445

Moin P, Mahesh K (1998) Direct numerical simulation: a tool in turbulence research. Annu Rev Fluid Mech 30:539–578, URL http://dx.doi.org/10.1146/annurev.fluid.30.1.539

Nagib HM, Chauhan KA, Monkewitz PA (2007) Approach to an asymptotic state for zero pressure gradient turbulent boundary layers. Philos T R Soc A 365:755–770, URL http://dx.doi.org/10.1098/rsta.2006.1948

Nakagawa S, Hanratty TJ (2001) Particle image velocimetry measurements of flow over a wavy wall. Phys Fluids 13:3504, URL http://dx.doi.org/10.1063/1.1399291

Nickels TB (2004) Inner scaling for wall-bounded flows subject to large pressure gradients. J Fluid Mech 521:217–239, URL http://dx.doi.org/10.1017/S0022112004001788

Nogueira J, Lecuona A, Rodriguez PA (2001) Identification of a new source of peak locking, analysis and its removal in conventional and super-resolution PIV techniques. Exp Fluids 30:309–316, URL http://dx.doi.org/10.1007/s003480000179

Nogueira J, Lecuona A, Rodriguez PA (2005) Limits on the resolution of correlation PIV iterative methods. Fundamentals. Exp Fluids 39:305–313, URL http://dx.doi.org/10.1007/s00348-005-1016-2

Ohmi K, Li HY (2000) Particle tracking velocimetry with new algorithms. Meas Sci Tech 11:603–616, URL http://dx.doi.org/10.1088/0957-0233/11/6/303

Olsen MG (2010) Depth of correlation reduction due to out-of-plane shear in microscopic particle image velocimetry. Meas Sci Tech 21:9, URL http://dx.doi.org/10.1088/0957-0233/21/10/105406

van Oudheusden BW, Scarano F (2008) Topics in Applied Physics, Springer Verlag, chap PIV Investigation of Supersonic Base-Flow-Plume Interaction, pp 465–474

Overmars E, Warncke N, Poelma C, Westerweel J (2010) Bias errors in PIV: the pixel locking effect revisited. In: 15th Int Symp on Applications of Laser Techniques to Fluid Mechanics Lisbon, Portugal, 05-08 July

Pfeffer H (1996) Towards Reusable Launchers - A Widening Perspective. ESA Bulletin 87:58–65

Pitot H (1732) Description d'une machine pour mesurer la vitesse des eaux courantes et le sillage des vaisseaux. Histoire de l'Académie royale des sciences avec les mémoires de mathématique et de physique tirés des registres de cette Académie pp 363–376

Pitsch H (2006) Large-eddy simulation of turbulent combustion. Annu Rev Fluid Mech 38:453–482, URL http://dx.doi.org/10.1146/annurev.fluid.38.050304.092133

Prasad A, Adrian R (1993) Stereoscopic particle image velocimetry applied to liquid flows. Exp Fluids 15:49–60, URL http://dx.doi.org/10.1007/BF00195595

Raffel M, Willert CE, Wereley ST, Kompenhans J (2007) Particle image velocimetry: a practical guide. Springer Verlag

Roidl B (2012) A zonal RANS-LES method for compressible flows. Comput Fluids 67:1–15, URL http://dx.doi.org/10.1016/j.compfluid.2012.07.003

Roshko A, Thomke GJ (1966) Observations of Turbulent Reattachment behind an Axisymmetric Downstream-Facing Step in Supersonic Flow. AIAA Journal 4:975–980

Rossi M, Segura R, Cierpka C, Kähler CJ (2010) On the effect of particle image intensity and image preprocessing on depth of correlation in micro-PIV measurements. In: 15th International Symposium on Applications of Laser Techniques to Fluid Mechanics, Lisbon, Portugal, July 5-8

Sagaut P (2005) Large eddy simulation for incompressible flows: an introduction. Springer Verlag

Santiago JG, Wereley ST, Meinhart CD, Beebe DJ, Adrian RJ (1998) A particle image velocimetry system for microfluidics. Exp Fluids 25:316–319, URL http://dx.doi.org/10.1007/s003480050235

Scarano F (2001) Iterative image deformation methods in PIV. Meas Sci Tech 13:R1–R19, URL http://dx.doi.org/10.1088/0957-0233/13/1/201

Scarano F, Sciacchitano A (2011) Robust elimination of light reflections in PIV. In: 9th international symposium on particle image velocimetry - PIV'11, Kobe, Japan, July 21-23

Scarano F, Benocci C, Riethmuller ML (1999) Pattern recognition analysis of the turbulent flow past a backward facing step. Phys Fluids 11:3808, URL http://dx.doi.org/10.1063/1.870240

Scharnowski S, Kähler CJ (2013) On the effect of curved streamlines on the accuracy of PIV vector fields. Exp Fluids 54:1435, URL http://dx.doi.org/10.1007/s00348-012-1435-9

Scharnowski S, Hain R, Kähler CJ (2012) Reynolds stress estimation up to single-pixel resolution using PIV-measurements. Exp Fluids 52:985–1002, URL http://dx.doi.org/10.1007/s00348-011-1184-1

Schlichting H, Gersten K (2006) Grenzschicht-Theorie. Springer Verlag

Scholz U, Kähler CJ (2006) Dynamics of flow structures on heaving and pitching airfoils. In: 13th International Symposium on Applications of Laser Techniques to Fluid Mechanics, Lisbon, Portugal

Schram C, Rambaud P, Riethmuller ML (2004) Wavelet based eddy structure eduction from a backward facing step flow investigated using particle image velocimetry. Exp Fluids 36:233–245, URL http://dx.doi.org/10.1007/s00348-003-0695-9

Schrijer F, Sciacchitano A, Scarano F, Hanneman K, Pallegoix J, Maseland J, Schwane R (2011) Experimental Investigation of Base Flow Buffeting on the Ariane 5 Launcher Using High Speed PIV. In: Proceedings 7th European Symposium on Aerothermodynamics for Space Vehicles , Brugge, Belgium, 9-12 May

Smagorinsky J (1963) General Circulation Experiments with the Primitive Equations: I The Basic Experiment. Mon Weather Rev 91:99–164, URL http://dx.doi.org/10.1175/1520-0493(1963)091<0099:GCEWTP>2.3.CO;2

Smits A, Monty J, Hultmark M, Bailey S, Hutchins N, Marusic I (2011) Spatial resolution correction for wall-bounded turbulence measurements. J Fluid Mech 676:41–53, URL http://dx.doi.org/10.1017/jfm.2011.19

Spalart P, Allmaras S (1992) A one-equation turbulence model for aerodynamic flows. In: AIAA, Aerospace Sciences Meeting and Exhibit, 30 th, Reno, NV

Stanislas M, Okamoto K, Kähler CJ (2003) Main results of the first international PIV challenge. Meas Sci Tech 14:R63–R89, URL http://dx.doi.org/10.1088/0957-0233/14/10/201

Stanislas M, Okamoto K, Kähler CJ, Westerweel J (2005) Main results of the second international PIV challenge. Exp Fluids 39:170–191, URL http://dx.doi.org/10.1007/s00348-005-0951-2

Stanislas M, Okamoto K, Kähler CJ, Westerweel J, Scarano F (2008) Main results of the third international PIV Challenge. Exp Fluids 45:27–71, URL http://dx.doi.org/10.1007/s00348-008-0462-z

Statnikov V, Glatzer C, Meinke M, Scrhöder W (2012) Numerical investigation of the Near Wake of Generic Space Launcher Systems. In: EUCASS Flight Physics Book (Vol. 5)

Stitou A, Riethmuller ML (2001) Extension of PIV to super resolution using PTV. Meas Sci Tech 12:1398–1403, URL http://dx.doi.org/10.1088/0957-0233/21/4/045401

Tian Q, Lowe K, Simpson R (2007) A three-velocity-component laser-doppler velocimeter for measurements inside the linear compressor cascade. Exp Fluids 43:487–499, URL http://dx.doi.org/10.1007/s00348-007-0311-5

Vollmers H (2001) Detection of vortices and quantitative evaluation of their main parameters from experimental velocity data. Meas Sci Tech 12:1199–1207, URL http://dx.doi.org/10.1088/0957-0233/12/8/329

Wattendorf FL, Kuethe AM (1934) Investigations of Turbulent Flow by Means of the Hot-Wire Anemometer. J Appl Phys 5:153–164, URL http://dx.doi.org/10.1063/1.1745244

Weiss P, Deck S, Robinet JC, Sagaut P (2009) On the dynamics of axisymmetric turbulent separating/reattaching flows. Phys Fluids 21:075,103, URL http://dx.doi.org/10.1063/1.3177352

Wereley ST, Meinhart CD (2001) Second-order accurate particle image velocimetry. Exp Fluids 31:258–268, URL http://dx.doi.org/10.1007/s003480100281

Wernet JH, Wernet MP (1994) Stabilized Alumina/Ethanol Colloidal Dispersion for Seeding High Temperature Air Flows. In: Proceedings of the ASME Symposium on Laser Anemometry: Advances and Applications, Lake Tahoe, NV, June 19-23

Westerweel J (2008) On velocity gradients in PIV interrogation. Exp Fluids 44:831–842, URL http://dx.doi.org/10.1007/s00348-007-0439-3

Westerweel J, Nieuwstadt F (1991) Performance tests on 3-dimensional velocity measurements with a two-camera digital particle-image velocimeter. In: Laser Anemometry-Advances and Applications 1991, vol 1, pp 349–355

Westerweel J, Scarano F (2005) Universal outlier detection for piv data. Exp Fluids 39:1096–1100, URL http://dx.doi.org/10.1007/s00348-005-0016-6

Westerweel J, Geelhoed PF, Lindken R (2004) Single-pixel resolution ensemble correlation for micro-PIV applications. Exp Fluids 37:375–384, URL http://dx.doi.org/10.1007/s00348-004-0826-y

Willert C (1997) Stereoscopic particle image velocimetry for application in wind tunnel flows. Meas Sci Tech 8:1465–1479, URL http://dx.doi.org/10.1088/0957-0233/8/12/010

Willert C, Stasicki B, Klinner J, Moessner S (2010) Pulsed operation of high-power light emitting diodes for imaging flow velocimetry. Meas Sci Tech 21:075,402, URL http://dx.doi.org/10.1088/0957-0233/21/7/075402

Willert CE, Gharib M (1991) Digital Particle Image Velocimetry. Exp Fluids 10:181–193, URL http://dx.doi.org/10.1007/BF00190388

Wu X, Moin P (2009) Direct numerical simulation of turbulence in a nominally zero-pressure-gradient flat-plate boundary layer. J Fluid Mech 630:5–41, URL http://dx.doi.org/10.1017/S0022112009006624

Wygnanski I, Fiedler H (1969) Some measurements in the self-preserving jet. J Fluid Mech 38:577–612, URL http://dx.doi.org/10.1017/S0022112069000358

Wyngaard JC (1968) Measurement of small-scale turbulence structure with hot-wires. J Phys E 1:1105–1108, URL http://dx.doi.org/10.1088/0022-3735/1/11/310